THE DEVELOPMENT AND FABRICATION OF MINIATURIZED DIRECT METHANOL FUEL CELLS AND THIN-FILM LITHIUM ION BATTERY HYBRID SYSTEM FOR PORTABLE APPLICATIONS

A Dissertation
Presented to
The Academic Faculty

by

Shruti Prakash

In Partial Fulfillment
of the Requirements for the Degree
Doctor of Philosophy in the
School of Chemical & Biomolecular Engineering

Georgia Institute of Technology
May 2009

THE DEVELOPMENT AND FABRICATION OF MINIATURIZED DIRECT METHANOL FUEL CELLS AND THIN-FILM LITHIUM ION BATTERY HYBRID SYSTEM FOR PORTABLE APPLICATIONS

Approved by:

Dr. Paul A. Kohl, Advisor
School of Chemical & Biomolecular Engineering
Georgia Institute of Technology

Dr. Meilin Liu
School of Material Science & Engineering
Georgia Institute of Technology

Dr. Carson Meredith
School of Chemical & Biomolecular Engineering
Georgia Institute of Technology

Dr. Gary Gray
Georgia Tech Research Institute
Georgia Institute of Technology

Dr. Tom Fuller
School of Chemical & Biomolecular Engineering
Georgia Institute of Technology

Dr. Gabriel Rincón-Mora
School of Electrical & Computer Engineering
Georgia Institute of Technology

Date Approved: March 4, 2009

In dedication to my Ma and Papa, my didi Shraddha and my husband Amit who believed in me and made my life meaningful

ACKNOWLEDGEMENTS

I would like to acknowledge a number of people who helped me achieve my academic goals. First, I wish to thank my thesis advisor, Dr. Paul Kohl, who taught me the essence of critical thinking, scientific research and its impact on solving practical problems. Without his help, encouragement and guidance, this dissertation would not be possible.

I wish to thank the entire Kohl-research group for making the past 4-5 years a memorable and fun learning experience. In particular, I would like to acknowledge Daphne Perry for all her help and support. I would like to extend my appreciation to Dr. William Mustain, who participated in this project for two years as a post-doctoral researcher. I would like to acknowledge his help in the study of battery characteristics. I would like to thank Hyea Kim for sharing the ups and downs of the project with me.

In addition, I would like to thank and extend my deep gratitude to my parents, Madhu and Sudhanshu Prakash and my sister Shraddha Prakash, who always believed in me despite my failures, loved me unconditionally and encouraged me to dream, explore and learn. Without them, I would not be where I am today. I would also like to thank my uncle Dr. Amit Prakash and my aunt Mrs. Kalyanee Sinha who helped me pursue my education in the USA. Finally, I would like to thank my husband, Amit, for his constant support, meaningful advice and unconditional love. He has always been my best friend and it is because of him that I continue to grow as a person.

TABLE OF CONTENTS

LIST OF TABLES

LIST OF FIGURES

LIST OF SYMBOLS

A	Pre-exponential Rate Constant
A	Area
α	Ratio of Permeability Coefficient Of Two Species
χ	Electrolyte Aspect Ratio
C	Battery Capacity
δ_1	Thickness of Membrane
δ_2	Thickness of Catalyst Layer
D_i	Diffusion Coefficient Of Species *i*
ε	Energy Efficiency Of A Fuel Cell
ε	Voltage Efficiency
E_V	Electrochemically Useful Energy
E_R	Resistive Energy
E_x	Energy Lost Through Permeation
E_P	Activation Energy of Permeation
E_D	Activation Energy of Diffusion
E_P	Activation Energy of Permeation
E_D	Activation Energy of Diffusion
F	Faraday's Constant
$\gamma_{theoretical}$	Theoretical Efficiency Of CO_2 Vent
$\gamma_{Experimental}$	Experimental Efficiency Of CO_2 Vent
ΔH_S	Enthalpy Change of Sorption
i	Current
i_{SD}	Self-discharge Current

i_C	Charging Current
l	Thickness of CO_2 Vent Membrane
λ	Aspect Ratio of CO_2 Vent Membrane
μ	Micro
n	Number of Electrons
N_i	Rate Of Transport Of Species *i*
$\wp_{CO_2}$	Partial Pressure Of CO_2
$\wp_{MeOH}$	Partial Pressure Of MeOH
P_i	Permeability Coefficient Of Species *i*
Δp	Pressure Drop
ρ	Resistivity
r_{SiOH}	Rate Of Silanol Formation
r_{SiO2}	Rate of Silicon Dioxide Formation
R	Gas Constant
S	Rate Selectivity
S_i	Solubility Coefficient Of Species *i*
t	Time
t_c	Charging Time
t_D	Discharging Time
V_d	Discharging Voltage
V_C	Charging Voltage
V_{OP}	Operating Voltage
V_{OCV}	Open Circuit Potential
Ω	Ohms

LIST OF ABBREVIATIONS

CH_3OH	Methanol
CO_2	Carbon Dioxide
DMFC	Direct Methanol Fuel Cell
e^-	Electron
FTIR	Fourier Transfer Infra-Red Spectroscopy
H^+	Proton
He	Helium
H_2O	Water
H_2	Hydrogen
kPa	Kilo Pascal
Li-ion	Lithium-Ion
Li_xCoO_2	Lithium Cobalt Oxide
$Li_xMn_2O_4$	Lithium Manganese Oxide
Li_xNiO_2	Lithium Nickel Oxide
$Li_xV_2O_5$	Lithium Vanadium Oxide
MEA	Membrane Electrode Assembly
MeOH	Methanol
N_2O	Nitrous Oxide
OH	Hydroxide
PEM	Proton Exchange Membrane
PECVD	Plasma Enhanced Chemical Vapor Deposition
PDMS	Poly Dimethyl Siloxane

PSG	Phospho-Silicate Glass
PTMSP	Poly Trimethyl Silyl Propyne
PH_3	Phosphine
Pt-Ru/C	Platinum-Ruthenium on Carbon
Pt/C	Platinum on Carbon
QMS	Quadruple Mass Spectroscopy
RF	Radio Frequency
RGA	Residual Gas Analyser
SCCM	Standard Cubic Centimeter
SiH_4	Silane
STP	Standard Temperature Pressure
TGA	Thermo Gravimetric Analysis
VCA	Video Contact Angle
VOC	Volatile Organic Compound
V_2O_5	Vanadium Oxide
WHr	Watt Hour
XPS	X-ray Photoelectron Spectroscopy

SUMMARY

In this work, a hybrid power module comprising of a direct methanol fuel cell (DMFC) and a Li-ion battery has been proposed for low power applications. The challenges associated with low power and small DMFCs were investigated and the performance of commercial Li-ion batteries was evaluated. At low current demand (or low power), methanol leakage through the proton exchange membrane (PEM) reduces the efficiency of a DMFC. Consequently, a proton conducting methanol barrier layer is needed. Since volume restrictions make it infeasible to use balance of plant components (active fuel channels) in DMFCs, passive fuel delivery systems are the only available option. When using a passive fuel delivery system, a CO_2 vent is required to release the pressure built in the fuel tank of these DMFCs. In this work, the above challenges in advancing the performance of a low power DMFC have been addressed. Finally, Li-ion batteries have been evaluated for low self-discharge and high voltage efficiency.

Phospho- silica glass (PSG) was formed as a methanol resistant PEM. It was demonstrated that phosphorus doping in the silica matrix increased the ionic conductivity of the glass membrane. The doping increased the number of non-bridging type bonds (P-OH) in the silica matrix, which in turn increased the acidic-OH groups that allow proton conduction. It was also observed that the plasma deposition condition of the glass membrane could be altered to achieve a desired ionic conductivity in the membrane. At low temperature and high RF power, the PSG films demonstrated high ionic conductivity and structural integrity. When compared to PEMs with pure Nafion membranes, the

PEMs fabricated with Nafion-PSG hybrid membranes not only showed a reduction in the methanol permeability but also an improvement in the DMFC performance.

A CO_2 vent was fabricated from poly (dimethyl siloxane) (PDMS) and poly (1-trimethyl silyl propyne) (PTMSP) base polymers. It was observed that the vent membrane had higher permeability coefficient for CO_2 than methanol. Addition of hydrophobic additives like 1, 6-divinylperfluorohexane to the base polymer further enhanced the selectivity of the vent for CO_2 transport. When operated at high temperatures, the rate of CO_2 flux increased, which in turn increased its permeability coefficient. However, the sorption of methanol molecules limited their transport through the polymer backbone and, as a result, their permeability coefficient decreased with temperature. The experimental results validated the theoretical model developed for estimating the vent efficiency. It was observed that at high selectivity (α of 9.2), the vent was 95% efficient.

The use of Li-ion battery in a power module as a secondary energy storage device results in a non-traditional duty cycle. This unique duty cycle requires the battery to be active for a very short span of time compared to its dormant or sleep stage. Under such a load, the effects of self-discharge and voltage loss were evaluated for Panasonic coin cells and thin film LiPON cells. It was observed that the thin film battery outperformed the others in terms of low energy loss. Nonetheless, the performance of small Panasonic coin cells with vanadium oxide cathode was comparable at low discharge rates of less than 0.01% depth of discharge. Lastly, it was also observed that the batteries have stable cycles at low discharge rates.

CHAPTER 1

INTRODUCTION

1.1 Motivation

Increasing the efficiency of portable electronics is a continuing effort, owing to the increasing market demand for smaller but longer-lasting devices. These electronic devices typically require an average power in the range of microwatts to watts, depending on function and duty cycle. The power source of such devices must have a small form factor, light weight and high energy density.

One growing market for these devices is electronic sensors. These devices communicate wirelessly and are deployed in locations where plug-in power is not readily available, and a portable power source is essential to their implementation. A second area is the use of wireless sensors in commercial buildings. The sensing and control of heating, ventilation, and air-conditioning systems will improve the energy efficiency and make building more environmentally friendly. A third technological area is automated meter readers that can allow wireless sensors to form self-assembled networks. A fourth area of interest is home automation. Again, energy efficiency can be improved by monitoring and selectively controlling heating, air-conditioning, and lighting. Finally, wireless sensors, especially those forming networks, are useful in environmental and homeland security situations.

In each of these applications, the cost, lifetime, size and weight of the power source are critical to the value of the overall system. Many of these sensors have simple

function and low duty cycles, i.e., they acquire data only occasionally, and as such, they require low-power to operate. Such devices may require 10's of mW for milliseconds to acquire or transmit data, and 10's μW for long periods in sleep-mode. This style of operation – low, intermittent power over a long time period is far different from how traditional power sources such as in transportation, high-power electronic devices, or electric power operate.

While batteries can be considered as an economical means of powering these wireless electronic devices, they suffer from a few drawbacks. The complex recharging, replacement and disposal of batteries limit the portability and uninterrupted operation of the wireless devices. Fuel cells, in particular direct methanol fuel cells (DMFCs), with their high energy density can be explored as a power source for electronic devices. However, like the current batteries, the state-of-the-art fuel cells also suffer from a few drawbacks. Most importantly, the slow kinetics of electrochemical reactions makes these fuel cells incapable of responding to transient load demand with acceptable efficiency.

A hybrid power module, comprising a DMFC integrated in parallel with a battery, can address the shortcomings of the two individual components [1]. The resulting hybrid power system will utilize the energy from a highly efficient renewable energy source (fuel cell) to recharge the secondary storage device (battery) such that the module together can run an electronic device without interruption[1, 2]. Figure 1.1 shows the architecture of a hybrid power module. In such a module, the role of the fuel cell is to provide sleep current and recharge the battery as and when needed, while the Li-ion battery provides the burst current when demanded by the load. The remaining component of the module is a charger-mixer circuit which converts the energy derived from fuel cells to useful voltage.

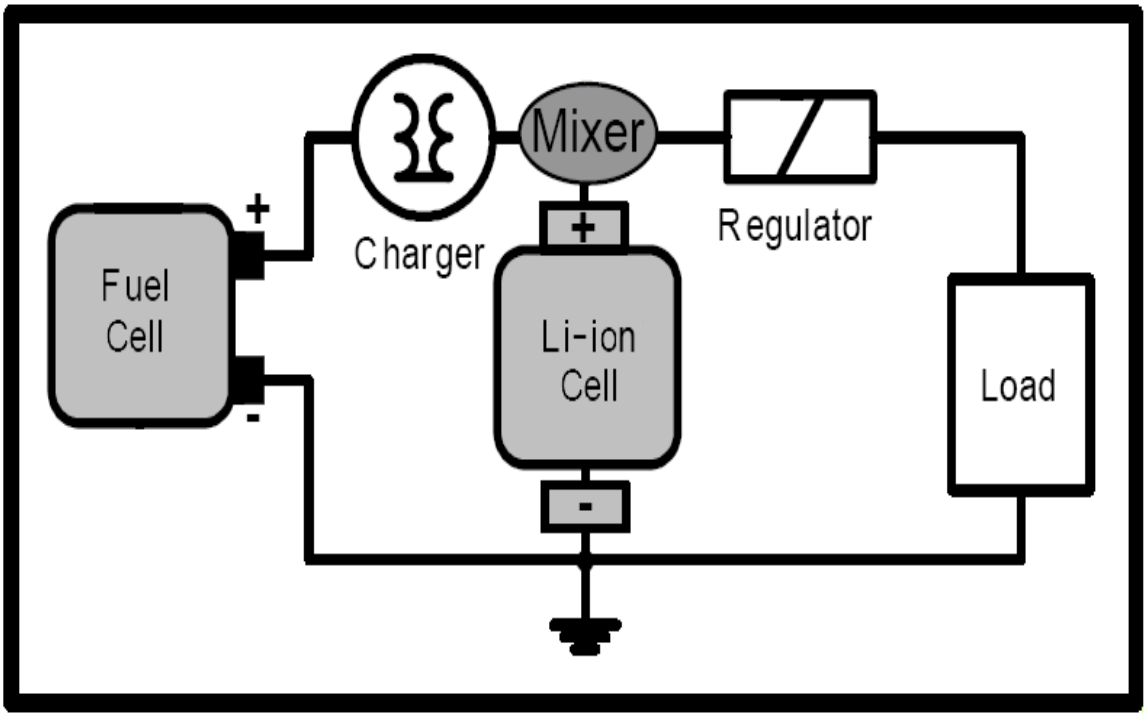

Figure 1.1: Hybrid fuel cell Li-Ion power supply

1.2 Dissertation Overview

Based on the motivations discussed above, the key objectives of this dissertation can be outlined. Each of these objectives will ultimately assist in the design of an efficient power module shown in Figure 1.1. Since the architecture shown in Figure 1.1 introduces volume and size restriction on fuel cells, it is of interest to understand and define the challenges associated with the design of a small Direct Methanol Fuel Cells (DMFC). The first objective of this study is to develop a proton exchange membrane system (PEM) that can address the issues of methanol crossover without compromising on its ionic conductivity. The second objective is to address the CO_2 accumulation in a closed fuel tank of DMFCs and develop an efficient CO_2 release system. Understanding the mechanism of transport is a key parameter in the design of a competent CO_2 release

system. Finally, since the hybrid power module is designed for low power applications, it is essential to identify an efficient secondary energy storage device that suffers from minimal energy loss over time. Thus, the third and final objective of this dissertation is to evaluate the loss and performance of commercial Li-Ion batteries.

CHAPTER 2

BACKGROUND

2.1 Direct Methanol Fuel Cells

Fuel cells are galvanic cells that convert chemical energy to electrical energy[3]. The electrochemical reaction at the anode of a fuel cell oxidizes the fuel source to produce protons (H^+) and electrons (e^-). The protons transfers through the proton exchange membrane (PEM) and in the presence of electrons, they catalytically reduce oxygen to form water. The electrons moving in the external circuit can be harnessed to generate electricity. For low temperature operation (room temperature), PEM fuel cells often utilize hydrogen, methanol or formic acid as the source of protons [4-8]. Of these, methanol is the most feasible choice for portable applications due to its non-corrosive nature and easy storage. At the anode of a Direct Methanol Fuel Cell (DMFC), methanol is catalytically reduced in the presence of Pt-Ru to generate protons. Equation 2.1 shows the oxidation of methanol.

$$CH_3OH + H_2O \rightarrow CO_2 + 6H^+ + 6e^- \qquad (2.1)$$

At the cathode, oxygen from air is catalytically reduced in the presence of Pt to form water, as shown in Equation 1.2 [8]

$$O_2 + 4H^+ + 4e^- \rightarrow 2H_2O \qquad (2.2)$$

Based on the above reactions a 17 M methanol anode feed is theoretically possible. However, in conventional systems, the highest currents and powers are achieved with

dilute methanol solutions in 0.5 M to 12 M methanol range [9]. The concentration optimization is thus, a balance of three effects. First, if the methanol concentration is too high, permeation of fuel through the electrolyte is prohibitive. Second, if the methanol concentration is too low, the reaction kinetics is sluggish and mass transport of the methanol reactant to the anode limits the current density. Finally, up to 15 water molecules can be transported by electroosmotic drag from the anode to the cathode for each methanol molecule oxidized [10]. This dilution of the fuel is highly undesirable because it decreases the energy density of the cell and can cause water management problems. As a result, careful optimization of the above listed effects will impart higher energy efficiency to DMFCs.

Fuel cells have very high theoretical energy densities because concentrated liquid fuels with high equivalence (e.g. six electrons from methanol) can be used, and the oxidizing agent (species to be reduced at the cathode) is readily available (oxygen from air)[3, 11, 12]. The theoretical energy density of pure methanol is 6100 Whr/kg, however, thermodynamic efficiency limits the discharge of methanol fuel at the theoretical thermodynamic voltage. Moreover, since methanol oxidation can takes place only in the presence of water, dilute (12 M) methanol discharged at 0.5 V represents a more realistic DMFC operating point. Under these conditions, the energy density of DMFC would be over 1200 Whr/kg.

As a result, DMFCs have received significant attention as a likely power source for fully integrated low power applications (1-1000 μW) installed directly on a single, stand-alone chip[6]. In a hybrid power module application, the role of a DMFC is to provide the constant power for the sleep-mode and to recharge the battery. Therefore, the

design parameter for a DMFC shifts from the traditional high power mode, to low power high efficiency mode. The operating efficiency of a DMFC can be considered to be a function of useful methanol consumption (methanol consumed through electrochemical reaction) and high ionic conductivity of the PEM. Thus, it is essential that the two primary energy loss mechanisms be mitigated to achieve high efficiency and long operating time. First, the permeation of methanol through the electrolyte membranes should be reduced and second, the internal resistance of the PEM should be mitigated.

An expression for the energy conversion efficiency of a fuel cell can be derived by considering the energy available relative to the energy delivered. The useful energy delivered from a fuel cell, E_U, is given in Equation 2.3.

$$E_U = iV_{op} \tag{2.3}$$

Where i is the fuel cell current and V_{op} is the operating voltage. Resistive losses caused by ionic transport through the proton exchange membrane, E_R, is expressed by Equation 2.4.

$$E_R = \left(\frac{i^2 \rho \delta_1}{A_1} \right) \tag{2.4}$$

Where ρ is the ionic resistivity of the electrolyte, δ_1 is ionic path length, and A_1 is the electrochemically active area.

Fuel can be lost by permeation through the electrolyte and is often referred to as methanol crossover. This loss, E_x, is given by Equation 2.5.

$$E_X = \left(\frac{P_1 \Delta p A_2}{\delta_2} \right) nFV_{ocv} \tag{2.5}$$

Where P_1 is the permeation coefficient of the membrane, Δp is the pressure drop across the membrane, A_2 is the exposed membrane area available for fuel transport through the membrane, δ_2 is the electrolyte thickness, n is the number of electrons transferred in the reaction, and F is Faraday's constant. It should be noted that generally δ_1 is the same as δ_2, however A_1 and A_2 need not be the same. Appropriately engineering the electrode structure may block the membrane from crossover loss while maintaining a large membrane area for low resistive losses (i.e. $A_2<A_1$). Combining Equations 2.3-2.5, the energy efficiency, ε, is given by Equation 2.6.

$$\varepsilon = \frac{iV_{op}}{\left(\frac{i^2 \rho \delta}{A_1}\right) + \left(\frac{P_1 \Delta p A_2}{\delta}\right) nFV_{ocv} + iV_{op}} \tag{2.6}$$

Fuel loss from permeation through the PEM membrane is especially important in ultra low-power fuel cells compared to intermediate and high power cells because of three main reasons. First, the rate of fuel consumption through electrochemical oxidation is orders of magnitude lower; second, the ohmic loss is negligible for low current ranges since it a function of the square of the operating current; and third, the electrolyte aspect ratio (χ=A/δ) is high. That is, the current in the numerator of Eq. 2.6 is smaller (can be much smaller) than in high-power systems, making it more important to have tight control of losses (terms in the denominator of Eq. 2.6), especially the permeation losses.

In order to truly realize a fully functional, long life, low power direct methanol fuel cell, there are several components that need to be considered. Since most of the solutions in the literature focus on high power, short life systems, challenges associated with low power, long life DMFCs have not been explored. In this study, the challenges pertaining to the design and performance of a low power, long life DMFC have been

identified and addressed. The first of these is the proton exchange membrane (PEM). Nafion® is a logical choice for initial studies, as it the most commonly used solid electrolyte. Nonetheless, its permeability to methanol limits it use for long-life devices. Second, in order to contain the methanol fuel, which is highly volatile, the fuel container must be near-hermetically sealed. However, at the anode surface, carbon dioxide gas is produced as the reaction byproduct. If this is not released to the environment, the pressure in the fuel container will increase significantly and quickly, leading to rupture and, perhaps, explosion. Therefore, a CO_2 selective vent needs to be invented and implemented. Also, due to the small size constraints considered here, it is essential to eliminate any balance-of-plant components such as heaters, piping, pumps, etc. This leads to room-temperature device operation, atmospheric oxygen harvesting at the cathode as well as the need for a passive fuel delivery system at the anode.

With all of this taken into account, the proposed DMFC battery hybrid module is shown in Figure 2.1. In this module, the microporous substrate impregnated with the polymer electrolyte is used as the structural base of the device with a thin-walled metal can to hold the methanol. The novel carbon dioxide vent is incorporated into the metal fuel container; the container also contacts the fuel cell anode (inner side of the membrane) and provides the negative contact for the device to the board. The fuel cell, electronics and the lithium-ion battery are then mounted on a patterned board in order to make electrical contact.

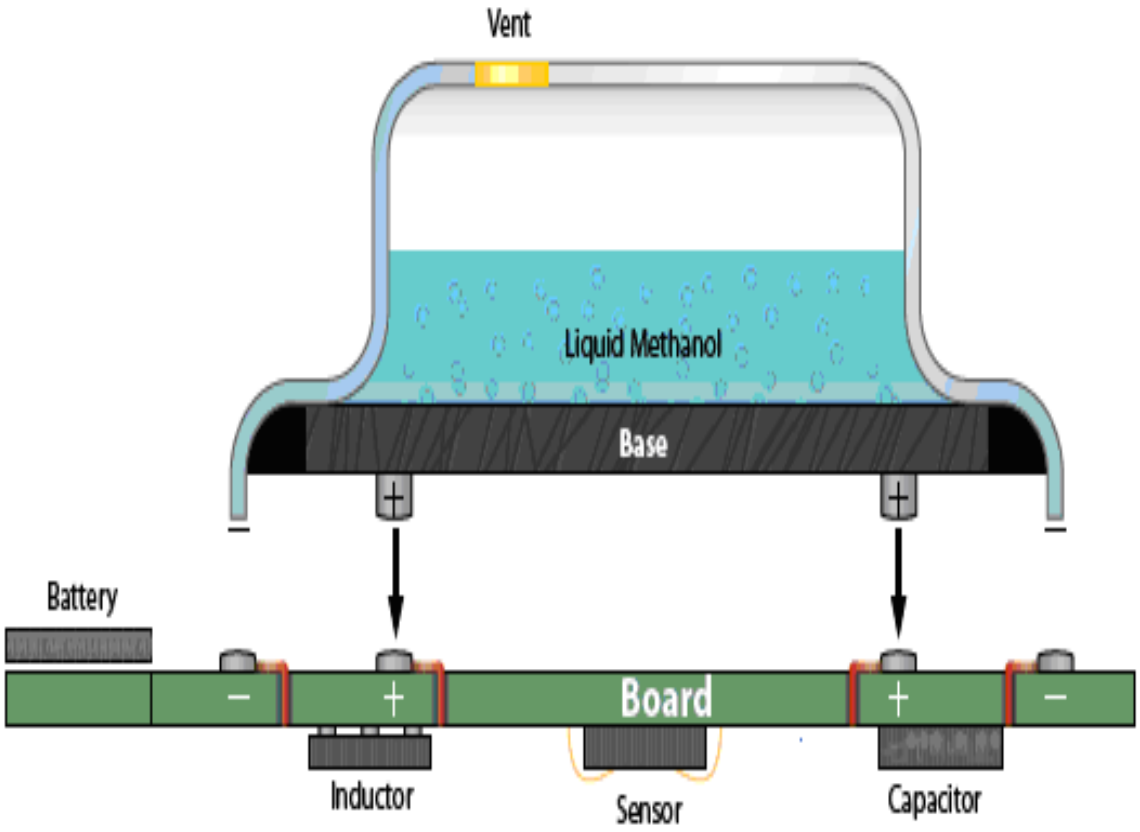

Figure 2.1: DMFC and Li-ion battery hybrid power module

2.2 Proton Exchange Membrane (PEM) for DMFCs

Silicate glasses deposited by plasma enhanced chemical vapor deposition (PECVD) have traditionally been used as low-loss electrical insulators in microelectronic devices. However, in recent years it has been reported that introducing minority additives into the silicate matrix allows researchers to tune the physical properties of these glasses, making them attractive for a variety of applications. It has been shown that introducing limited amounts of a secondary oxide in the glass can tailor its structure, mechanical strength, and both the electrical and ionic conductivity[13]. One possible application of silicate glasses with increased ionic conductivity is fully inorganic electrolyte materials for low temperature proton exchange membrane fuel cells. Silicate glasses with adequate proton conductivity are ideal because they are inexpensive, reliable, easily fabricated over a wide range of thicknesses and can serve as a methanol barrier layer to lower the fuel crossover rate in direct methanol fuel cells (DMFCs).

Silicate glasses have a tetrahedral structure where defect sites, –OH terminated silicon groups, assist in ion transport by providing nano-porous regions that are tens of angstroms in diameter. These imperfections retain the high electrical loss characteristics of the structure, while providing a surface-site ionic pathway along the length of the pores. The ionic conductivity is achieved by liberation of protons from silanol hydroxyl groups in glass structure pores[14]. Abe et al. have shown that oxides prepared at low temperature incorporate a large number of hydroxide and water impurities that impart high porosity to the glass as compared to those formed at high temperature[15].

It has also been shown that doping of silicate glasses with Group V elements, such as phosphorus, increases the conductivity of the silicate glasses. This is accomplished by introducing gaps in the tetrahedral glass network as the requisite Si-O-Si bond formation is sterically hindered and replaced by either —Si-OH or —Si-O-POH surface groups. This increases both the free volume and pore wall surface area, thus increasing the ion-exchange capacity of the prepared glass. It should also be considered that the Group V hydroxyl groups have a higher acidity when compared to silanol. This indicates that the associated proton in the P-OH group is more strongly bonded with neighboring water molecules[13], which should increase its mobility.

Further studies in this area have shown that proton mobility is also a function of the hydrogen bonding that occurs between the hydroxyl groups attached to a network-forming cation (X = Si^{4+} or P^{5+}) and a hydroxide ion (X-O-H$^{\cdots}$O-X)[16, 17]. It has been shown that the strength of the hydrogen bond between the hydroxyl groups depends on the type of counter ion it is bonded to. The hydrogen bonding is extremely weak in cases where the counter ion is of the bridging type (X-O-X) compared to those where the counter ion is of the non-bridging type (X-O^-). Uma et al. found that in phosphorus-doped silicate glasses (PSG), the phosphorus is bonded to one bridging and three non-bridging oxygen atoms[18]. It is believed that the increase in non-bridging oxygen bonds increases the ion conduction sites, leading to higher conductivity for phosphorus-doped silicate glasses.

Additional enhancement in the ionic conductivity of silicate glasses occurs by water absorption into the pores. The defect sites located within the glass film provide a high local charge density and electrostatic field, promoting the chemisorption of water

molecules that provide a bulk transport mechanism for the charge carrying protons. Therefore, the magnitude of the ionic conductivity in phosphorus doped silica glasses depends on free volume and pore surface area (for ion transport), chemical structures in the glass (e.g. -Si-OH and –P-OH concentration), intermediate range order and the local bonding environment in the glass network[15, 19, 20].

It has been well established that high quality phosphorous-doped silicate glasses can be fabricated by melt-quenching techniques. However, the high processing temperature of melt casting makes it incompatible with many microelectronic and electrochemical applications. Also, glasses fabricated by this technique have low proton conductivity, making it undesirable as an electrolyte material [21, 22]**.** Therefore, alternative fabrication methods have been explored in order to deposit the proton-conducting silicate glasses, including sol-gel and plasma enhanced chemical vapor deposition (PECVD). Sol-gel processes have been commonly used, though they often suffer from low mechanical strength and stability [22-24].

On the other hand, the low temperature, PECVD glasses yield high mechanical strength and stability glasses as well as a fabrication technique that is compatible with state-of-the-art microelectronic materials and processes. Plasma deposited oxides can also have higher porosity than high-temperature sol-gel glasses due to increased silanol concentration and water impurities, especially when deposited at low temperature [25], which should provide enhanced ionic conductivity. Furthermore, the PECVD technique provides better control of the surface reactions, adsorbate mobility, and desorption of reaction byproducts by controlling the number of active radicals and ions in the plasma,

which may be adjusted by control of several variables, including substrate temperature, chamber pressure, RF power and reactant flow-rate[14].

2.3 CO_2 vents for DMFCs

The process of CO_2 discharge from the anode chamber without significant loss of methanol raises a key challenge in fuel cells designed with minimal volume and passive components. One mole of CO_2 is produced for each mole of oxidized methanol. Since CO_2 has limited solubility in methanol, CO_2 bubbles are formed at the anode and reduce the effective anode area, as studied by Yang et al. [26]. CO_2 buildup also causes an increase in pressure inside the DMFC fuel tank which will increase the fuel crossover problem and finally lead to tank or seal rupture. This issue becomes critical for all-passive fuel cells that strive for volumetric efficiency and have no pressure relief mechanism. To further understand the severity of CO_2 accumulations, consider a DMFC with 1 cm^3 head space in the fuel tank. If the cell operates at 20 μA current, and the CO_2 molecules were not vented, the overpressure inside the fuel tank would increase by about 1 psi day^{-1} (7 kPa day^{-1}).

Previous small DMFC studies have evaded this important issue of an efficient mechanism for CO_2 venting [27-29]**.** One approach to deal with the build-up of CO_2 is to design a mechanical pressure relief valve. However, the loss of methanol vapor, complexity of valve design, and space limitations make this approach undesirable. A selective membrane for separation of the carbon dioxide from methanol is preferred because of its size and simplicity. The mechanism of gas transport through polymeric membranes is governed by Knudsen diffusion, molecular diffusion or solution diffusion

[30]. The transport mechanism of a gas or vapor molecule through a polymer layer is a function of the intrinsic interaction among transporting species, polymer matrix and the polymer structure. The overall polymer transport process is broadly dependent on two factors: polymer chain segmental mobility and the presence of defects in the form of voids and pores that influences the diffusion and sorption of a transporting moiety through the polymer [31]. Thus, it is important that the polymer membrane used for gas separation exhibit certain intrinsic properties that facilitate separation. According to Nakagawa et al., these intrinsic properties include high gas permeability coefficient, high separation factor between transporting molecules, the ability to form non-porous thin layer, and chemical and mechanical durability [32].

The polymer matrix must be paired with a fast moving permeate to achieve high gas permeabilities. The transport of a gas molecule through a polymeric matrix depends on the proficiency of small penetrants to diffuse and permeate in response to a gradient in the chemical potential [33, 34]. Additionally, the individual components in a mixture must exhibit a difference in their interaction with the polymer backbone for high separation. As an example, the volatile and non-volatile species in a permeating mixture can interrelate uniquely with the voids and pores in a polymer structure and affect the chain mobility of the polymer backbone. While the non-volatile molecules diffuse through the porous interface of the membrane due to their unique interaction with the polymer backbone, the transport of volatile organic compounds (VOC) entails complex sorption and desorption process. The transport mechanism of VOC across a membrane layer involves three distinct steps: (1) adsorption on the upstream surface of the

membrane, (2) diffusion through the bulk of the membrane matrix, and (3) desorption at the downstream interface of the membrane[35].

Like mentioned before, the mode of transport of a species through a polymer matrix is dictated predominantly by the interaction between transporting moiety and the polymer backbone. Thus to increase the gas separation between a mixture, individual components in the permeating mixture should demonstrate difference in their properties and how they interact with the polymer backbone. With this guideline in sight, the performance of two polymer membranes (i) poly (dimethyl siloxane) (PDMS), and (ii) poly (1-trimethyl silyl propyne) (PTMSP) for designing CO_2 vents have been discussed [36].

2.4 Li-Ion batteries in low power, hybrid power modules

The recent growth in the deployment of ultra low power (< 100 µW average power) wireless devices for sensing and communication has led to the search for a suitable high energy density power supply. Ultra low power direct methanol fuel cells (DMFC) have the promise to provide power with the highest possible energy density. However, micro DMFCs suffer from the same drawbacks as traditional DMFCs and PEM fuel cells for portable power applications, namely their inability to adjust to transient loads with acceptable efficiency. Therefore, many fuel cell systems must rely on a hybrid architecture, such as the one shown earlier in Figure 1, where a secondary energy storage device provides the high current response to the transient load and the fuel cell provides a

steady-state current that operates the circuit controls and recharges the energy storage device.

Secondary lithium ion (Li-ion) batteries are the preferred energy storage device for many high power portable applications including cellular phones, laptop computers, and hybrid electric vehicles. Li-ion cells are the best option for the fuel cell-battery hybrid power source due to their high energy density, good cyclability, and high energy efficiency compared to previous battery technologies, including nickel-cadmium, nickel-metal hydride, and zinc-air. However, Li-ion batteries also suffer from energy losses during cycling and self-discharge, both of which are a function of the state-of-charge. In this hybrid fuel cell-battery application, there are losses due to self discharge and the discharge polarization. The purpose of this study was to evaluate the trade-offs between battery type, state of charge, and battery capacity in order to find the most energy efficient operating condition.

The kinetics of self discharge will vary greatly depending on the battery chemistry, electrode composition and electrolyte formulation. Most Li-ion manufacturers use similar non-aqueous electrolytes, which consist of $LiPF_6$ solvated in linear and cyclic carbonates such as dimethyl carbonate and ethylene carbonate, respectively [37, 38]. The most widely used cathode since the 1990's is Li_xCoO_2 [39-43]. However several other cathodes are used including $Li_xMn_2O_4$ [44-46], Li_xNiO_2 [47, 48], and $Li_xV_2O_5$ [41-43, 46, 49]. In an attempt to provide long shelf life and stable performance during life cycles to batteries, thin film solid electrolytes have been studied widely. One of the more studied versions of thin film Li-ion battery is Lipon cells where "Lipon" refers to lithium phosphorus oxynitride electrolyte [50]. The glassy behavior of the electrolyte imparts

stability upon contact with lithium metal and accounts for their low self-discharge properties. Few studies have also suggested the presence of nitrogen atoms in amorphous matrix of lithium phosphate responsible for increased stability of the system [51].

In a previous study by Johnson and White , it was shown that the self discharge of a commercial Sony 18 650 battery, which has a $LiCoO_2$ cathode, operating at approximately 4.0 V is 11 µA cm^{-2}, which the authors noted as "negligible" [52]. This self discharge current can be considered negligible when the average discharge rate is high, such as a laptop with a 1.2 A-h battery operating at a C/4 discharge. However, in small sensor applications, the steady state current may be only 100 to 500 µA and the battery may only operate at C/4 discharge rate less than 0.1% of the devices' life.

Small Li-ion batteries can be used in hybrid power supply applications, however, they must meet the peak power needs of the system, which can be from 1 mA to 50 mA, without wasting excessive energy through self-discharge. Very small sensors which require only a steady state trickle charge, for example 10 µW, are very vulnerable to self-discharge problems. Over-sizing the battery would waste fuel cell energy in self-discharge while under-sizing the battery would result in system failure because the peak power needs would not be met.

Thus, the self discharge current of Li-ion batteries is an important parameter in designing ultra low power, hybrid power sources. One design parameter of importance in the battery is the active area. It should be as low as possible in order to minimize the self discharge but be large enough to supply the peak power. Many sensors have low average power with short bursts of activity. For example, in many cases the peak current, i_1 (Figure 2.2) can be 1000 times greater than the steady state sleep current, i_2, unlike larger

electronic systems where the current ratio may only be 5:1. Also, the duty cycle is low, i.e. $t_2 >> t_1$.

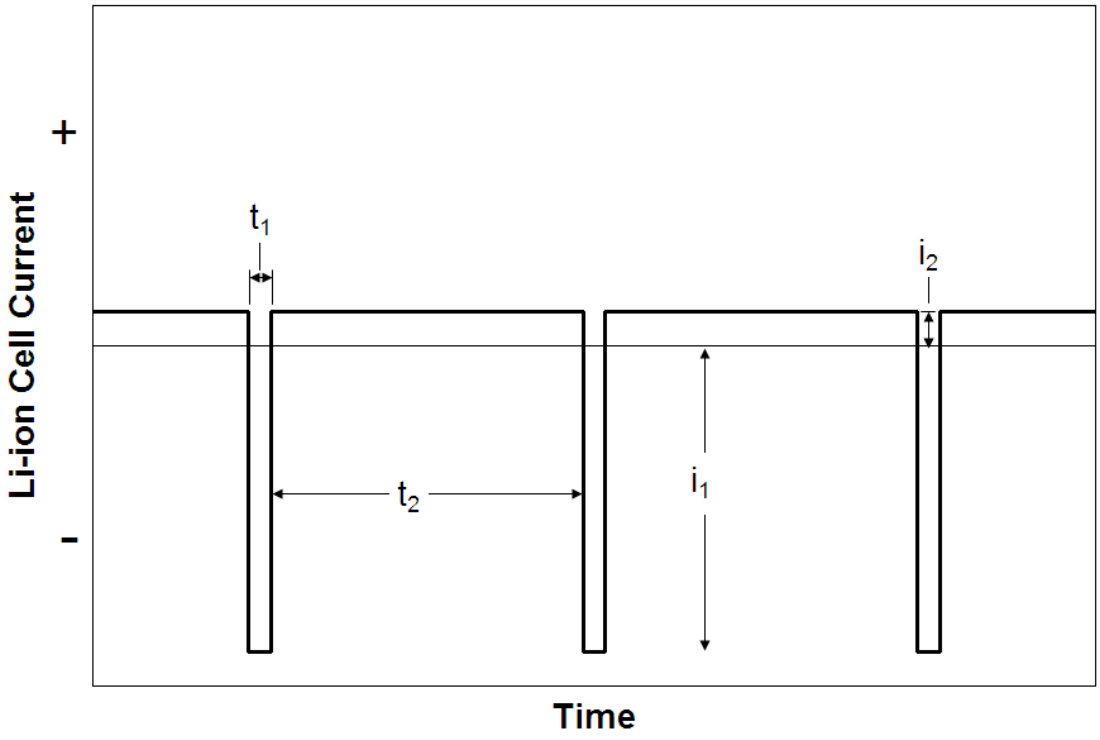

Figure 2.2: Current pulse profile of a secondary Li-ion cell in a hybrid power module

It is clear that the use of Li-ion cells in ultra low power applications is altogether different than their use in larger electronic systems. The depth of discharge during the brief, high current bursts is typically less than 1% of the stored charge. The battery is recharged between events so that the battery spends most of its life a zero net current, except for the recharge current which must be supplied to compensate for self-discharge.

Therefore, cell selection requires a balance between the polarization and self-discharge loss. The goal here is to find the Li-ion technology which can provide brief, high current bursts with as low as possible self-discharge.

CHAPTER 3

EXPERIMENTAL

In this chapter, the experimental procedure related to each key objective is outlined. For the study of PEM systems, the experimental conditions and characterization of glass membranes are discussed. In the case of CO_2 vent membrane, fabrication procedure of polymer vent membranes is outlined and the experimental setup for their characterization has been discussed. Finally, the evaluation processes of batteries are reported.

3.1Glass Deposition

Thin films of phosphorous-doped SiO_2 were deposited on (100) n-type silicon substrates. The first step in preparing the silicate glasses involved metallization of the silicon substrate to provide a conductive plane underneath the glass. For this purpose, a thin layer (200Å) of aluminum metal was deposited on the substrate by DC sputtering. Oxide deposition was carried out using a Unaxis 78324 RF PECVD (plasma enhanced chemical vapor deposition) system operating at a frequency of 13.56 MHz. The semiconductor grade reaction precursors were 5% SiH_4 in He, 1% PH_3 in He and pure N_2O. The SiH_4 and PH_3 flow rates were both kept constant at 200 sccm in order to maintain a molar ratio of phosphorus to silicon at 1:5 in the plasma chamber. The N_2O flow rate was set to one of the two values: 80 and 450 sccm.

For the study of PECVD glass as a PEM film, three deposition parameters: RF power of plasma, substrate temperature and chamber pressure were investigated. First,

the temperature of the metallized silicon substrate was varied from 100 to 200°C while holding the chamber pressure and RF power constant at 400 mTorr and 400 W, respectively. Next, the RF power was adjusted between 100 and 400 W at constant substrate temperature (100°C) and chamber pressure (400 mTorr). Finally, the chamber pressure was varied from 400 to 800 mTorr with a substrate temperature of 100°C and a chamber pressure of 400 mTorr.

The thickness of the deposited phosphorus doped glass film was typically 2 to 3 μm for a 30 minute deposition time. The resulting thin oxide membranes deposited were amorphous in nature and formed translucent films. The ionic conductivity of the films was measured by AC impedance spectroscopy using a Perkins Elmer PARSTAT 2263 electrochemical system with a MSI Electronics Model Hg-412 mercury probe. The frequency range of the impedance measurement was 100 mHz to 1 MHz with an AC signal amplitude of 10 mV. Phosphorus concentration in the films was determined by x-ray photoelectron spectroscopy (XPS) using the Perkin Elmer 540 XPS system. A Perkin-Elmer 1600-FTIR was used to obtain infrared spectra. Refractive index measurements were carried out by Woollam Ellipsometer.

3.2 CO_2 Vent Synthesis and Characterization

A two-part silicone elastomer (base and curing agent, SYLGARD) was obtained from Dow Corning to fabricate PDMS membranes. The elastomer curing agent was added to the base in a 1:10 (wt) ratio. This mixture was mechanically stirred for 30 minutes to ensure complete mixing. This was followed by a 1 hour room temperature

degassing step at18 kPa absolute pressure in a vacuum oven (Isotemp Vacuum Oven, Model 281A). Once the mixture was degassed, it was spin coated on a Teflon substrate to form a thin film using a CEE-100 CB Spinner. The membrane was cured at 100 °C for 1 hour (Fischer Scientific Isotemp Oven). The cured membrane was then peeled off from the substrate.

PTMSP was obtained from Gelest Corporation. It was dissolved in toluene at room temperature, and mixed for 1 week using a rotary mixer. The amount of solvent in the polymer was adjusted to obtain a desired viscosity of the polymer mixture so as to facilitate spin coating. Thin films of the membrane were spin coated on a Teflon substrate. Slow evaporation of the solvent was achieved by placing the cast membrane under a pressure of 90 psia (600 kPa absolute) at 60° C for 3 hours. The resulting membranes were then peeled from the substrate.

Two kinds of additives were mixed with PDMS and PTMSP membranes: 1,9-decadiene (Alfa Aesar) and 1,6 divinyl perfluorohexane (97%) (Matrix Scientific). These additives were included in the polymer mixtures in different weight ratios prior to the curing step. Figure 3.1 lists the chemical structure of PDMS and PTMSP along with the two additives mentioned above.

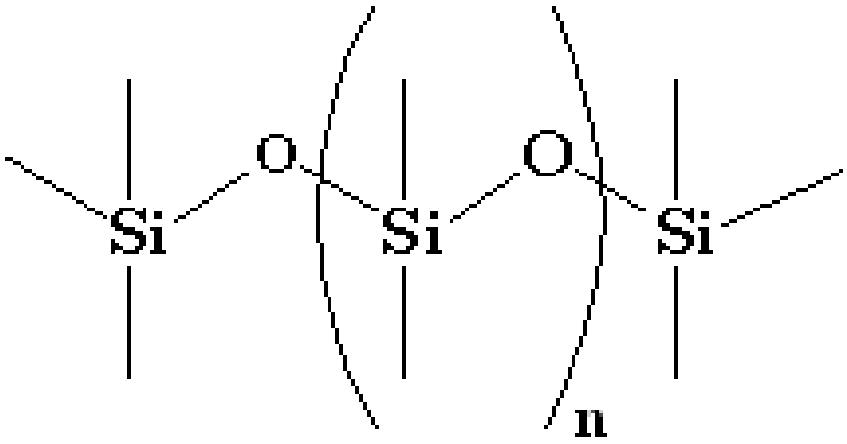

(a) Polydimethyl siloxane (PDMS)

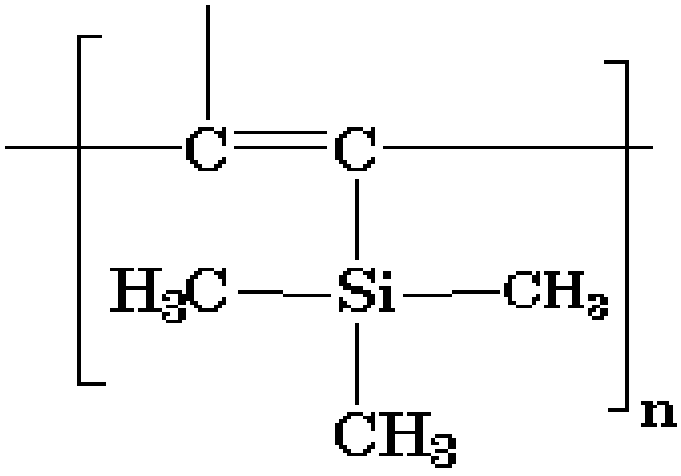

(b) Poly(trimethylsilyl)propyne (PTMSP)

Figure 3.1: Chemical structures of CO_2 vent candidate: (a) PDMS, (b) PTMSP, (c) 1, 6-divinylperluorohexane, (d) 1,9-decadiene

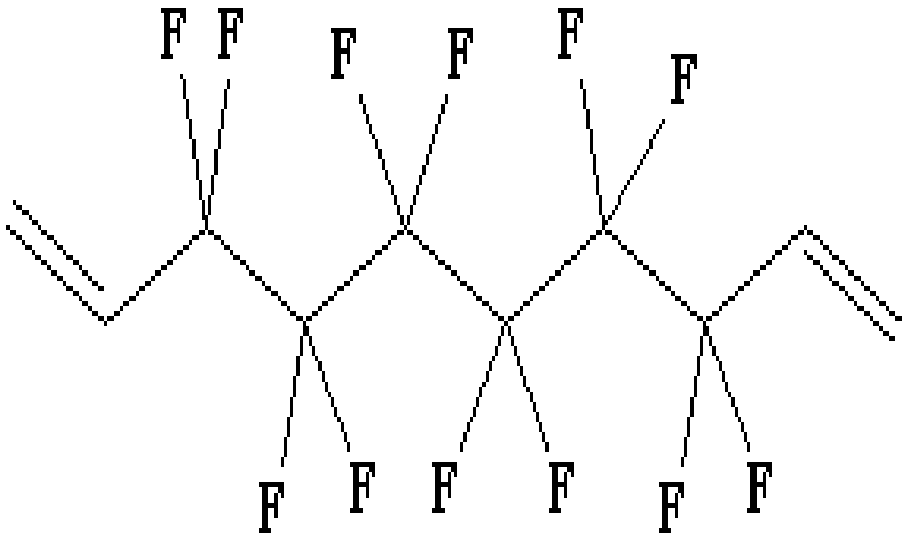

(c) 1,6-divinylperfluorohexane

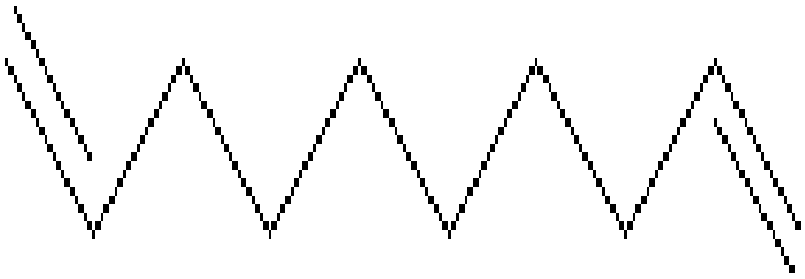

(d)1,9-decadiene

Figure 3.1: Chemical structures of CO_2 vent candidate: (a) PDMS, (b) PTMSP, (c) 1, 6-divinylperluorohexane, (d) 1,9-decadiene

Water contact angle measurements were conducted using the ACT video contact angle system (VCA 2500XE). All measurements were taken using DI water at room temperature. Two sets of experiments were conducted to measure the permeability coefficient of CO_2 and methanol through the polymer membranes. First, the permeability rate of CO_2 and methanol was measured independent of each other and second, the permeability was measured when CO_2 and methanol were both present together as a binary mixture. In each case, the thickness of the fabricated membranes was measured using precision calipers.

In the first experimental setup, the permeation rates of methanol and CO_2 were measured independently. Methanol permeation studies were carried out by methanol gravimetric analysis as methanol was lost from a closed container through a membrane sealed onto a glass vessel. The rate of mass loss of methanol through the PDMS and the PTMSP membranes were recorded as a function of time. All measurements were made at STP. The PDMS membrane used in this experiment was 105 μm thick with an exposed area (to methanol) of 0.352 cm^2. The thickness of the PTMSP membrane was 33 μm with an exposed area of 0.608 cm^2.

CO_2 permeation studies were carried out by measuring the pressure increase due to CO_2 transport through a thin polymer film. The membrane was tightly sealed to a pressure chamber using an o-ring and clamp. The CO_2 which permeates through the membrane was captured in a closed chamber. The upstream pressure of CO_2 was maintained between 2 and 5 psig and the downstream pressure (of the sealed capture chamber) was recorded as a function of time at ambient temperature. The thickness of the

PDMS membrane was 300 μm and the PTMSP membrane was 118 μm with an exposed area of 0.015 cm^2 for each.

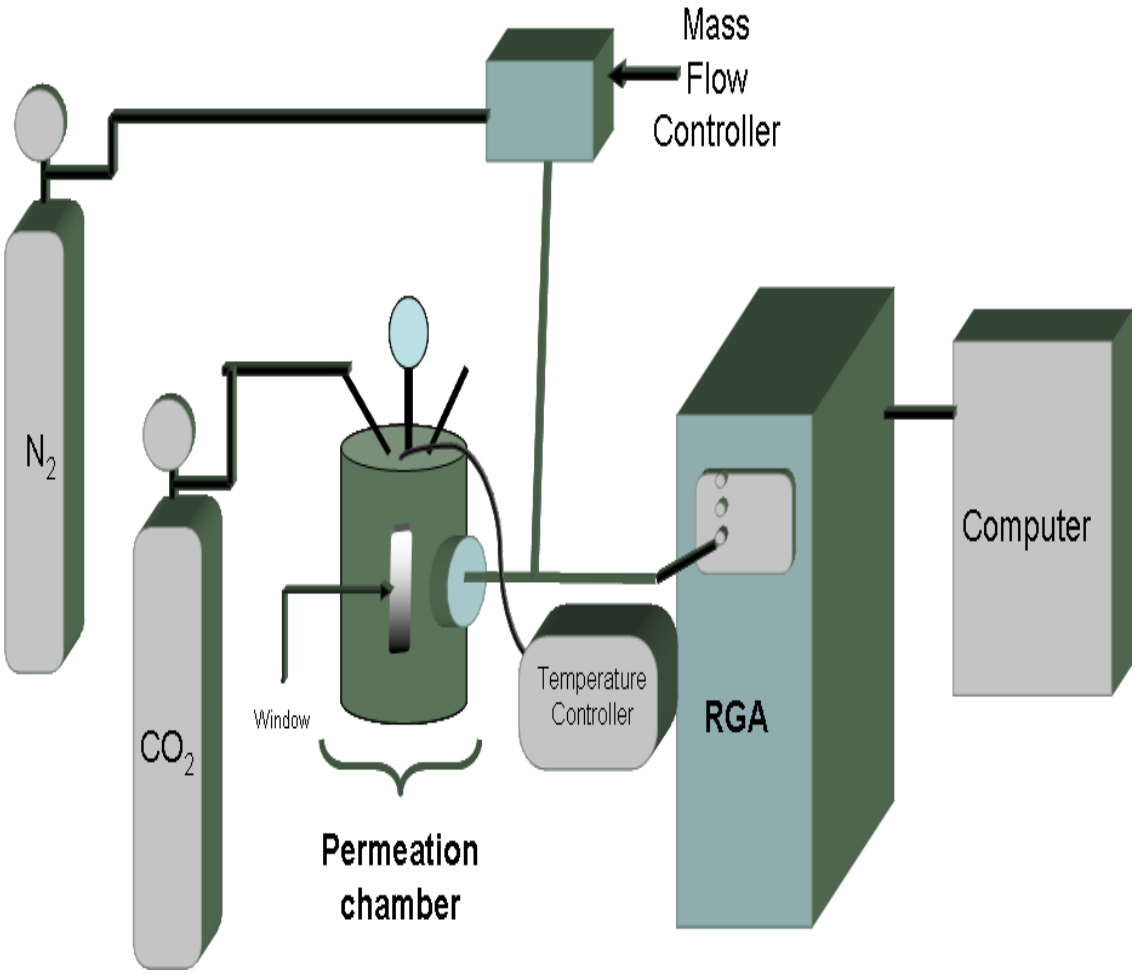

Figure 3.2: Permeation Cell setup.

.

In the second experiment setup, to mimic the true polymer film performance and evaluate the permeability coefficients of CO_2 vent membranes, a permeation cell was constructed to house both methanol and CO_2. This 'binary experiment' is shown schematically in Figure 3.2. The upstream pressure of CO_2 inside the cell was maintained between 4 and 5 psig (28-32 kPa) and the gas inside the permeation cell was saturated with methanol at all times. On the exit or downstream side if the membrane, nitrogen was used as a sweep gas to carry permeates from the membrane to a quadrapole mass spectrometer. The rate of CO_2 and methanol permeation through a 255 μm thick PDMS membrane having an area of 2.85 cm^2 was measured. A similar permeation experiment was conducted for a 120 μm PTMSP membrane, with an area of 2.85 cm^2.

Small, 0.5mm x 0.5mm membrane samples were prepared for thermogravametric analysis (TGA) using a TA Instruments TGA Q500. The temperature was ramped at 10 °C-min^{-1} and the N_2 flow rate was maintained at 90 ml min^{-1}. The permeability coefficient of CO_2 and methanol were measured using a quadruple mass spectrometer QMS 100 Series Gas Analyzer by Stanford Research Systems. The QMS was paired with a pressure vessel and a 4836 Parr Temperature controller as shown in Fig. 3.2.

3.3 Battery Characterization

Ten low capacity Li-ion coin-type cells were used in this investigation. Each study used a minimum of three cells. The response across each set of cells was consistent. In order to maintain similarity between the electrode and electrolyte a single manufacturer, Panasonic, was used for nine of the cells. In order to look at the effect of

the electrolyte, a thin film LiPON electrolyte cell was purchased from Front Edge Technology, Inc. The physical parameters of the commercial cells is presented in Table 3.1.

Table 3.1: Properties of tested Li-ion cells.

Cell	Cathode	Electrolyte	Manufacturer	Nominal Capacity (mAh)	Diameter (mm)	Height (mm)	Active Diameter (mm)	Active Area (cm2)
ML414	MnO2	organic	Panasonic	1.2	4.8	1.4	2.9	0.07
ML621	MnO2	organic	Panasonic	5.0	6.8	2.1	4.2	0.14
ML1220	MnO2	organic	Panasonic	17.0	12.5	2.0	1.0	0.71
ML2020	MnO2	organic	Panasonic	45.0	20.0	2.0	1.6	1.9
VL621	V2O5	organic	Panasonic	1.5	6.8	2.1	0.5	0.17
VL1220	V2O5	organic	Panasonic	7.0	12.5	2.0	1.0	0.74
VL2020	V2O5	organic	Panasonic	20.0	20.0	2.0	1.6	2.1
VL2320	V2O5	organic	Panasonic	30.0	23.0	2.0	2.0	3.1
VL2330	V2O5	organic	Panasonic	50.0	23.0	3.0	2.0	3.1
NX0201	CoO2	LiPON	Front Edge Technology	0.4	N/A	0.2	N/A	3.5

All electrochemical measurements were made with an Arbin battery test system. For each experiment, new cells were used in order to eliminate the effect of capacity and performance fading caused by cycling.

In order to confirm the cell capacity, cycling tests were done between 2.5 and 4.2 V in the galvanostatic mode with charge and discharge currents of 100 μA. Following cycling, the cells were dissected and the normalizing area for all other experiments was taken as the cathode geometric area. Cell polarization and charge-loss experiments were conducted by charging the cells at 1/100 C to the desired voltage. Four cell voltages were of interest in this study: 3.5, 3.75, 4.0 and 4.2 V. For the polarization experiments, the cells were immediately discharged (immediately following the charge cycle) at 1/10, 1/5, 1/2, 1, or 2 C relative to their rated capacity for 1 s. The cells were recharged at 1/100 C until the original voltage was achieved and the charge/discharge cycle was repeated 50 times with each cell. The discharge potential was taken as the peak (minimum) value measured using the Arbin system. The value reported here was calculated by taking the mean of the final five discharge values for each of the tested cells.

The self discharge rate of the battery during hybrid power source operation was investigated by cycling at four discharge rates. The cell was first charged to one of four voltages of interest: 3.5, 3.75, 4.0 or 4.2 V. The cell was then discharged for 100 s at constant current. The cell was then recharge at the same current as that used in the discharge until the original cell voltage was reached. The recharge time was greater than 100 s and the time varied based on cell size, chemistry and charge/discharge current. For smaller cells, with capacities lower than 20 mA-h, the cells were discharged and

recharged at 2, 6, 8 and 10 μA. For larger cells, the current was increased by a factor of either 2 or 5.

CHAPTER 4

PROTON EXCHANGE MEMBRANE (PEM) FOR DIRECT METHANOL FUEL CELLS

4.1 Objective

This chapter discusses the performance of a phosphorus doped silicon dioxide glass (PSG) as ion exchange membrane. Phosphorus doped silicon dioxide glass (PSG) was deposited via plasma enhanced chemical vapor deposition (PECVD). The effect of plasma deposition parameters, substrate temperature, RF power, and chamber pressure, on the ionic conductivity of the PSG films is elucidated in this chapter. The objective of this chapter is to present optimized plasma deposition condition for high ionic conductivity. The work presented in this chapter has been previously published in the Journal of Power Sources [53].

4.2 Results and Discussion

Figure 4.1 shows the ionic conductivity of PECVD deposited PSG thin films as a function of substrate temperature at constant RF power and chamber pressure. The samples were prepared at an RF power of 400 W and a pressure of 400 mTorr. The trend observed in Figure 1 indicates that increasing the deposition temperature leads to a decrease in the conductivity of PSG films.

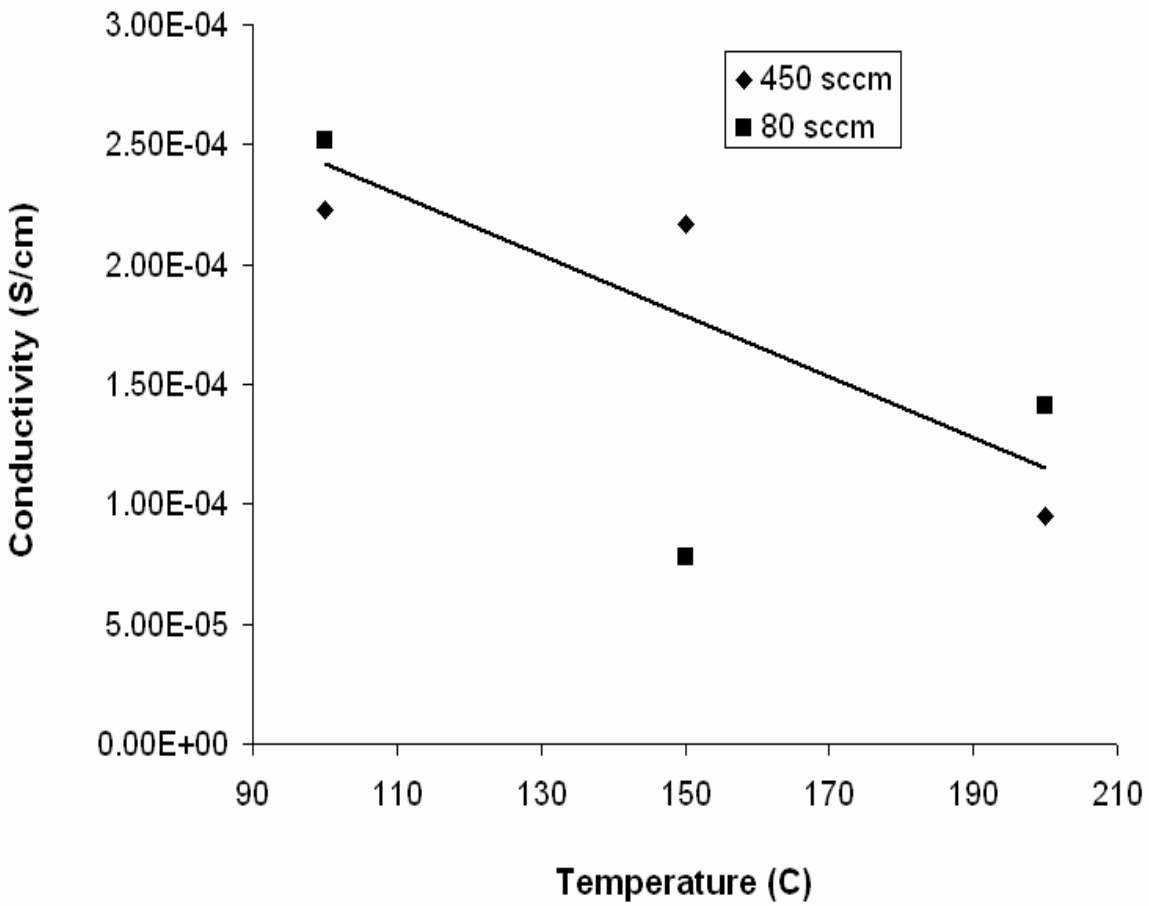

Figure 4.1: Ionic conductivity of P-doped SiO_2 thin films as a function of substrate temperature at 400 mTorr chamber pressure, 400 W RF power and N_2O flow-rates of 80 and 450 sccm

This trend can be explained by two factors. First, it has been well established that the silane oxidation reaction can proceed through two reaction pathways, the complete oxidation to SiO_2, Equation 4.1, or the so-called non-bridging defect SiOH structure, where at least one of the oxygen bonds is not condensed.

$$SiH_4 + 4N_2O \rightarrow 4N_2 + SiO_2 + 2H_2O \tag{4.1}$$

Since the ionic conductivity of the silicate glasses is a function of the defect content of the prepared film[14], the reaction selectivity is a key control parameter. Due to differences in the activation energy of these two reactions, if a typical Arrhenius expression is assumed, the selectivity will be an exponential function of the temperature, shown in Equation 4.2.

$$S \equiv \frac{r_{SiOH}}{r_{SiO2}} = A\exp\left[\frac{E_{SiO2} - E_{SiOH}}{RT}\right] \tag{4.2}$$

Where S is the reaction selectivity, r_i is the overall reaction rate, R is the ideal gas constant, T is the reaction temperature in Kelvin and E_i is the reaction activation energy. Since the activation barrier for the complete condensation reaction is greater than that for silanol, it is clear from Equation 4.2 that at low temperatures the selectivity increases, leading to an increase in the ionic conductivity, which is in agreement with previous observations by Abe and coworkers[15].

Second, it has already been established that the ionic conductivity of silicate glasses is enhanced by the presence of secondary oxides formed by doping with Group V elements including phosphorus and the amount of phosphorus that gets incorporated in the glass matrix directly influences the ionic conductivity of the deposited PSG films. Similar to the previous discussion, the relative reaction rates for the phosphorus and silicon precursor species is also a function of the substrate temperature due to changes in

the selectivity between the total reaction rate of silane and phosphine, Equations 4.1 and 4.33, at the surface. However, it should be noted that during the phosphorus oxidation, incomplete condensation can also occur, forming defect P-OH bonds that may increase the ionic conductivity[54].

$$2PH_3 + 8N_2O \rightarrow 8N_2 + P_2O_5 + 3H_2O \tag{4.3}$$

Figure 4.2 shows the phosphorus content of the prepared films as a function of substrate temperature. It is observed that as the temperature of the substrate increases, the phosphorus content in the film decreases, leading to a decrease in the number defect sites at elevated temperature and, hence, the ionic conductivity.

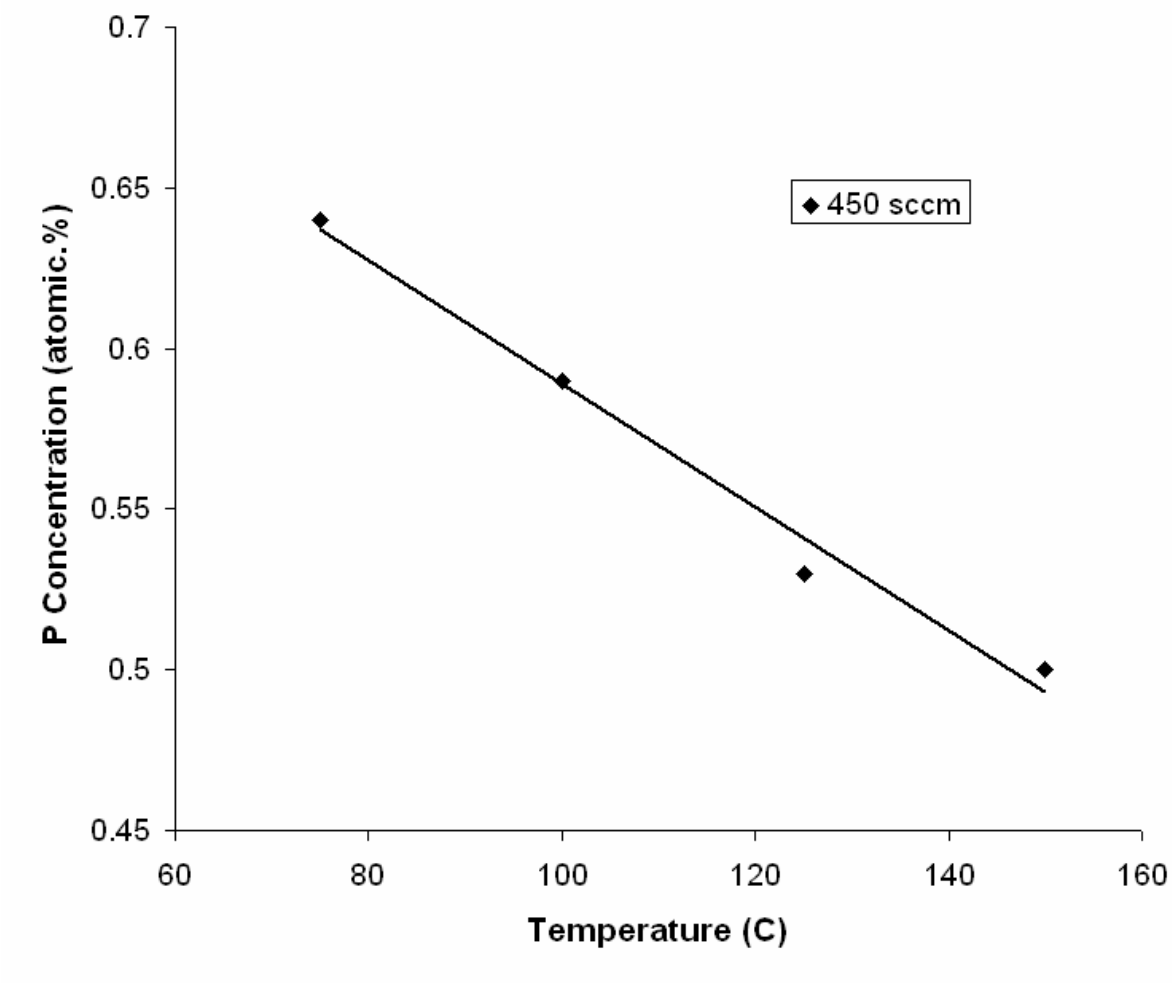

Figure 4.2: Phosphorus content of PSG films as a function of substrate temperature at 400 mTorr chamber pressure, 400 W RF power and 450 sccm N_2O flow-rate.

Furthermore, Digiovanni et al. have shown that at high temperature, the thermal activity of phosphorus causes it to volatilize into the gas phase, thus decreasing the overall content of P-OH bonding in the glass network[55]. Since the P-OH moiety is more acidic in nature than silanol (Si-OH), a decrease in phosphorus content could lead to a decrease in the conductivity of the deposited film, other factors remaining equal.

Also, Nogami and coworkers have shown that the activation energy of proton disassociation from Si-OH bonds is much higher than that of P-O-H making –P-OH more acidic unit[56]. Visual inspection of the PSG samples also showed that films deposited at higher temperature tended to crack due to thermal expansion mismatches with the metallized substrate.

Finally, at higher temperatures, the substrate surface is activated leading to an increase in the kinetic energy of the reactive ions on the surface. Chapple-Sokol et al. showed that in the plasma deposition of pure silicon dioxide at elevated temperature, the formation of hydroxyl bonds may be inhibited due to thermal activation of the surface[14]. Also as the temperature increases, the residence time of the reactants on the surface decreases due to the accelerated rate of collisions and high kinetic energy of moieties at the heated substrate. This low residence time of the reactants on the substrate forces the reaction to take place in the gas phase and the depletion of reactants at the growing surface of the substrate causes a decline in the overall deposition rate of glass at higher temperature, as shown in Figure 4.3. Thus, low temperature deposition results in thinner films with higher intrinsic conductivity.

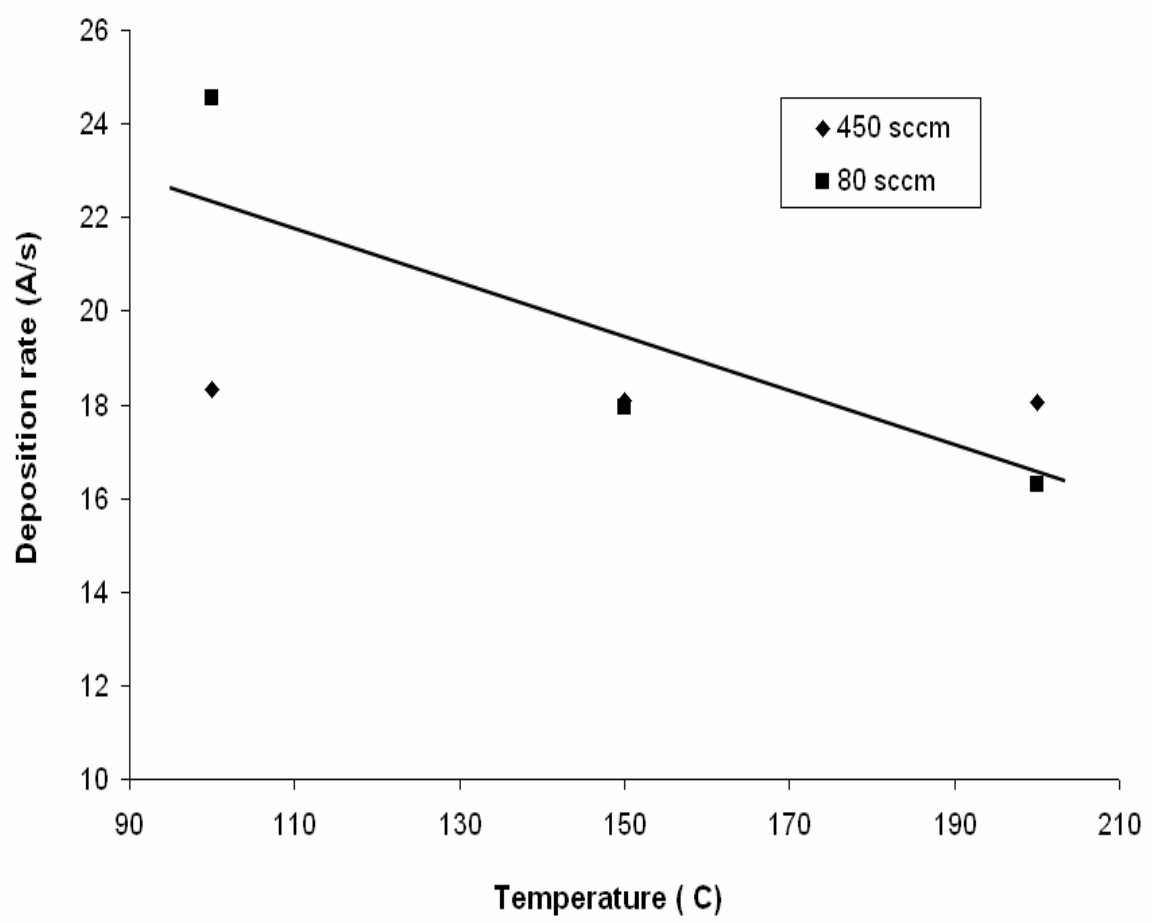

Figure 4.3: PSG deposition rate as a function of substrate temperature at N_2O flow-rates of 80 and 450 sccm, 400 mTorr chamber pressure, 400 W RF power

Next, the effect of the RF plasma power on the film properties was investigated by depositing glass films at two N_2O flow rates, 80 and 420 sccm, while maintaining the same silicon to phosphorus ratio. The plasma chamber pressure was held at 400 mTorr and the substrate temperature was set to the optimum value obtained in Figure 1, 100^{o}C. Increasing the RF plasma power results in a steady rise in the conductivity of the

deposited PSG films, as shown in Figure 4.4. The phosphorus concentration, estimated by XPS, as a function of RF power is shown in Figure 4.5.

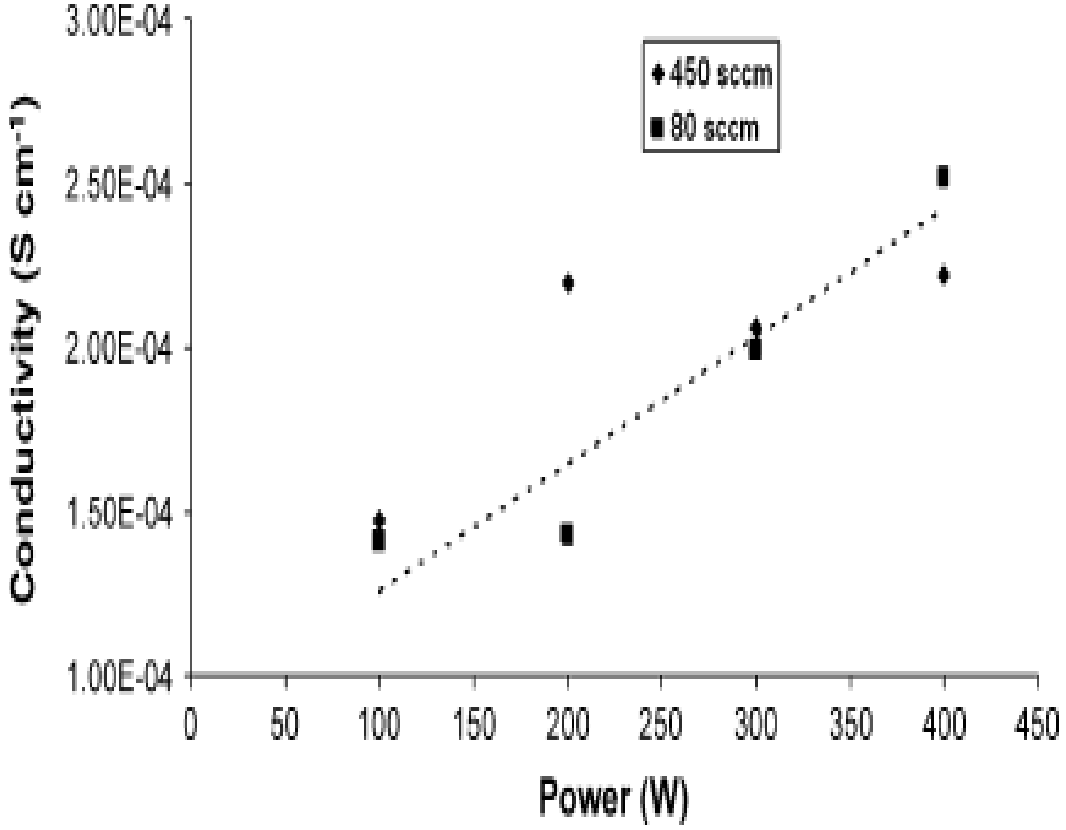

Figure 4.4: Ionic conductivity as a function of PECVD RF power at 100°C substrate temperature, 400 mTorr chamber pressure and N_2O flow-rates of 80 and 450 sccm

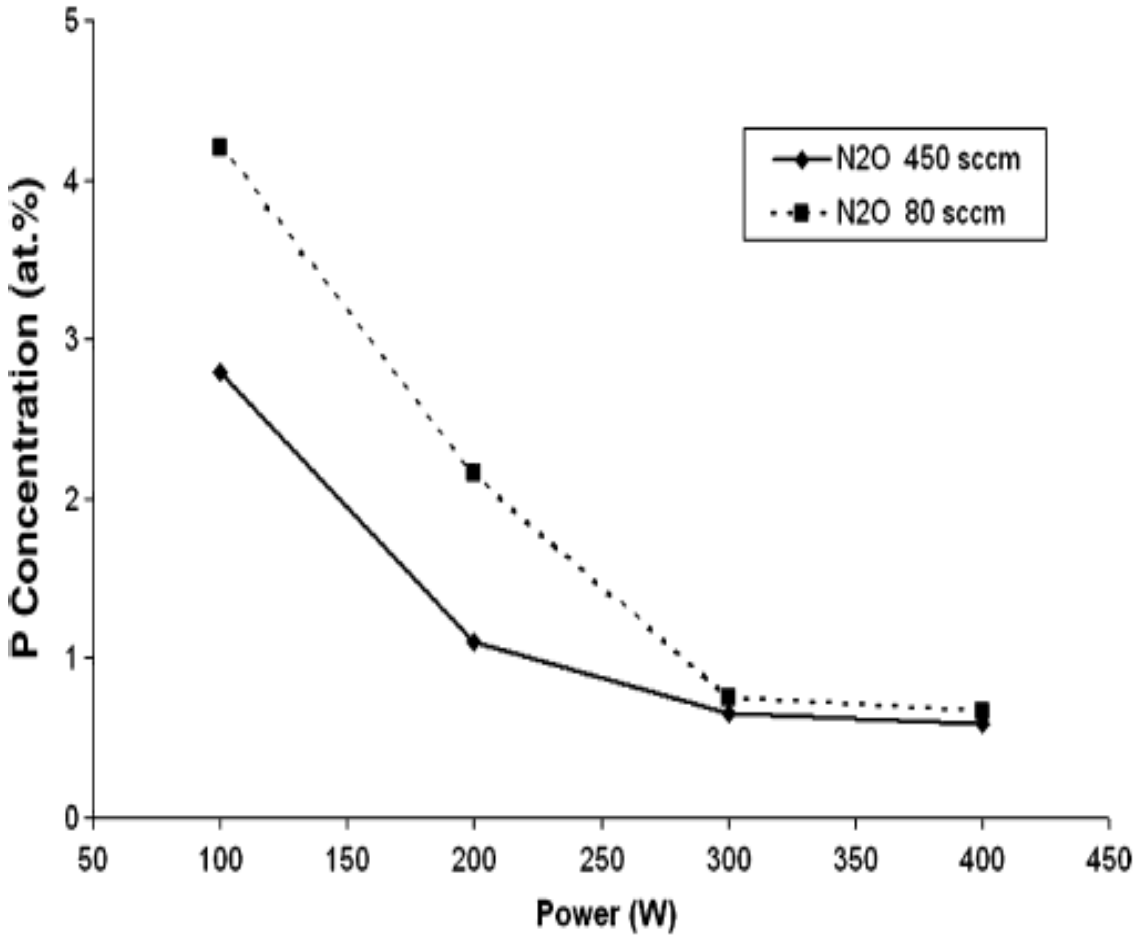

Figure 4.5: Phosphorus concentration determined by X-ray Photoelectron Spectroscopy as a function of RF power at 100^{o}C, 400 W and N_2O flow-rate of 80 sccm.

Figure 4.5 shows that the phosphorus content in the prepared films decreases as plasma power increases. The decrease in phosphorus content at higher RF power likely originates from the differences in the disassociation energy between SiH_4 and PH_3. Phosphorus is more electronegative than silicon meaning that the bond disassociation energy of PH_3 is higher than that of SiH_4. At high RF power, the fraction of SiH_4

undergoing disassociation is comparatively higher than PH_3 and hence the overall phosphorus concentration decreases. It is also observed that the ionic conductivity of the film increases with decreasing phosphorus content. This appears to be a direct contradiction to earlier results; however, it was previously noted that imperfections in pure silicate glass from incomplete oxidation also lead to the formation of conductive species in the form of –OH. Therefore, the hydroxide concentration in the films was analyzed by examining the –OH stretch in the FTIR spectra.

Figure 4.6 shows the FTIR spectra for PSG films prepared with 80 sccm N_2O flowrate at 200, 300 and 400 W. Two important observations can be made. First, the P=O stretch at 1400 cm^{-1} decreases with increasing power, in agreement with the XPS results that the phosphorus content decreases with RF power. Second, the films deposited at higher power showed a greater hydroxide concentration, as evidenced by increased area under the broad peak observed for all samples in the 3000-3300 cm^{-1} range.

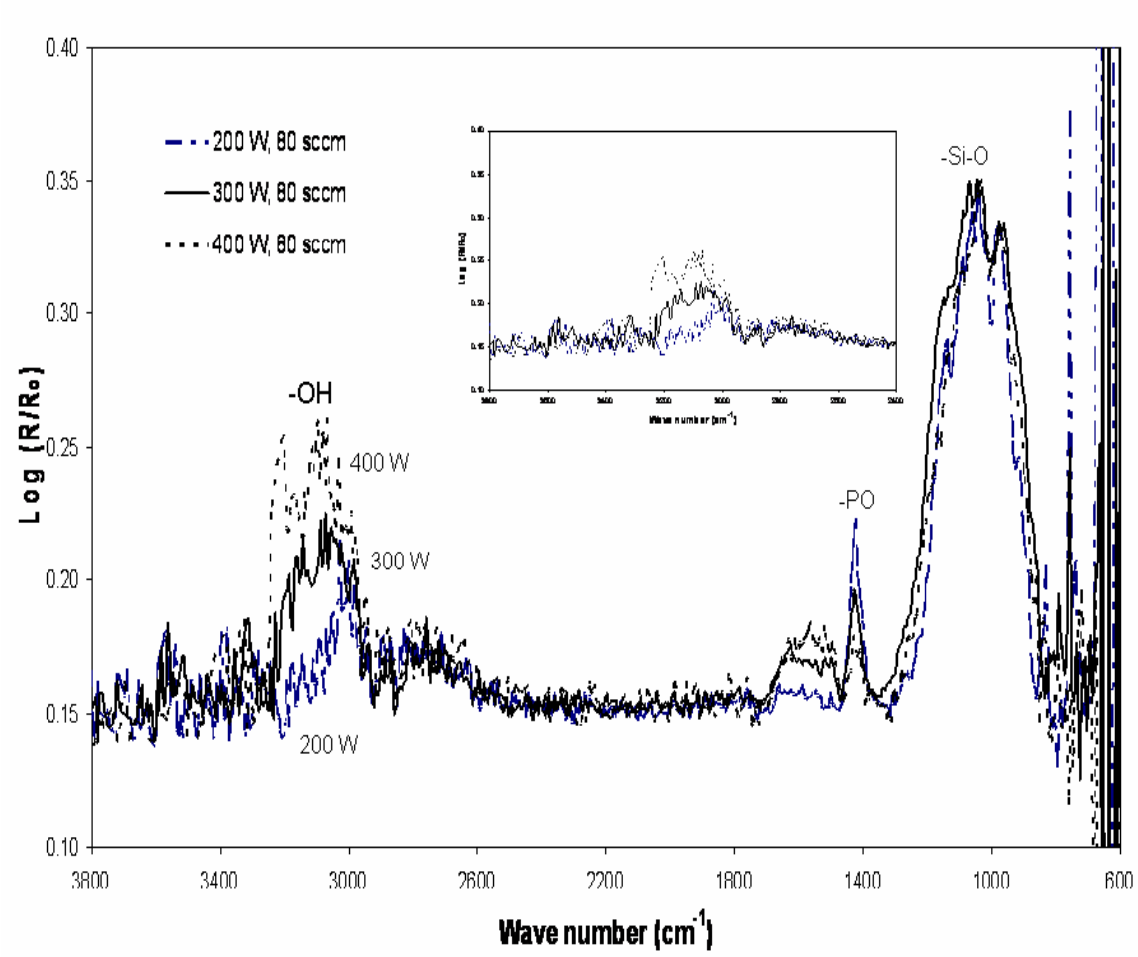

Figure 4.6:Fourier Transform Infrared spectra of PSG films prepared with RF powers of 200, 300 and 400 W with a 100^{o}C substrate temperature, 400 mTorr chamber pressure and 80 sccm N_2O flowrate

It is also observed that the density of reactive ions in the plasma is a function of plasma power. At higher plasma power, the numbers of reactive ions present in the plasma increases, which results in a more rapid and imperfect oxide formation. This increase in the glass deposition rate, shown in Figure 4.7, points to an increase in the reaction selectivity, Equation 4.3, indicating that more non-bridging moieties have been

formed. Thus, the faster deposition rate results in an increase in the defect density and the enhancement from the elevated –OH content appears to counteract any decrease in the ionic conductivity that is caused by a decrease in phosphorus content.

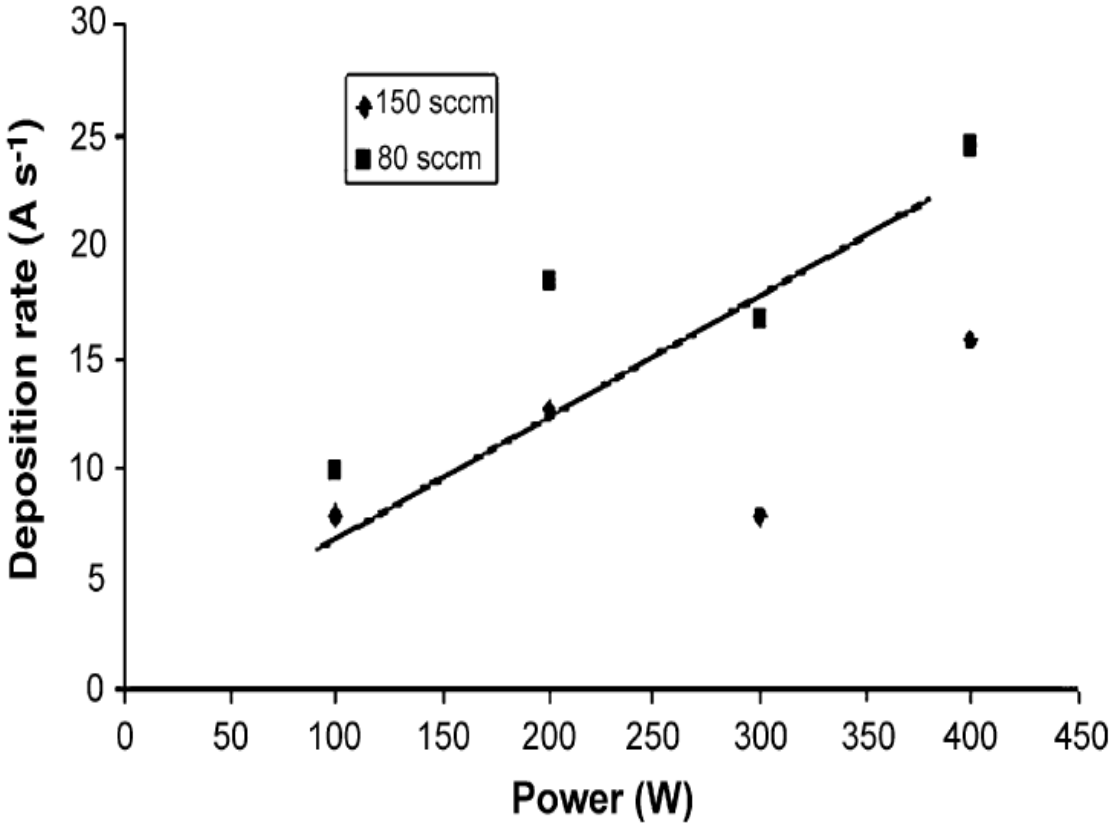

Figure 4.7: P-doped glass deposition rate as a function of RF Power at 100^{o}C, 400 mTorr and N_2O flow-rates of 80 and 450 sccm.

The ionic conductivity of the deposited PSG films as a function of chamber pressure at constant substrate temperature and RF power is presented in Figure 4.8. The temperature and RF power for each of the experiments was 100^{o}C and 400 W, respectively, and corresponds to the peak values obtained in Figures 4.1 and 4.4. It is observed that increasing the pressure from 200 to 400 mTorr, results in higher ionic conductivity. However on further increasing the pressure, the conductivity decreased.

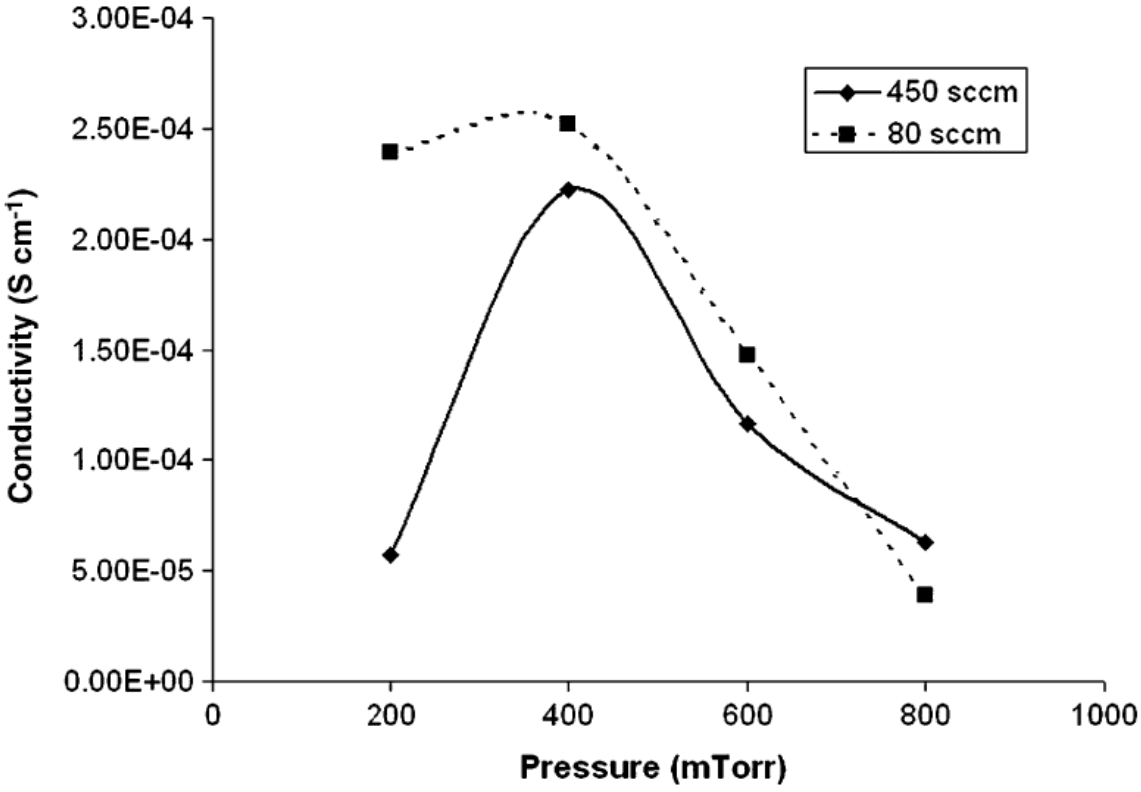

Figure 4.8: Ionic conductivity of prepared PSG thin films as a function of chamber pressure at 100^{o}C substrate temperature, 400 W RF power and N_2O flow-rates of 80 and 450 sccm.

It is also observed that increasing the chamber pressure resulted in a decrease in refractive index of the film, shown in Figure 4.9. According to Ceiler et al., as the polarity of molecules in a material decreases, the light velocity through the material also decreases, yielding reduced values for the material refractive index[25]. The decrease in refractive index observed at high pressure, as shown in Figure 4.9, indicates that as the pressure is increased inside the plasma chamber, the amount of polar species, most likely -OH, incorporated in the glass matrix decreases; thus lowering the conductivity of the films.

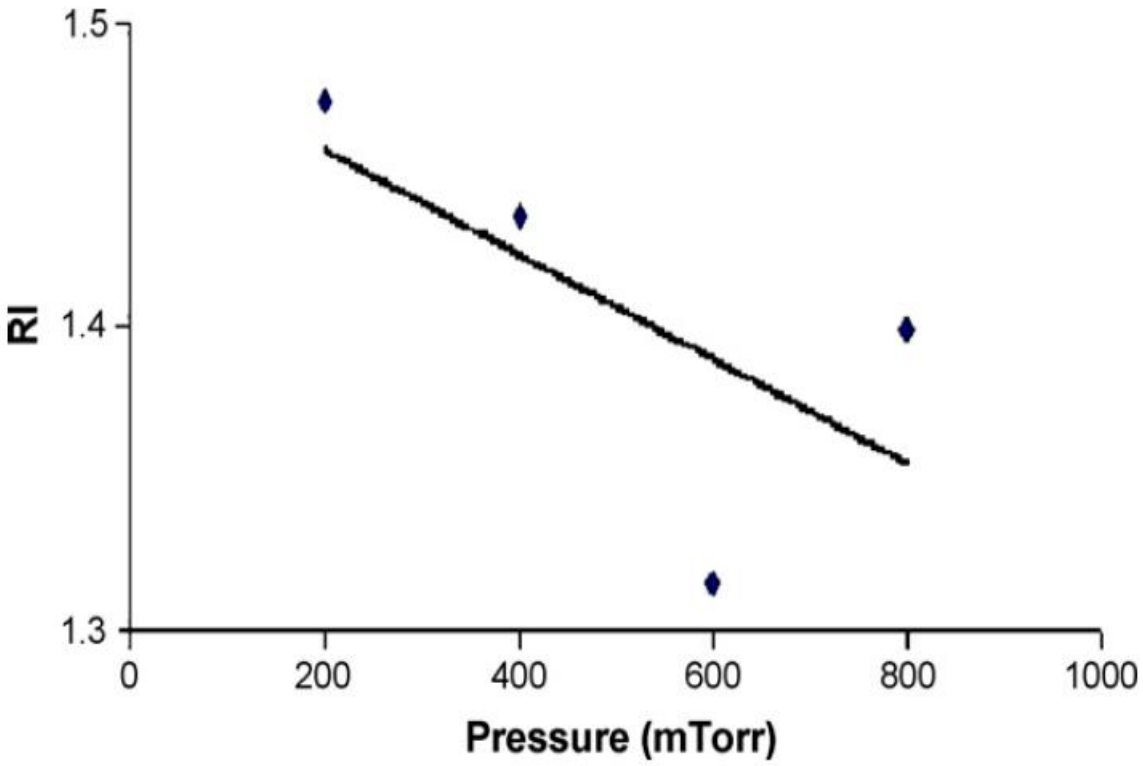

Figure 4.9: Refractive Index as a function of chamber pressure at N_2O flow rate of 450 sccm, 100^{o}C and 400 W

The PSG deposition rate with pressure is given in Figure 4.10. Apart from the initial increase, the deposition rate was not a strong function of pressure, though a slight decrease was observed. Diffusion models prepared by Dobkin et al. confirms that with increasing pressure, the deposition rate of oxides increases before stabilizing at high pressures[57]. Models prepared by the authors indicate a large increase in deposition rate until pressure reaches approximately 400 mTorr, in agreement with what is observed in Figure 4.10.

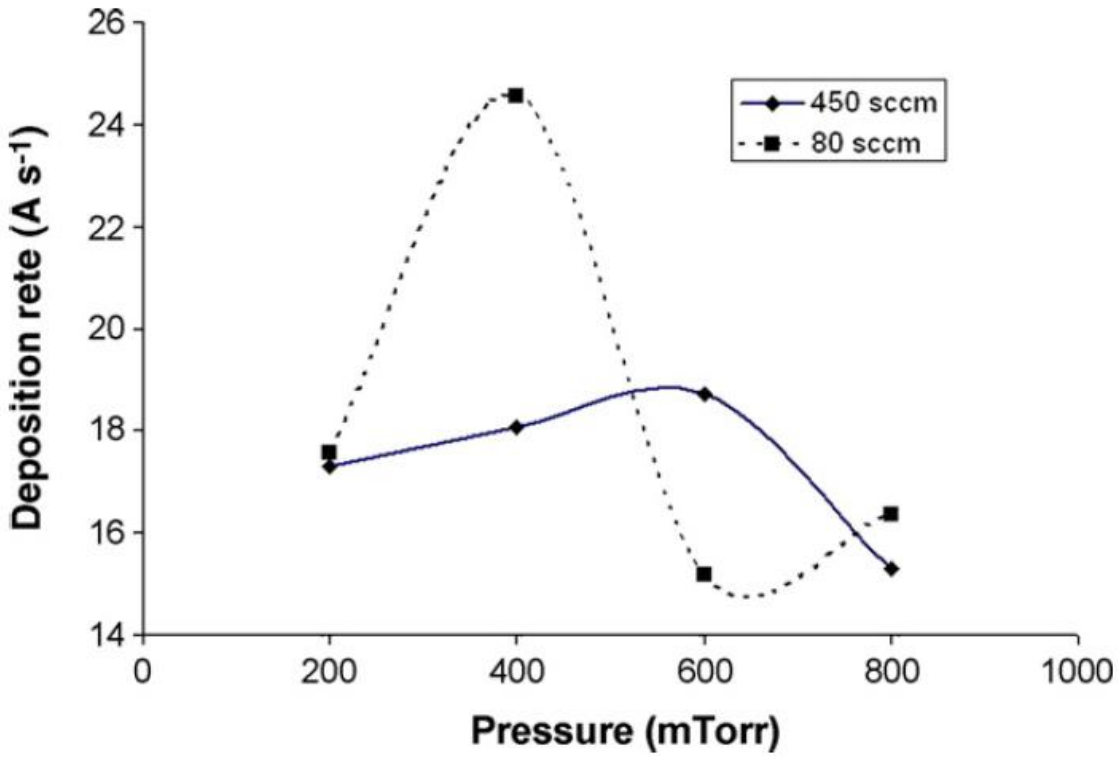

Figure 4.10: Phosphosilicate glass deposition rate as a function of chamber pressure at a substrate temperature of 100^{o}C, 400 W RF power and N_2O flow-rates of 80 and 450 sccm

Hey et al. have shown that at higher chamber pressures, the number of collisions between reactive ions increases[58]. The authors explain that with every subsequent collision, the reactive ion lose energy and come in close vicinity of each other, thus reducing the mean free path between them. This promotes the reaction to take place in gas phase in preference to that on the substrate. This explains the observed decrease in the deposition rate with pressure and the corresponding decrease in conductivity of the films. The phosphorus content of the films was also investigated by XPS and the results are presented in Figure 4.11. It is clear that the phosphorus content of the prepared films steadily decreases with pressure, which further explains the observed decline in conductivity.

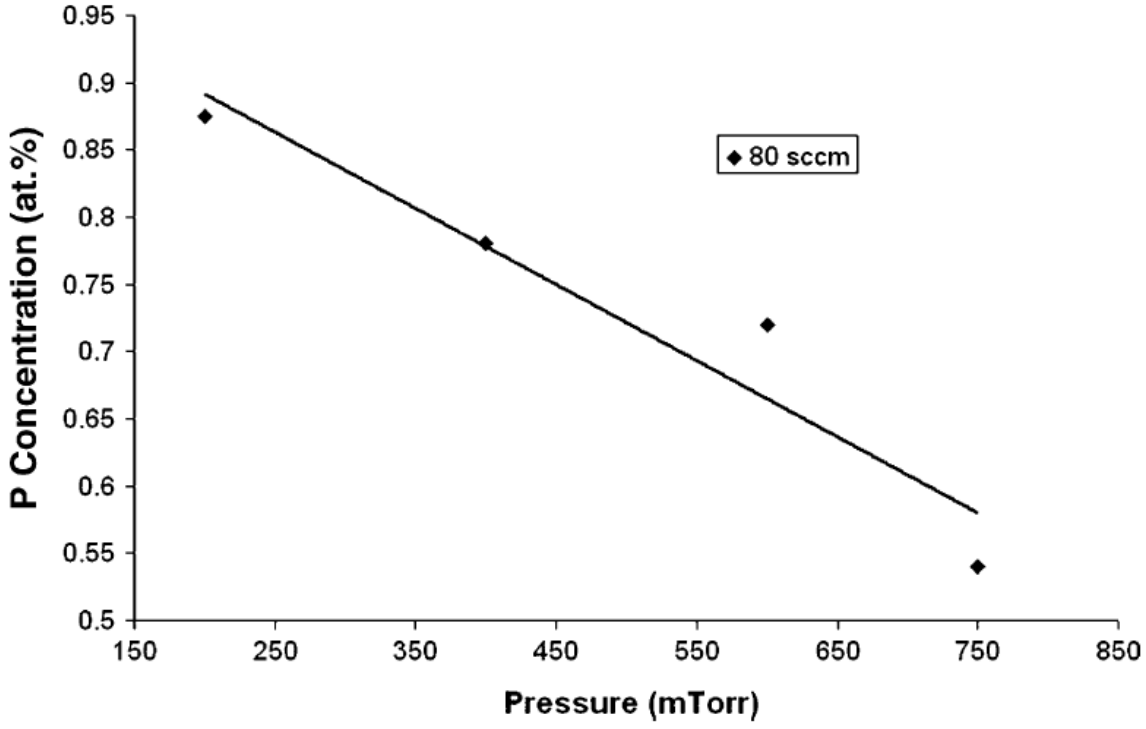

Figure 4.11: Phosphorus concentration as a function of chamber pressure at 100^{o}C substrate temperature, 400 W RF power and N_2O flow-rate of 80 sccm.

To characterize the performance of PSG as a proton exchange membrane, DMFCs with PSG-Nafion hybrid electrolyte membrane were fabricated. For this purpose, porous glass substrates (1 mm in thick) were first soaked in 5% Nafion solution and cured at 150 °C. The Nafion-filled substrates were then exposed to plasma and 3 μm of PSG membrane was deposited at the plasma conditions that showed the maximum ionic conductivity; 100 °C substrate temperature, 400 W RF power and 400 mTorr chamber pressure. The anode (PtRu/C) and cathode (Pt/C) catalyst layers were prepared by painting typical catalyst inks, which contained 30 weight percent Nafion solids. Gold paint was used as the current collector on both anode and the cathode. The passive delivery of fuel (methanol) to the electrolyte was achieved by attaching a methanol tank to the composite electrolyte filled substrate such that the painted anode was in contact with methanol and cathode was exposed to ambient air. To compare the performance of the DMFC made with Nafion-PSG composite membrane to those made with just Nafion, a fuel cell was constructed in the same manner as has been mentioned before except the no PSG was deposited on the substrate.

Polarization curves for both Nafion and PSG-Nafion hybrid membrane passive DMFCs are given in Figure 4.12. Both polarization curves were measured at room temperature (23^{o}C) with 12 M aqueous methanol fuel. It is clear from Figure 4.12 that the performance of the DMFC is markedly improved with the hybrid membrane. The open circuit voltage has been increased by approximately 65 mV and the current density at 0.4 V has nearly tripled. The improvement in the performance is likely due to lower methanol permeation through the PSG film when compared to Nafion alone. This is evident in the increase in the open circuit voltage where less internal short circuiting is

observed. Also, the current density is improved by the lower crossover by removing methanol and methanol oxidation intermediates from the catalyst surface. The reduced methanol crossover also limits the amount of water that is transported from the anode to cathode, which could lead to local flooding issues within the electrode structure.

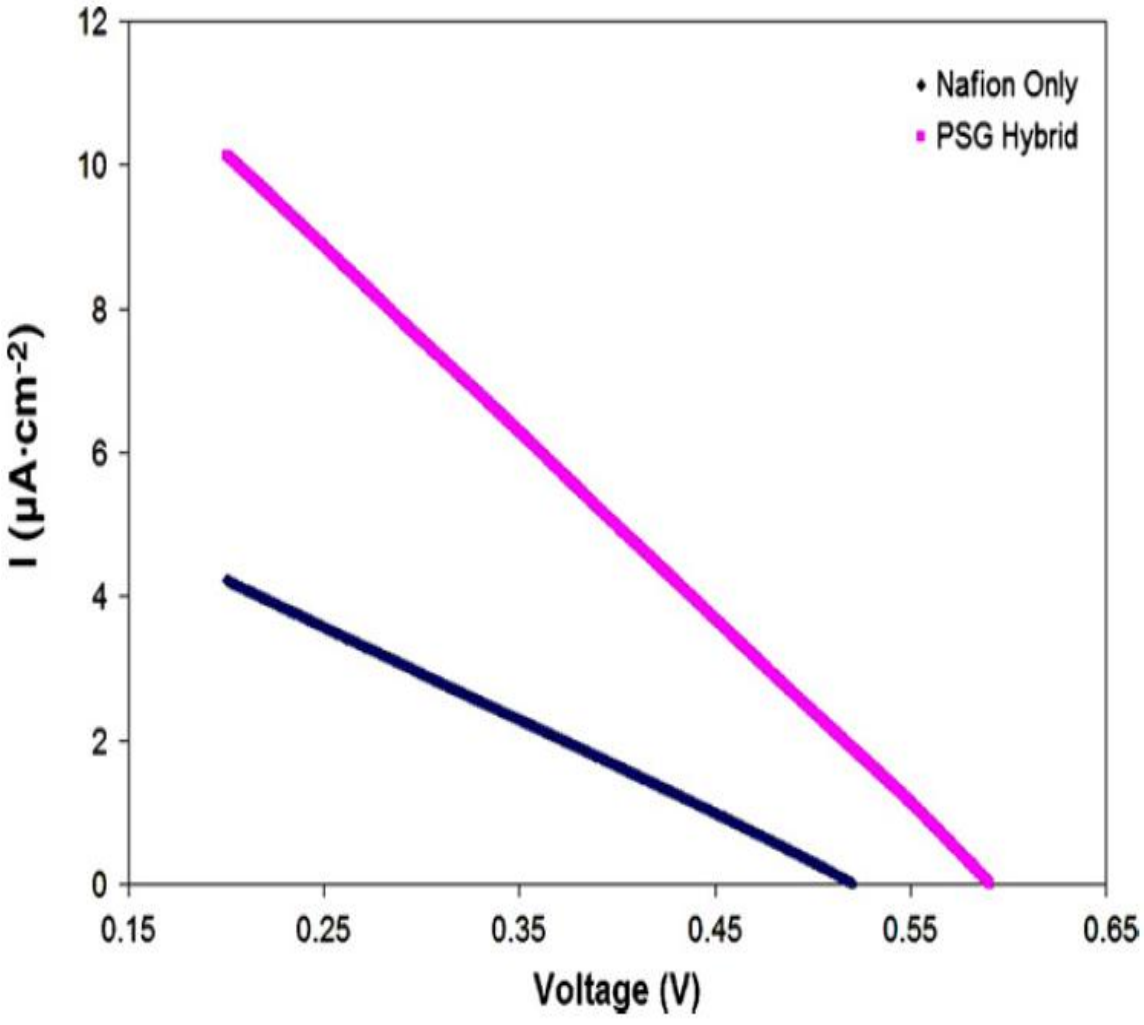

Figure 4.12: Polarization experiments for fully passive DMFCs with PSG-Hybrid and Nafion electrolytes; 23^{o}C, 12 M methanol, 10 mV/s.

The steady state performance of the DMFC was also measured and is presented in Figure 13. The cell was operated under a constant load of 76 kΩ at room temperature and 12 M methanol fuel. It was observed that the cell performance is quite stable, even following refueling, indicating that the hybrid membrane maintains stable ionic performance over the device life.

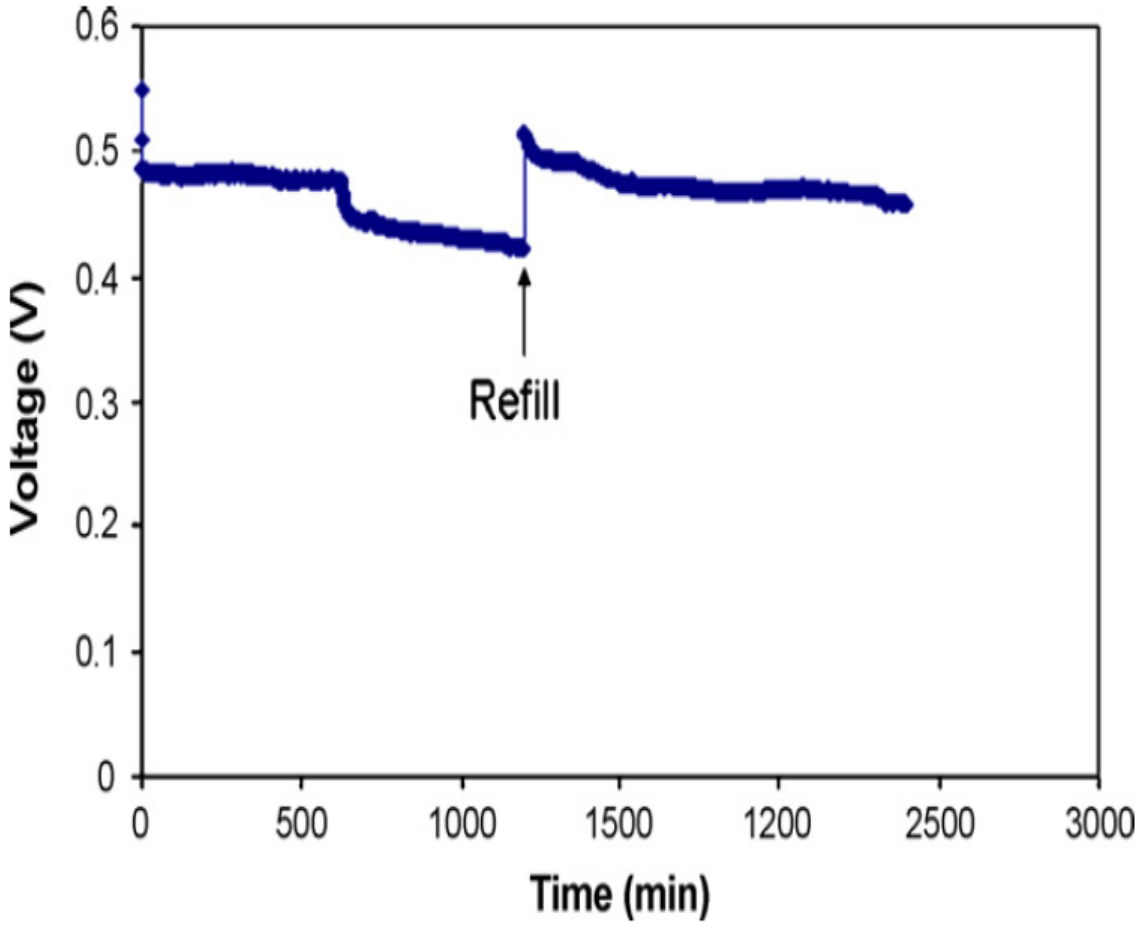

Figure 4.13: Steady-state performance of the passive DMFC with PSG-Hybrid proton-conducting electrolyte; 76 kΩ load, 23^{o}C, 12 M methanol.

Figure 4.13 shows that from 700-1300 min of operation, the cell voltage dips by approximately 10%. This is most likely due to the entrapped carbon dioxide bubles at the anode surface, which leads to a reduction in the electrochemically active surface area, and the voltage under constant load declines. As the tank is refueled, at ~ 1300 min. of operation, the CO_2 bubbles are released and the voltage is increased above the initial operating cell potential. This increase is most likely a result of catalyst activation over time.

4.3 Summary

PSG films were deposited by PECVD and a systematic variation of deposition conditions was carried out in order to optimize the plasma for both high film quality and ionic conductivity. The results presented in this chapter indicate that the plasma deposition conditions play an important role in the oxide growth rate, reaction selectivity and phosphorus content, which directly affect the ionic conductivity of the PSG films. It was observed that increasing the deposition temperature led to a decrease in conductivity of the PSG films due to elevated phosphorus and silanol content. Increasing the plasma chamber pressure had a negative effect on the conductivity since the oxide reaction took place in gas phase in preference to the substrate at higher pressures, which lead to a decrease in the defect density of the prepared films. Finally, increases in RF power lead an increase in the conductivity. It was found that despite the decrease in phosphorus content of the PSG films, the number of silanol defect sites increased, leading to a substantial increase in the conductivity. It was also observed that the film growth rate was higher with 80 sccm flow rate of nitrous oxide indicating complete oxidation of silicon and phosphorus on the substrate.

Having elucidated the trends in the ionic conductivity as a function of various plasma conditions, a peak conductivity of 2.52×10^{-4} S/cm was achieved for PSG deposited at 400 W RF Power, 400 mTorr chamber pressure, 100 °C substrate temperature and a nitrous oxide flow rate of 80 sccm. This value is 2.5 times greater than the target conductivity value to 1×10^{-4} S/cm and 250 times greater than the ionic

conductivity of pure silicon dioxide films. Therefore, it is clear that doping of silicate glasses with phosphorus significantly improved the ionic conductivity of the oxide films.

The optimized PSG film was then used to make DMFCs with lower methanol permeability than pure Nafion electrolytes. Polarization experiments with both Nafion and PSG-Hybrid membrane passive DMFCs indicated that the presence of the P-doped silicate glass significantly improves cell performance. The open circuit voltage was increased by approximately 65 mV and the current density at 0.4 V was nearly tripled. The PSG-Hybrid electrolyte DMFC was also exposed to a constant load of 76 kΩ and showed excellent stability characteristics at room temperature and 12 M methanol fuel.

CHAPTER 5

CARBON DIOXIDE VENTS FOR DIRECT METHANOL FUEL CELLS

5.1 Objective

Passive, stand alone, direct methanol fuel cells require a pressure management system that releases product CO_2 from the anode chamber. However, this must be done without allowing the methanol fuel to escape.

The objective of this chapter is to study the performance of a polymer membrane for gas transport and CO_2/methanol separation. The design and operational parameters of a novel CO_2 venting technology in DMFC using polymer membranes have been described. The key parameter in the selective membrane is to maximize the transport of carbon dioxide with respect to methanol. The performance of two polymers: (i) poly (dimethyl siloxane) (PDMS) and (ii) poly (1-trimethyl silyl propyne) (PTMSP) have been investigated because of their hydrophobic nature, which supports the diffusivity of carbon dioxide over methanol. Compared to common polymeric materials (e.g. natural rubber and poly-ethylene), both PDMS and PTMSP are known to exhibit extremely high gas permeabilities.

Table 5.1 compares the permeability coefficients of oxygen and carbon dioxide through natural rubber and polyethylene with PDMS and PTMSP membranes. The permeability coefficient of CO_2 through PDMS is 100 times higher than polyethylene and 30 times higher than natural rubber. The corresponding permeability coefficients through PTMSP are 1,000 to 10,000 times higher than natural rubber or polyethylene. However,

the transport of methanol through these membranes as well as their performance in the presence of a non-ideal of methanol and CO_2 has not been previously explored.

. Furthermore, the role of two hydrophobic additives, 1, 6-divinylperfluorohexane and 1, 9-decadiene in improving the selectivity of the membranes has been discussed. This chapter also discusses the performance of vent membrane as a function of temperature. The theoretical and experimental efficiency of the vent has been discussed. The work presented in this chapter has been previously published in the Journal of Power Sources [36].

Table 5.1: Permeability coefficient for CO_2 and O_2 in Barrers

Polymer	**Permeability Coefficient at STP (Barrers)**	
	O_2	**CO_2**
Poly ethylene	2.2	9.5
Natural Rubber	24	131
Silicone Rubber (PDMS)	540-600	3230
PTMSP	7725	28000

5.2 Theory

The permeability coefficient of a permeate (gas or vapor) through a polymer matrix can be estimated using the Nernst Distribution function [59-61]. The permeability coefficient of species i, P_i, is defined as the product of its diffusion coefficient (D_i) and its solubility coefficient (S_i) and is given as Equation 5.1.

$$P_i = D_i \, . \, S_i \qquad (5.1)$$

Under steady state conditions, the solubility of a material is fixed and the rate of permeate transport can be looked at as the flux of permeate through the solid polymer matrix. Therefore, the permeability coefficient of species i through a polymer matrix can be expressed using Equation 5.2.

$$P_i = \frac{N_i l}{\Delta p A} \qquad (5.2)$$

where N_i is the steady state rate of mass transfer of species i through the polymer matrix, l is the thickness of the polymer membrane, A is the area, and Δp is the pressure gradient of species i between the upstream and the downstream side. Since the permeability coefficient is an intrinsic property of the material, it represents a useful tool in comparing the performance of different permeates through a material. For the study of a CO_2 vent in a passive DMFC, a useful figure of merit is the ratio of the permeability coefficient of CO_2 (P_{CO_2}) to methanol (P_{MeOH}), denoted in Equation 5.3 by α .

$$\alpha = \frac{P_{CO_2}}{P_{MeOH}} \qquad (5.3)$$

Values of α greater than 1 indicate that the membrane is intrinsically more selective to CO_2 than methanol. However, α is not the absolute difference in CO_2 and methanol mass

transport through the film because the composition or partial pressure of CO_2 and methanol are different in the fuel container and may change with time. This would lead to a different permeation rate, though permeability coefficient, being an intrinsic property of the membrane, remains the same. As such, the selectivity of the membrane, S, is defined as the ratio of the absolutes rates of mass transport of CO_2 and methanol through the polymer film.

$$S = \frac{N_{CO_2}}{N_{MeOH}} = \alpha \bullet \left(\frac{\Delta p_{CO_2}(t)}{\Delta p_{MeOH}(t)} \right) \tag{5.4}$$

Assuming ideal gas behavior, S can be expressed in terms of the partial pressure of CO_2 ($\wp_{CO_2}(t)$) and methanol ($\wp_{MeOH}(t)$) in the fuel tank headspace. The resulting expression for S is given by Equation 5.5.

$$S = \alpha \bullet \left(\frac{\wp_{CO_2}(t)}{\wp_{MeOH}(t)} \right) \tag{5.5}$$

Eq.5.5 can be further simplified by assuming that the partial pressure of methanol in the headspace of a stand alone DMFC is the same as the saturated vapor pressure, which is occurs when the two phases are in equilibrium. Eq. 5.5 can be rewritten in terms of the saturated vapor pressure of methanol and the absolute pressure of CO_2 in the headspace as shown in Equation 5.6:

$$S = \alpha \bullet \left(\frac{p_{CO_2}(t)}{p_{MeoH}^{sat}} \right) \tag{5.6}$$

While S represents a more useful diagnostic tool for the prepared films during operation, α is a more convenient comparative tool between candidate materials for the CO_2 vent. Also, if it is assumed that the vent releases CO_2 at the same rate as its electrochemical

generation in the anode tank, the theoretical flux of CO_2 can be written in terms of the current (i) as shown in Equation 5.7.

$$N_{CO_2,theoretical} = \frac{i}{nF} \tag{5.7}$$

Where n is the number of electrons transferred and F is the Faraday's constant. Furthermore, since the selectivity is directly related to the absolute rate of the permeate mass transport, we can define a theoretical fuel utilization efficiency, $\gamma_{theoretical}$, as the ratio of the electrochemical consumption of methanol to total methanol consumption (methanol consumed via electrochemical reaction and methanol lost though the polymer vent permeation), as shown in Equation 5.8.

$$\gamma_{theoretical} = \frac{i/nF}{i/nF + N_{MeOH}} \tag{5.8}$$

However the experimental efficiency of the vent can be calculated for the measured flux of CO_2 and methanol through the vent, as shown in Equation 5.9.

$$\gamma_{experimental} = \frac{N_{CO_2}}{N_{CO_2} + N_{MeOH}} = \frac{1}{\frac{N_{MeOH}}{N_{CO_2}} + 1} \tag{5.9}$$

Combining the definition of the selectivity, Equation 5.4, with Equation 5.9, yields a simple expression for the CO_2 vent efficiency, Equation 5.10.

$$\gamma = \frac{S}{S+1} \tag{5.10}$$

At steady state, the rate of electrochemical oxidation of methanol is equal to the rate of CO_2 permeation through the film. Therefore, the membrane aspect ratio (λ) is directly proportional to the operating current of a fuel cell and the rate of permeation of CO_2 through the membrane, as shown in Equation 5.11

$$\frac{i}{nF} = N_{CO_2} = P_{CO_2} p_{CO_2} \lambda \qquad (5.11)$$

Where p_{CO_2} is the absolute overpressure of CO_2 in the fuel container and λ is the aspect ratio of the film. Given that there are three variables in Equation 5.11, i, p_{CO_2} and λ, it is helpful to parametrically adjust one and plot the other two. Since the membrane efficiency is a function of selectivity, which is linearly related to the pressure, isobaric lines on an i-λ curve would establish constant efficiency (γ) trends. This relationship is shown in Equation 5.12

$$\lambda = \left(\frac{1}{nFP_{CO_2} p_{CO_2}} \right) i \qquad (5.12)$$

The mode of transport of a molecule through a glassy polymer matrix is a function of the intersegmental attraction between the permeating species and the polymer matrix. The permeation of gases is generally diffusion controlled, while the permeation of a condensable vapor is sorption controlled. Often the mechanism of permeation and its dependence on diffusion and sorption is explained through the solution-diffusion model, Equation 5.13 [32, 62].

$$E_P = E_D + \Delta H_S \qquad (5.13)$$

Where E_P is the activation energy of permeation, E_D is the activation energy for diffusion, and ΔH_s is the enthalpy of sorption. The E_P can be estimated using an Arrhenius relationship between P_i and temperature, T, as given in Equation 5.12 [62].

$$P_i = P_A \exp\left(\frac{-E_P}{RT} \right) \qquad (5.14)$$

Where P_A is the pre-exponential constant and R is the gas constant.

5.3 Results

The study of CO_2 and methanol permeation was carried out through two sets of experiments. In the first experimental setup, the permeation rates of methanol and CO_2 were measured independently. Methanol permeation studies were carried out by methanol gravimetric analysis. Figure 5.1 shows the weight loss of methanol as a function of time through the PDMS and the PTMSP membranes.

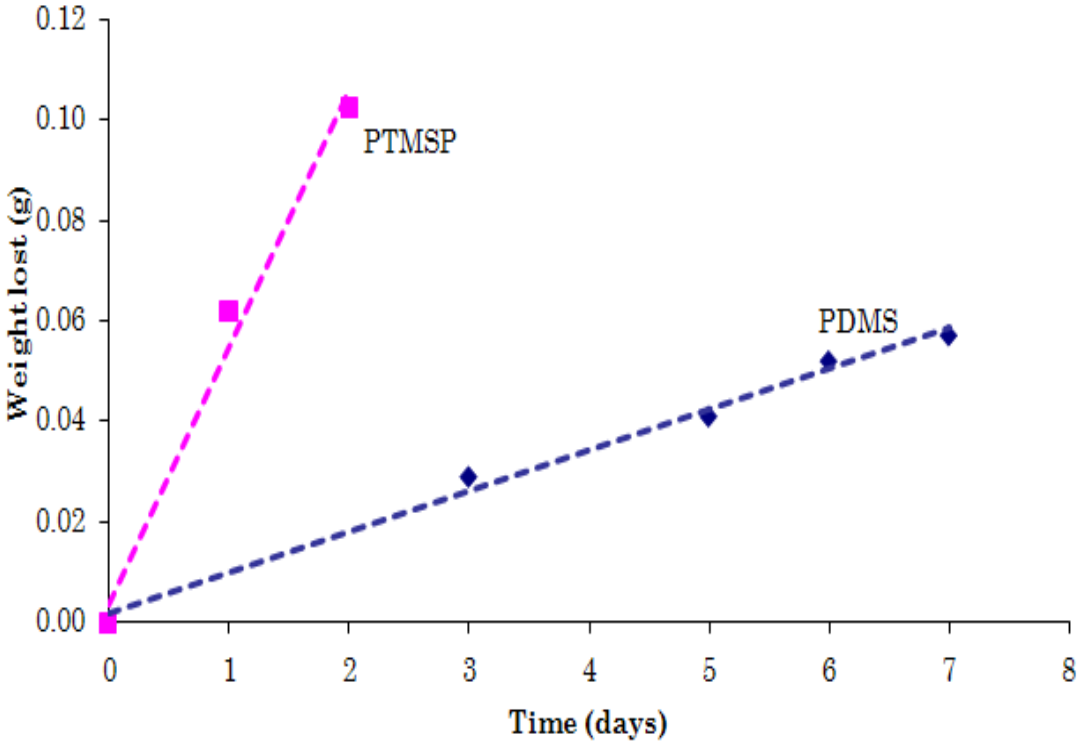

Figure 5.1: Methanol loss as a function of time through a PDMS and PTMSP membrane

The curves shown in the Figure 5.1 reflect a linear relationship between weight loss and time, as expected under steady state conditions for a fixed exposure area. The rate of methanol weight loss is 0.008 and 0.0512 g day^{-1} through the PDMS and the PTMSP membranes, respectively. Using Eq. 5.2, the corresponding permeability coefficient of methanol is 4.76 x 10^{-10} mol-cm cm^{-2}-day^{-1}-Pa^{-1} through PDMS and 5.1 x 10^{-10} mol-cm cm^{-2}-day^{-1}-Pa^{-1} through PTMSP membranes.

CO_2 permeation studies were carried out by measuring the pressure increase due to CO_2 transport through a thin polymer film. Figures 5.2a and 5.2b show the rate of pressure increase on the downstream side of the PDMS and the PTMSP membranes due to CO_2 permeation and accumulation in the sealed chamber. It is observed from Figures 5.2a and 5.2b that the pressure of CO_2 on the downstream side increases until it reaches a steady state value which is equal to the upstream pressure of CO_2 across the membrane. At this point, the CO_2 is in mechanical equilibrium across the membrane. The rate of pressure increase in the sealed chamber is calculated from the slope of the curve in Fig. 5.2 before it reaches steady state conditions. For the PDMS membrane, the CO_2 pressure increases at an initial rate of 9.21 x 10^{-4} psi min^{-1} and PTMSP at 0.631 psi min^{-1}. The resulting permeability coefficient (Eq. 4) of CO_2 was 9.5 x 10^{-10} and 1.25 x 10^{-9} mol-cm cm^{-2}-day^{-1}-Pa^{-1} for the PDMS and PTMSP membranes, respectively.

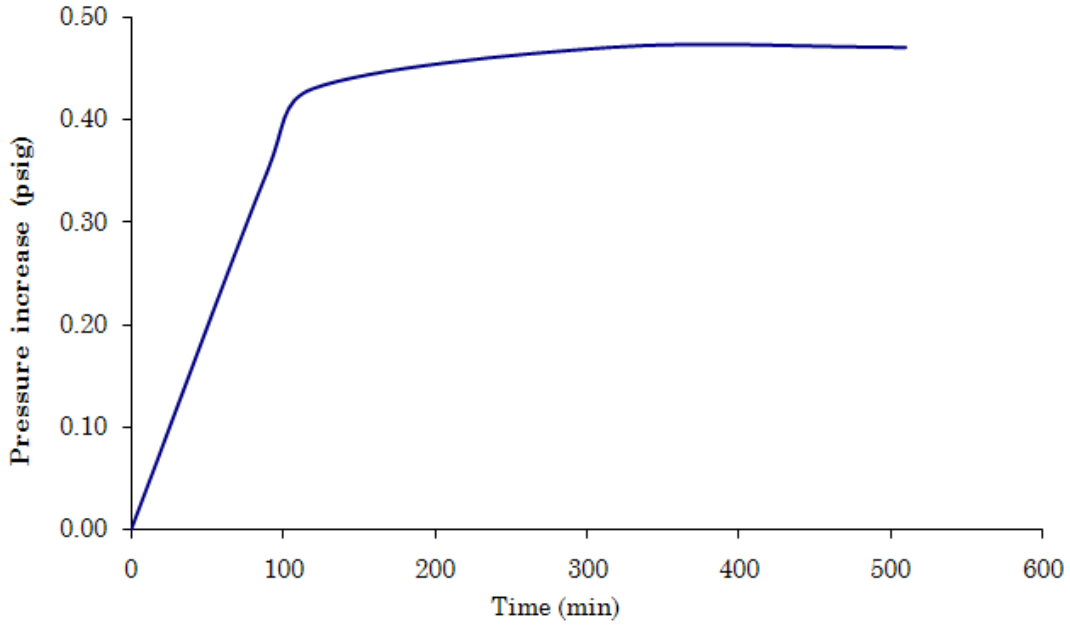

Figure 5.2a: Rate of pressure increase due to CO_2 permeation through PDMS membrane.

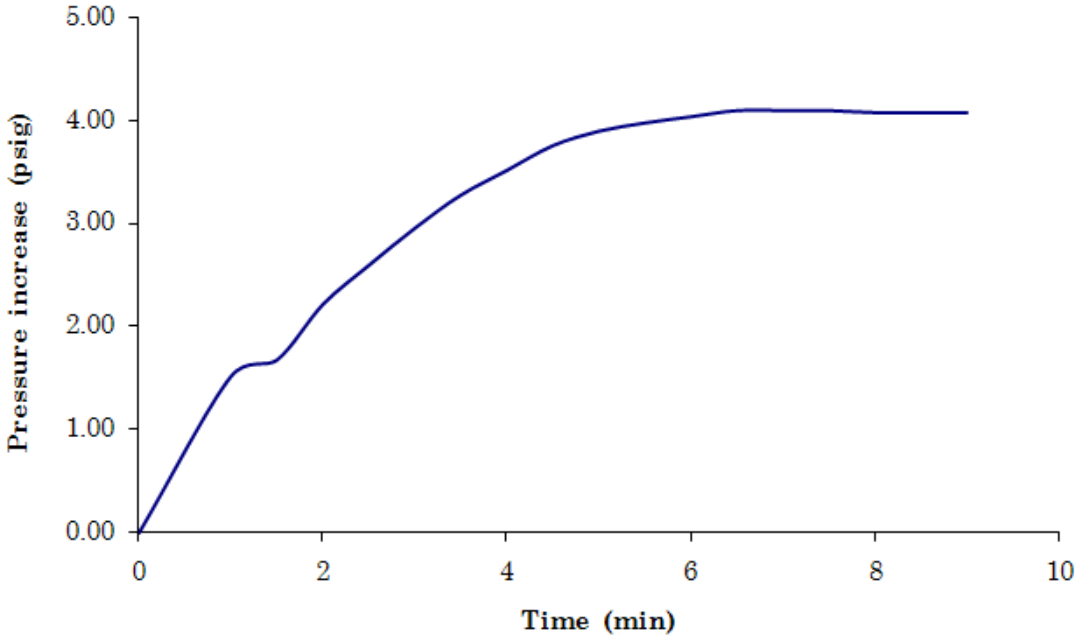

Figure 5.2b: Rate of pressure increase due to CO_2 permeation through PTMSP membrane

Based on the permeability coefficients of methanol and CO_2 through the PDMS and the PTMSP membranes, the magnitudes of α were estimated for each membrane using Equation 5.3. A value of 1.98 for α was obtained for the PDMS membrane and the corresponding value of α for the PTMSP membrane was 2.45.

The values of α obtained from the independent experiment setup were promising; however, α may vary under real operating conditions due to the non-ideal effects of having a methanol and CO_2 mixture. The relative amount of CO_2 and methanol detected as a function of time is shown in Figure 5.3. The instantaneous flux of CO_2 and methanol through the membrane was calculated using mass spectrometry sensitivity factors, which were obtained under known flow rate conditions in separate experiments. The equivalent steady state flux of CO_2 and methanol was 4.2×10^{-4} and 5.96×10^{-5} moles-day^{-1}-cm^{-2}, respectively. The resulting permeability coefficient of CO_2 and methanol through the PDMS membrane was 1.6×10^{-9} and 9.05×10^{-10} mol-cm cm^{-2}-day^{-1}-Pa^{-1} respectively.

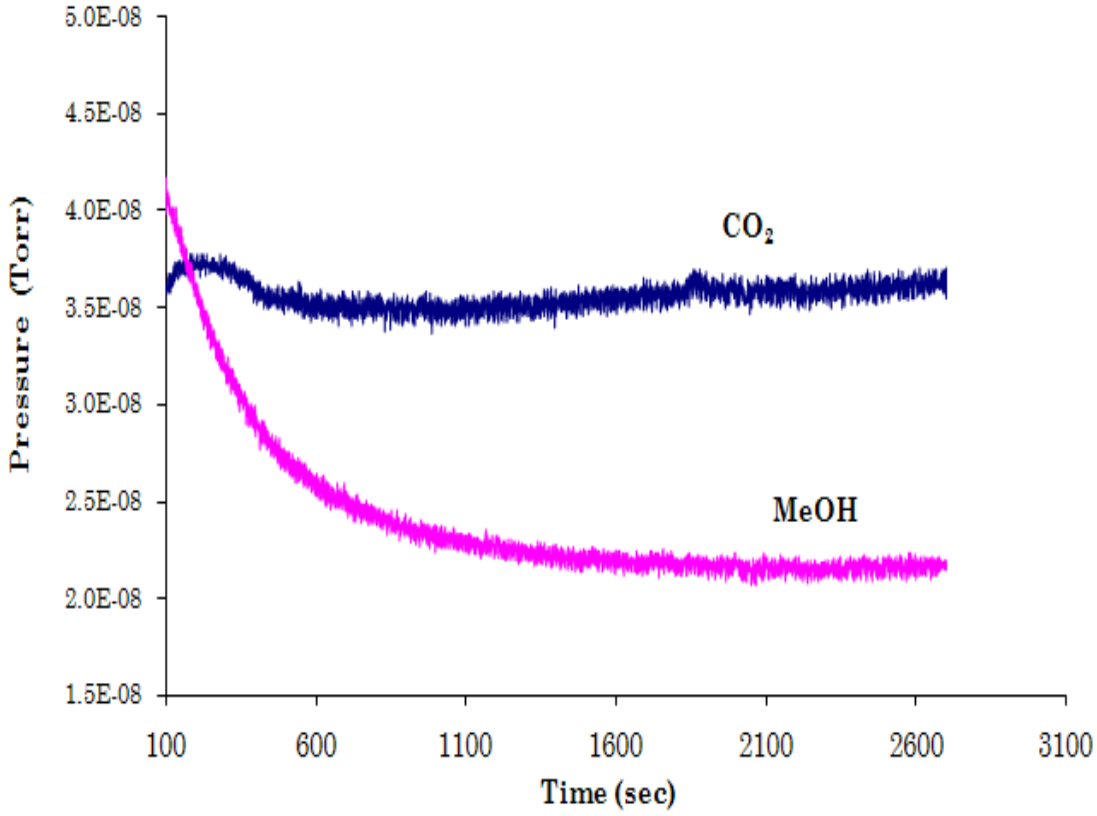

Figure 5.3: Pressure signal detected by RGA for CO_2 and methanol through PDMS membrane

A similar permeation experiment was conducted for a 120 µm PTMSP membrane, with an area of 2.85 cm^2. The relative amounts of methanol and CO_2 are shown in Figure 5.4 as a function of time. The steady state flux of CO_2 and methanol through PTMSP, calculated from Figure 5.4, are 4.91 x 10^{-4} and 1.12 x 10^{-4} moles-day^{-1}-cm^{-2}, respectively. The corresponding permeability coefficients of CO_2 and methanol through the PTMSP membrane are 1.7 x 10^{-9} and 8 x 10^{-10} mol-cm cm^{-2}-day^{-1}-Pa^{-1}, respectively.

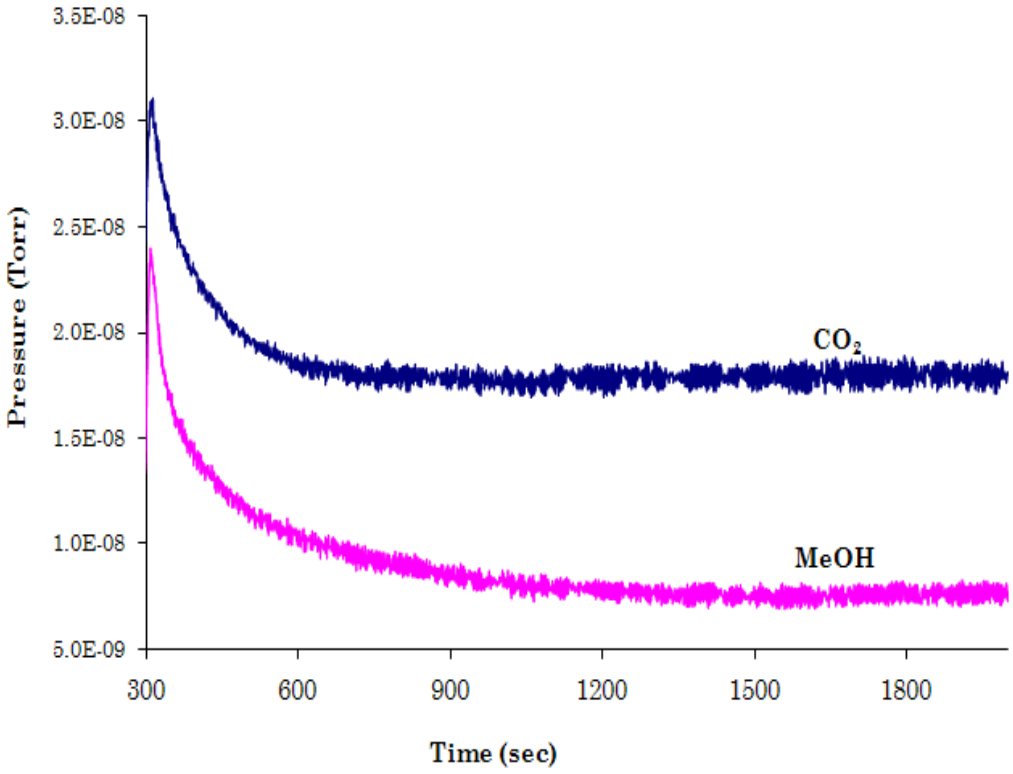

Figure 5.4: Pressure signal detected by RGA for CO_2 and methanol through PTMSP membrane

Table 5.2: Permeability coefficients (moles-cm/cm^2-day-Pa) and α value of methanol and CO_2 through PDMS and PTMSP membranes

	PDMS		**PTMSP**	
	Individual Setup	Binary Setup	Individual Setup	Binary Setup
CO_2	9.50E-10	1.60E-09	1.25E-09	1.70E-09
Methanol	4.80E-10	9.05E-10	5.10E-10	8.00E-10
α	1.98	1.77	2.45	2.13

The values for α were determined from the permeability coefficients of CO_2 and methanol through the PDMS and PTMSP membranes from their fluxes in separate permeation experiments and when mixed together. These values are shown in Table 5.2.

In all cases, the permeability coefficients for CO_2 through the PDMS and the PTMSP membranes were higher than the permeability coefficients of methanol through the same materials. Also, PDMS has higher permeability for methanol than PTMSP. The value of α was 1.98 through the PDMS and 2.45 through PTMSP as was obtained from the individual permeation experiments. The mass spectrometry results for the CO_2-methanol mixtures yielded permeability coefficients and α values in agreement with the separate-chemical experiments. The resulting α values were 1.8 for PDMS membranes and 2.13 for PTMSP membranes.

As discussed previously, α values greater than unity are good, since both PDMS and PTMSP membranes are intrinsically more selective to CO_2 than methanol. Most likely the hydrophobicity of the PDMS and the PTMSP membranes leads to an increased transport of CO_2, compared to methanol. To further increase the hydrophobicity of the PDMS and the PTMSP membranes, hydrophobic additives were incorporated into the polymer during membrane casting. To this end, two different additives, 1, 6-divinylperfluorohexane and 1, 9-decadiene, were used. Contact angle measurements were used to investigate the hydrophobic nature of the additives in the polymer matrix. Figure 5.4 shows the water contact angles for PDMS and PTMSP membranes as a function of the weight percent of 1, 6-divinylperfluorohexane in each polymer. As shown in Fig.5.4, the contact angle increased with increasing amount of 1, 6-divinylperfluorohexane in the polymer matrix showing the enhanced hydrophobic nature of the mixture.

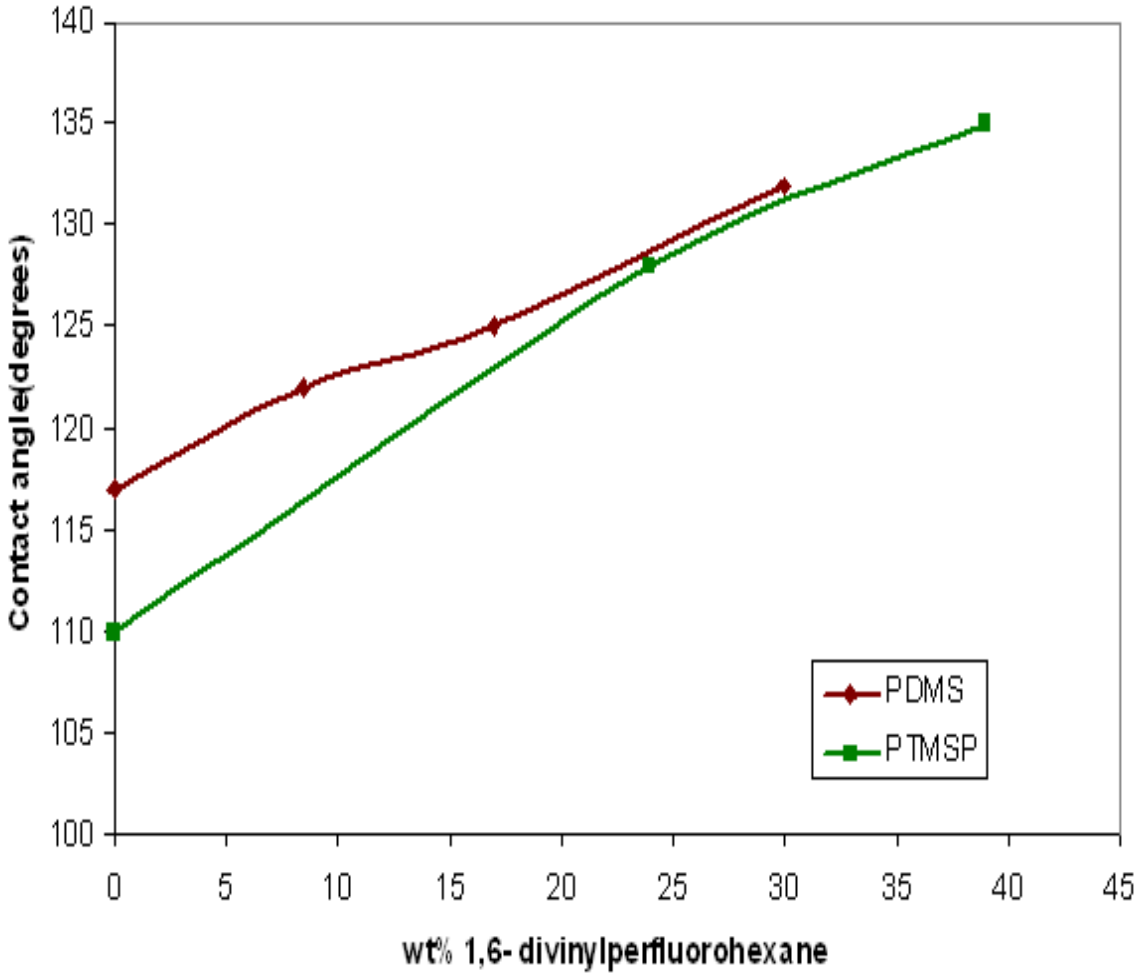

Figure 5.5: Water contact angle measurement for PDMS and PTMSP as a function of 1,6-divinylperflurohexane.

To quantify the effect hydrophobicity of the PDMS and PTMSP films on the separation performance with the two additives (1, 6-divinylperfluorohexane and 1,9-decadiene), permeability experiments were carried out for CO_2 and methanol, and their mixtures. Polymer membranes with an average thickness of 250 µm were cast for the mixtures of 1, 6-divinylperfluorohexane and PDMS. The flux of CO_2 and methanol were

measured at ambient temperature across an area of 2.85 cm^2. Using Equation 5.2, the molecular fluxes were translated into a permeability coefficient as a function of the additive content. The corresponding values of α were estimated from Equation 5.3. Figures 5.5a and 5.5b show the permeability coefficients and α for CO_2 and methanol as a function of 1,6-divinylperfluorohexane content in PDMS. The solid lines in Figures 5.5a and 5.5b correspond to the results for CO_2 and methanol, and the dotted lines are for CO_2 and methanol mixtures. Figure 5.5 shows that as the amount of 1, 6-divinylperfluorohexane increases in the PDMS matrix, the permeability coefficient of CO_2 increases while that for methanol decreases, as shown by the solid lines. The permeability of CO_2 and methanol, when measured separately, through a membrane composed of 35 wt% of 1, 6-divinylperfluorohexane in PDMS is $P_{CO_2} = 1.8 \times 10^{-9}$ moles-cm cm^{-2}-day^{-1}-Pa^{-1} and $P_{MeOH} = 5 \times 10^{-10}$ moles mol-cm cm^{-2}-day^{-1}-Pa^{-1}. This corresponds to a value of α of 3.6, which is about twice that of the pure PDMS membrane. However, the permeability coefficient and α trends when CO_2 and methanol were measured as mixtures did not comply with the independent measurement trend. It was observed that for CO_2 and methanol mixtures, the permeability coefficients of methanol increased at approximately the same rate as CO_2 for all compositions of PDMS and 1, 6-divinylperfluorohexane. As a result, the values of α for the polymer blend remained constant around 2.0.

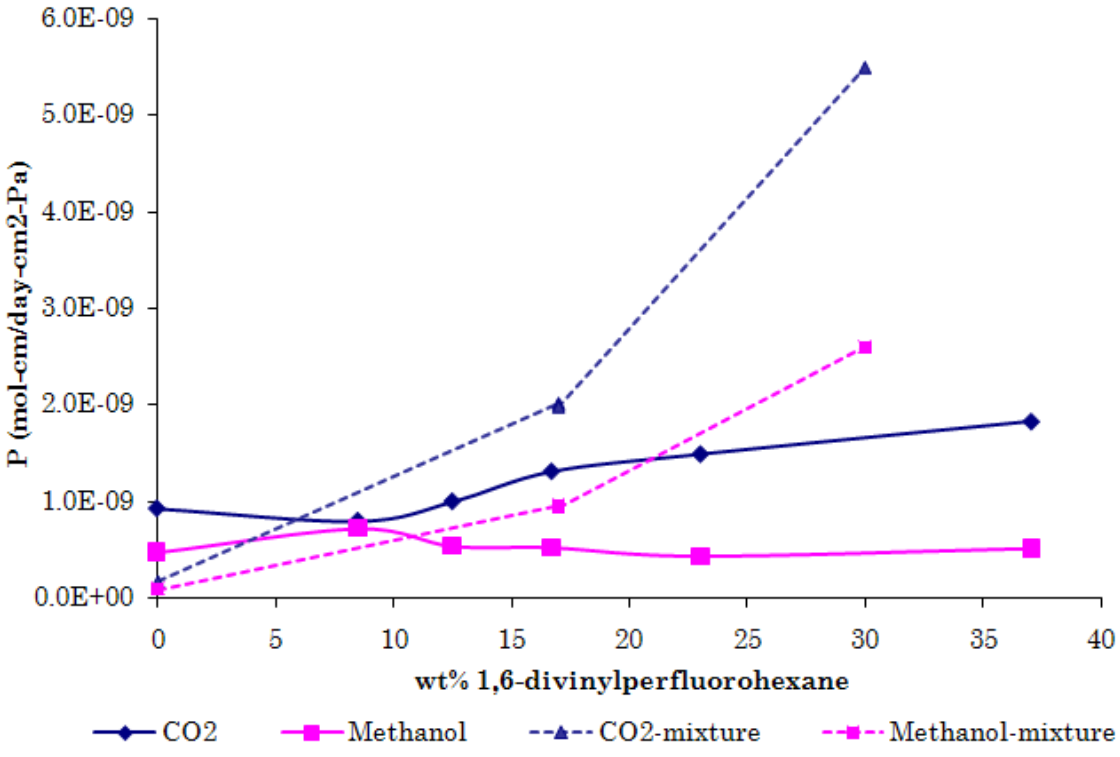

Figure 5.6a: Permeability coefficient through PDMS and 1,6-divinylperflrorohexane composite

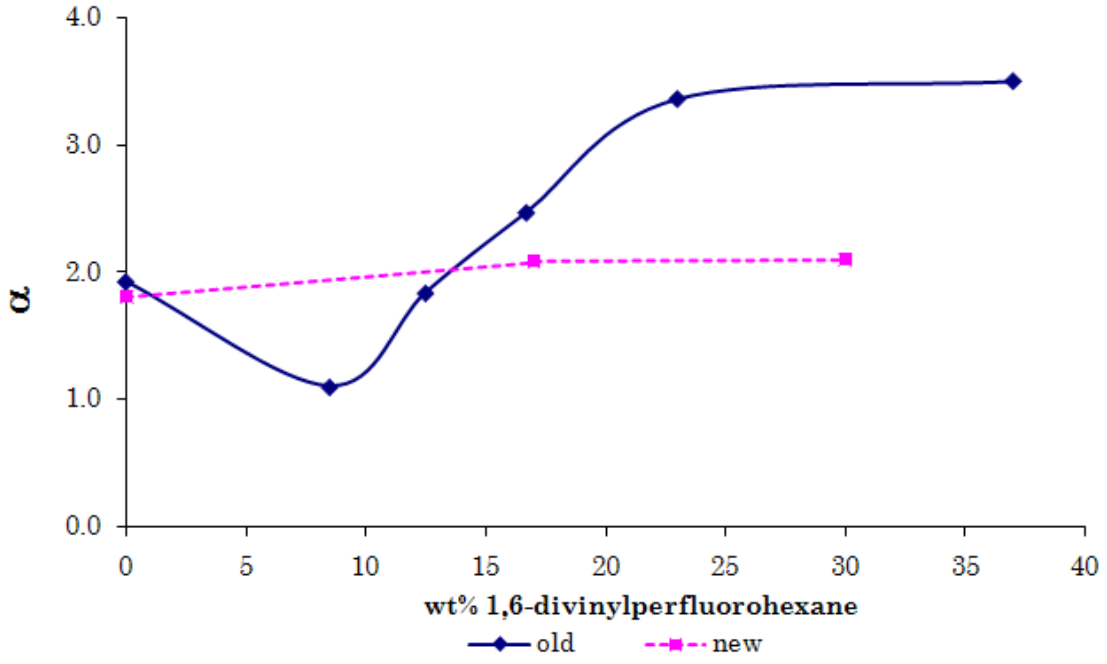

Figure 5.6b: Selectivity through PDMS and 1,6divinylperflrorohexane

Next, the performance of PTMSP and 1, 6-divinylperfluorohexane blends as membrane candidates for CO_2 vent were studied. Permeation rates of methanol and CO_2 were obtained by themselves and in CO_2 and methanol mixtures. In these experiments, the PTMSP blends had an average thickness of 11 μm and area of 2.85 cm^2. In each case, the fluxes of CO_2 and methanol were measured and translated into permeability coefficients and α values. Figures 5.6a and 5.6b shows the permeability coefficients and α of CO_2 and methanol through the polymer blend. The solid lines in these figures correspond to the results when the molecules were measured independently and the dotted lines correspond to the values obtained for mixtures of CO_2 and methanol. In both kinds of experiments, the permeability coefficient of CO_2 increased as the concentration of 1, 6-divinylperfluorohexane in the polymer increased, and the permeability coefficient for methanol decreased. The permeability coefficient and α trends when CO_2 and methanol were measured separately matched the values obtained for the mixtures. At 50 wt% of 1, 6-divinylperfluorohexane in PTMSP, the CO_2 permeability coefficient was 1.6 x 10^{-9} mol-cm cm^{-2}-day^{-1}-Pa^{-1} and methanol was 1.8 x 10^{-10} mol-cm cm^{-2}-day^{-1}-Pa^{-1}. As a result, α=9.2 was almost 5 times higher than the neat PTMSP membrane.

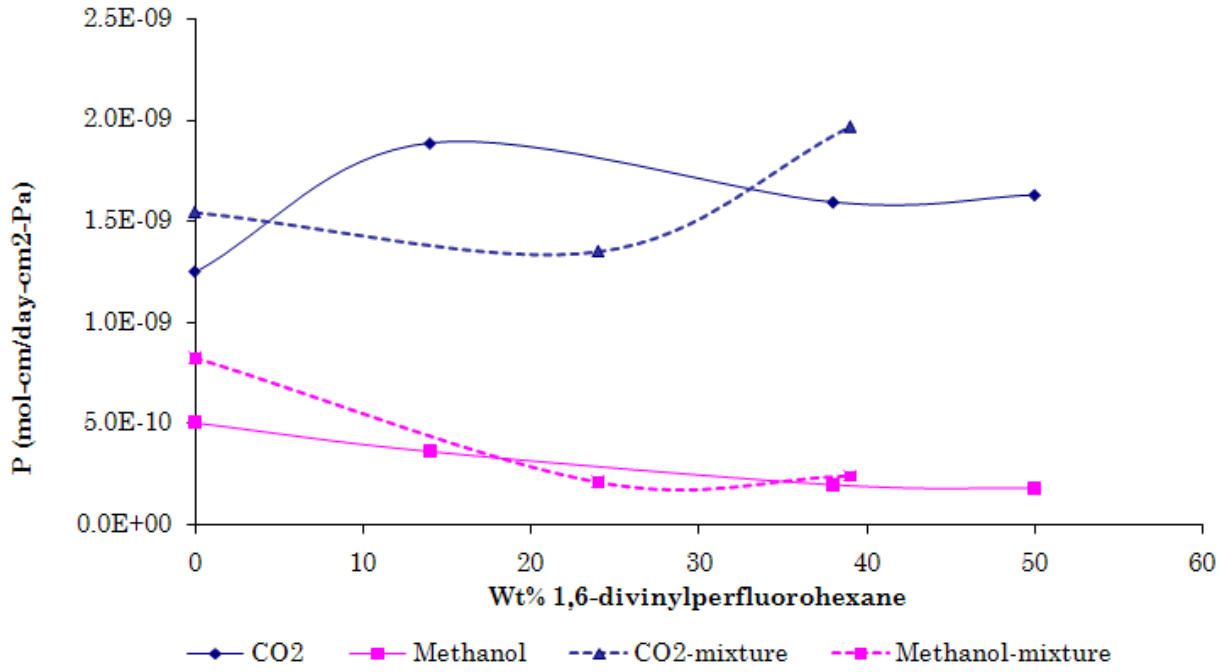

Figure 5.7a: Permeability coefficient through PTMSP and 1,6-divinylperflrorohexane composite

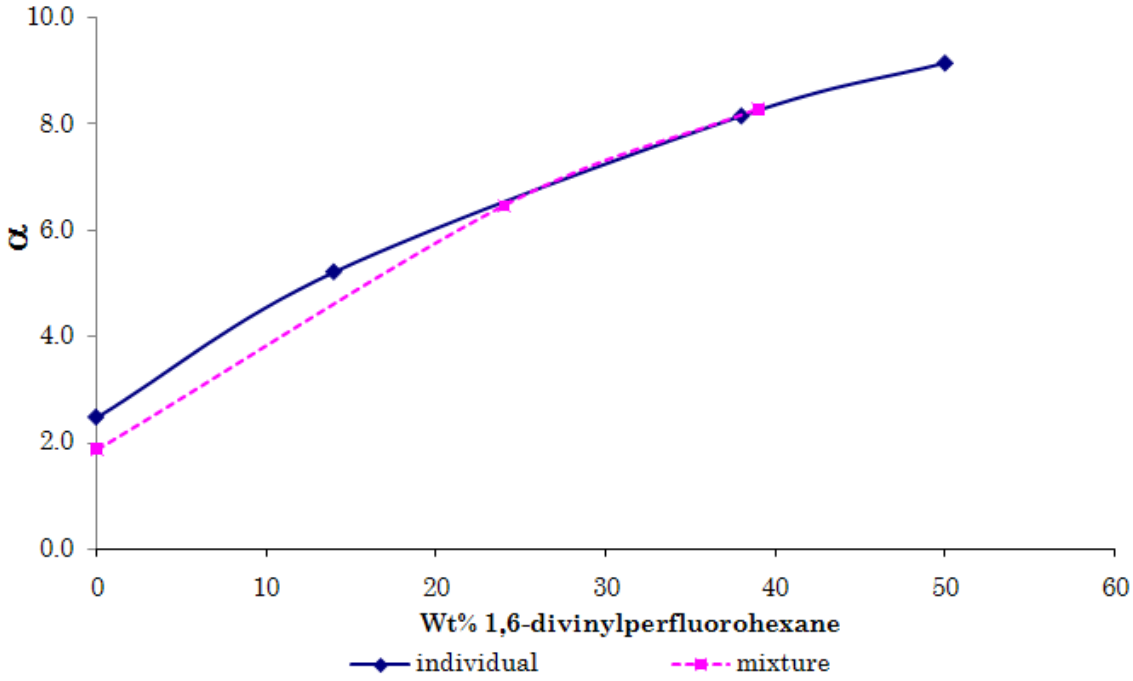

Figure 5.7b: Magnitude of α through PTMSP and 1,6-divinylperflrorohexane composite

Since PTMSP blends showed higher permeability coefficients than PDMS and its mixtures, the addition of a second additive, 1, 9-decadiene in PTMSP matrix was investigated. Like previous experiments, the rate of transport of methanol and CO_2 was measured by the independent and the binary system setups. In this case, membranes with average thickness of 120 μm were cast and the flux of CO_2 and methanol were measured at STP across an area of 2.85 cm^2. Figures 5.7a and 5.7b show both the permeability coefficients and α for CO_2 and methanol as a function of 1, 9-decadiene content in the PTMSP blend. The solid lines in Figure 5.7 are for CO_2 and methanol measured separately and the dotted lines are for CO_2 and methanol in a mixture. The 1, 9-decadiene/PTMSP membranes shows somewhat different permeabilities for the neat chemicals and their mixtures. For the separate permeability measurements of CO_2 and methanol, the permeability coefficient of carbon dioxide slightly increases with increasing 1, 9-decadiene content while the permeability coefficient of methanol through the film appears to be significantly hindered. Thus, α steadily increases with increased 1, 9-decadiene in the polymer film. The largest α obtained with this blend, 9.0, occurred with a 50:50 wt % mixture. However, the behavior observed for the vapor phase mixture of CO_2 and methanol was entirely different. In this case, the carbon dioxide permeation rate increased drastically with the addition of 1, 9-decadiene and the methanol permeation rate was nearly unchanged. Therefore, the obtained α was significantly reduced and the maximum value measured was 3.0 with 30 wt % 1, 9-decadiene.

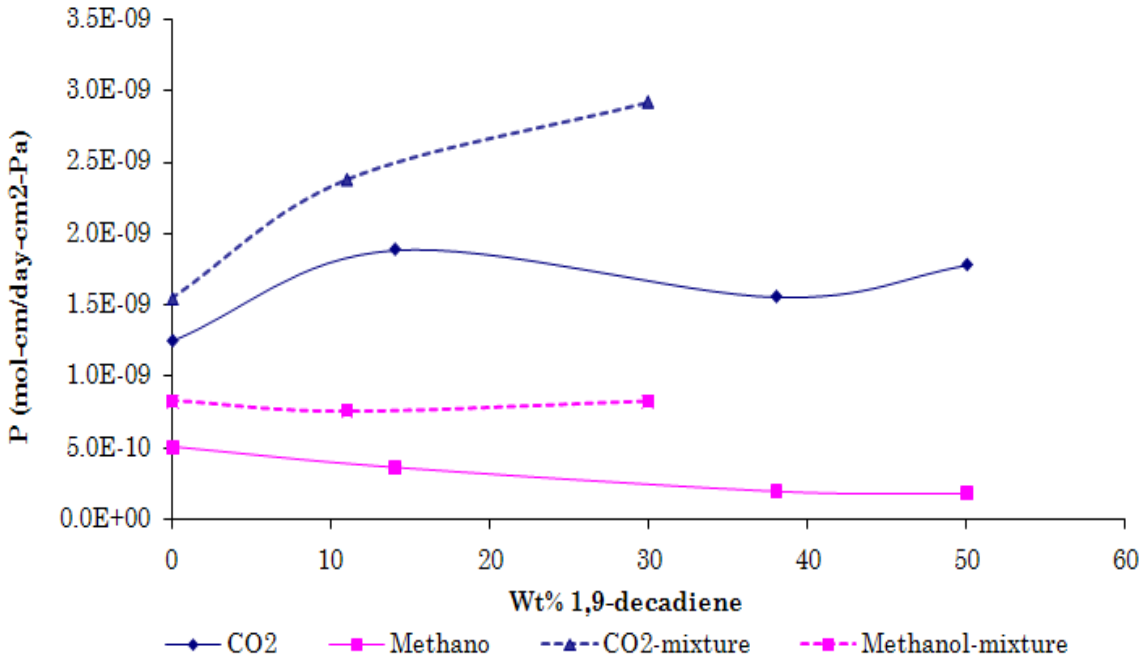

Figure 5.8a: Permeability coefficient through PTMSP and 1,9 decadiene composite

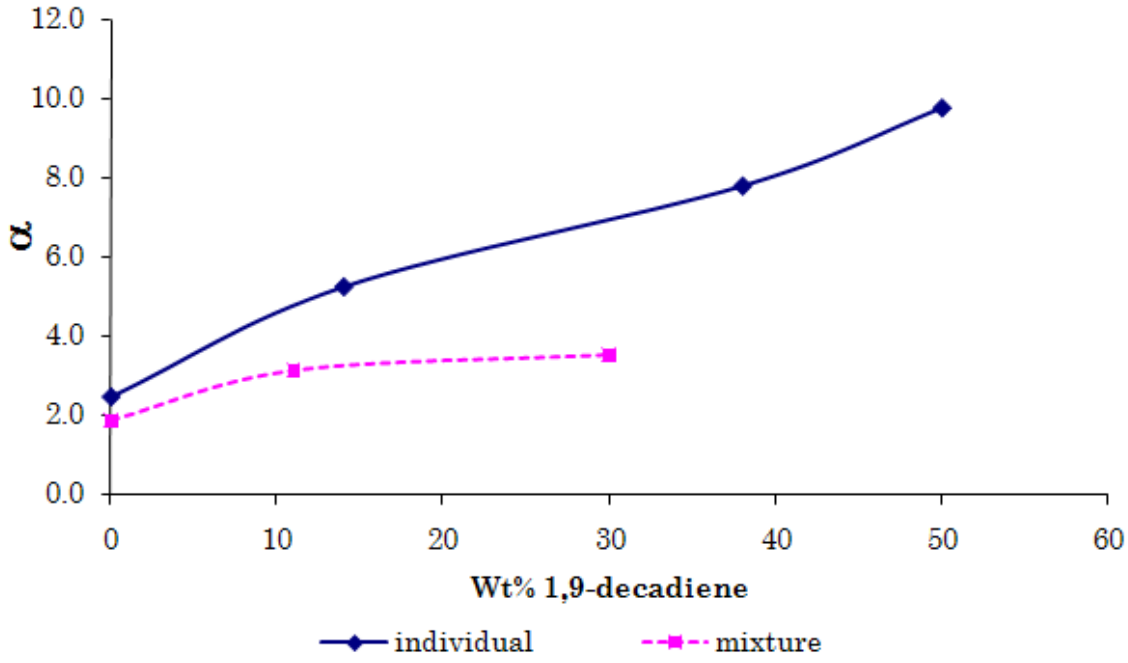

Figure 5.8b: Magnitude of α through PTMSP and 1,9 decadiene composite

In the above sections, the permeation behavior of CO_2 and methanol through different hydrophobic blends of PDMS and PTMSP membranes was studied. The best performing CO_2 vent was a polymer matrix with a 1:1 wt% of PTMSP and 1, 6-divinylperfluorohexane with α value of 9.2. It was also observed that the performance of this membrane remained constant when both methanol and CO_2 were present as a non-ideal mixture which yielded the top performance under fuel cell operating conditions. Based on these values, a theoretical model to predict the size of a CO_2 vent for a passive, stand alone DMFC was developed and is shown in Equation 5.8 and 5.11. The only parameter to be considered for the selective CO_2 vent is its aspect ratio (area-to-thickness ratio). Thus, three independent variables: pressure, current, and membrane aspect ratio (λ) fully define the fuel cell operating parameters and vent efficiency (fractional loss of methanol through the vent with respect to transport of all carbon dioxide and methanol through the vent).

Figure 5.9 shows the design conditions for a passive DMFC relating the operating current with CO_2 vent aspect ratio at a desired efficiency, as predicted by the theoretical models in Equation 5.11 and 5.12.. This design specification plot was generated using the experimental results for 1:1 mixture of PTMSP and 1, 6-divinylpefluorohexane where α was equal to 9. Figure 5.10 shows the effect of changes in operating current (i) on γ, keeping a constant aspect ratio (λ). The effect of current on the aspect ratio was estimated from Equation 5.12. It is observed that the change in the operating current has a negligible effect on the aspect ratio of a CO_2 vent.

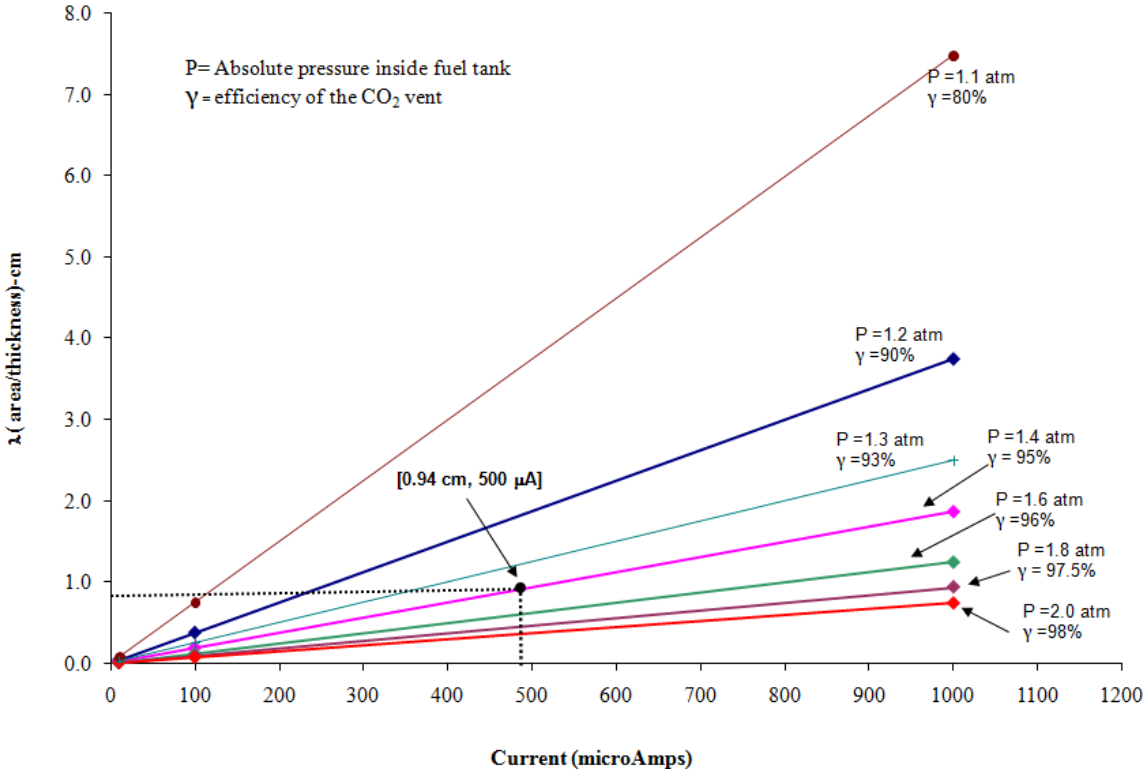

Figure 5.9: Design Specification of CO_2 vent and their efficiency (γ)

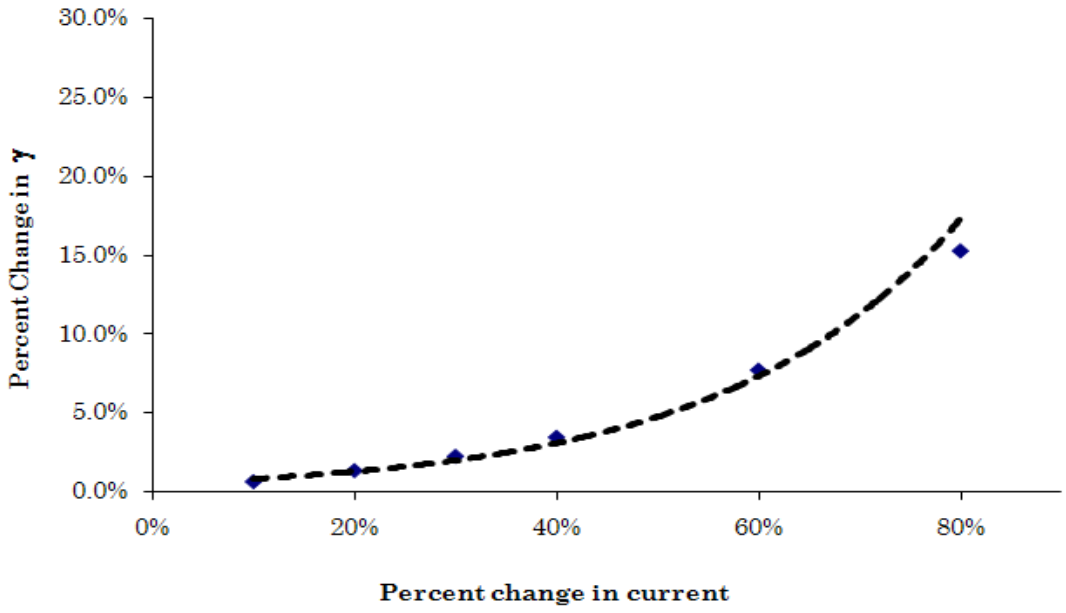

Figure 5.10: Sensitivity of γ to changes in operating current

The performance of PTMSP and 1, 6-divinylperfluorohexane showed promising results and demonstrated high selectivity for CO_2 release. The next part of the result evaluates the performance of the CO_2 vent under different DMFC operating conditions. For this part of the experiment, membrane samples were prepared by mixing PTMSP with 1, 6-divinylperflurohexane at a 1:0.1 weight ratio.

In a real fuel cell operation, CO_2 vent installed on a DMFC can undergo the same thermal cycle as the DMFC itself. Thus, it is necessary to investigate thermal stability and temperature dependent performance of the CO_2 vent to validate its application. Thermogravimetric analysis was used to test the thermal stability of the vent material. Figure 5.11 shows the thermogravemetric degradation profile of a PTMSP and 1, 6-divinylperfluorohexane blend. The polymer film shows no sign of weight loss or thermal degradation from 20°C to 90°C. The weight loss starts at about 90°C to 100°C and continues at the rate of 0.03% per degree to about 210°C. Between 210°C and 350°C, the polymer film shows a negligible weight loss. Beyond 350°C, the polymer film's weight drops sharply, indicating bulk polymer degradation.

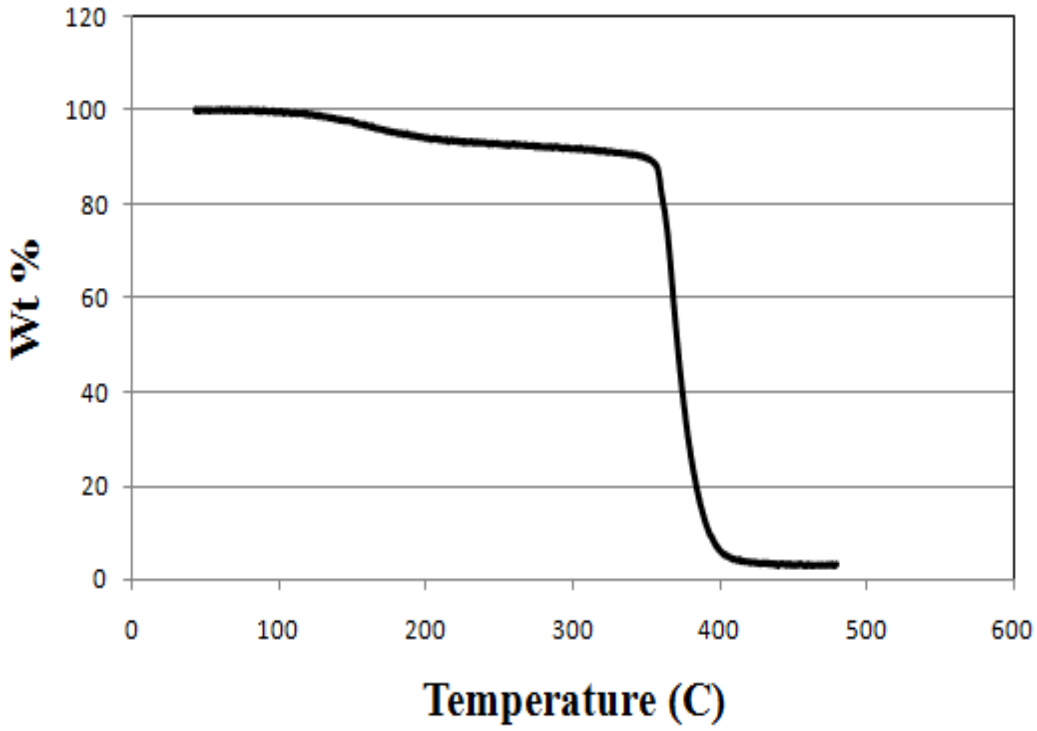

Figure 5.11: TGA of PTMSP with 1,6-divinylperflurohexane at 1:1 weight ratio.

Figure 5.12 shows the permeability coefficient of CO_2 and methanol as a function of temperature from 20°C to 50°C for the individual-component and mixture experimental setups. The flux of methanol and CO_2 through a PTMSP and 1,6-divinylperfluorohexane blend were measured at 22, 30, 40, 45, and 50°C. The permeability coefficients were not measured at temperatures above 50°C to avoid methanol boiling. Using Equation 5.2, the measured fluxes were translated into the corresponding permeability coefficients. For consistent results, the same membrane (2.85 cm^2 area and 150 µm thick) was used in both experimental setups. The permeability

coefficient of methanol decreased with increase in temperature, and the permeability coefficient of CO_2 increased. This trend was observed in both individual-component and mixture setups. At ambient temperature, the permeability coefficient of CO_2 was 9 x 10^{-10} and 1.2 x 10^{-9} mol-cm-cm^{-2}-day^{-1}-Pa^{-1} for the individual and the mixture setup, respectively. The CO_2 permeability coefficient at 50°C was estimated to be 1.21 x 10^{-9} moles-cm cm^{-1}-day^{-1}-Pa^{-1} for individual-component experiment. In the presence of methanol, the CO_2 permeability was essentially the same; 1.35 x 10^{-9} mole-cm-cm^{-2}-day^{-1}-Pa^{-1}.

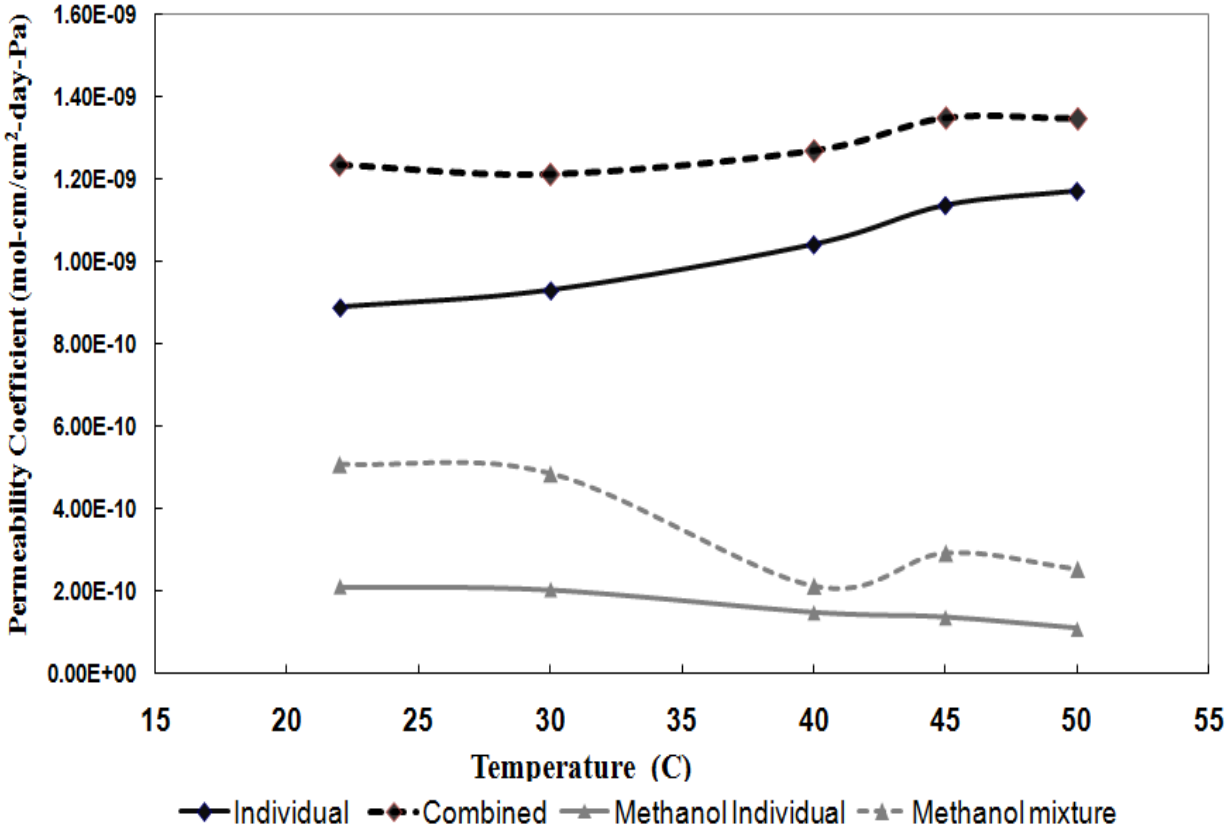

Figure 5.12: Permeability coefficients of CO_2 and methanol through PTMSP and 1,6-divinylperflurohexane.

Figure 5.13 shows the value of α for both the individual-component and mixture experiments. The value of α was determined from the permeability coefficients of CO_2 and methanol using Equation 5.3. The values of α increased as the temperature increased from 20°C to 50°C. While it increased from 4.2 to 10.6 for the individual-component experiment, the increase for the mixture experiment was comparatively lower (2.8 to 5.3).

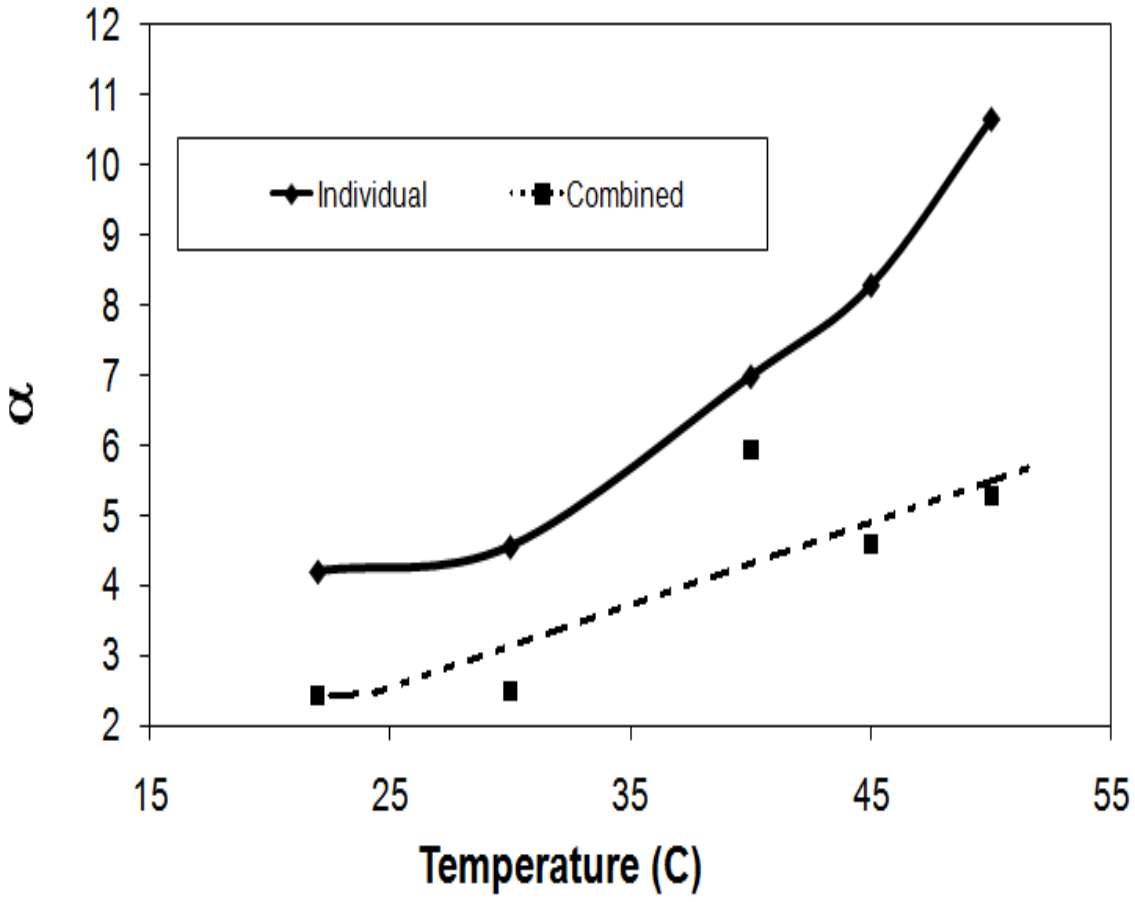

Figure 5.13: Values of α as measured through PTMSP and 1, 6- divinylperfluorohexane membrane

Figures 5.14 and 5.15 show the Arrhenius relationship for CO_2 and methanol permeability coefficient. The activation energy of permeation (E_P) through PTMSP and 1, 6-divinlyperfluorohexane was estimated from the slope of the curve in Figures 5.14 and 5.15, using Equation 5.14. The E_P of pure CO_2 through the vent membrane was 3.603 kJ $mole^{-1}$. However, in the presence of methanol, E_P for CO_2 was comparatively lower at 1.296 kJ $mole^{-1}$. While the E_P for pure methanol was -9.03 kJ/mole, the E_P for methanol in mixture was -8.08 kJ/mole.

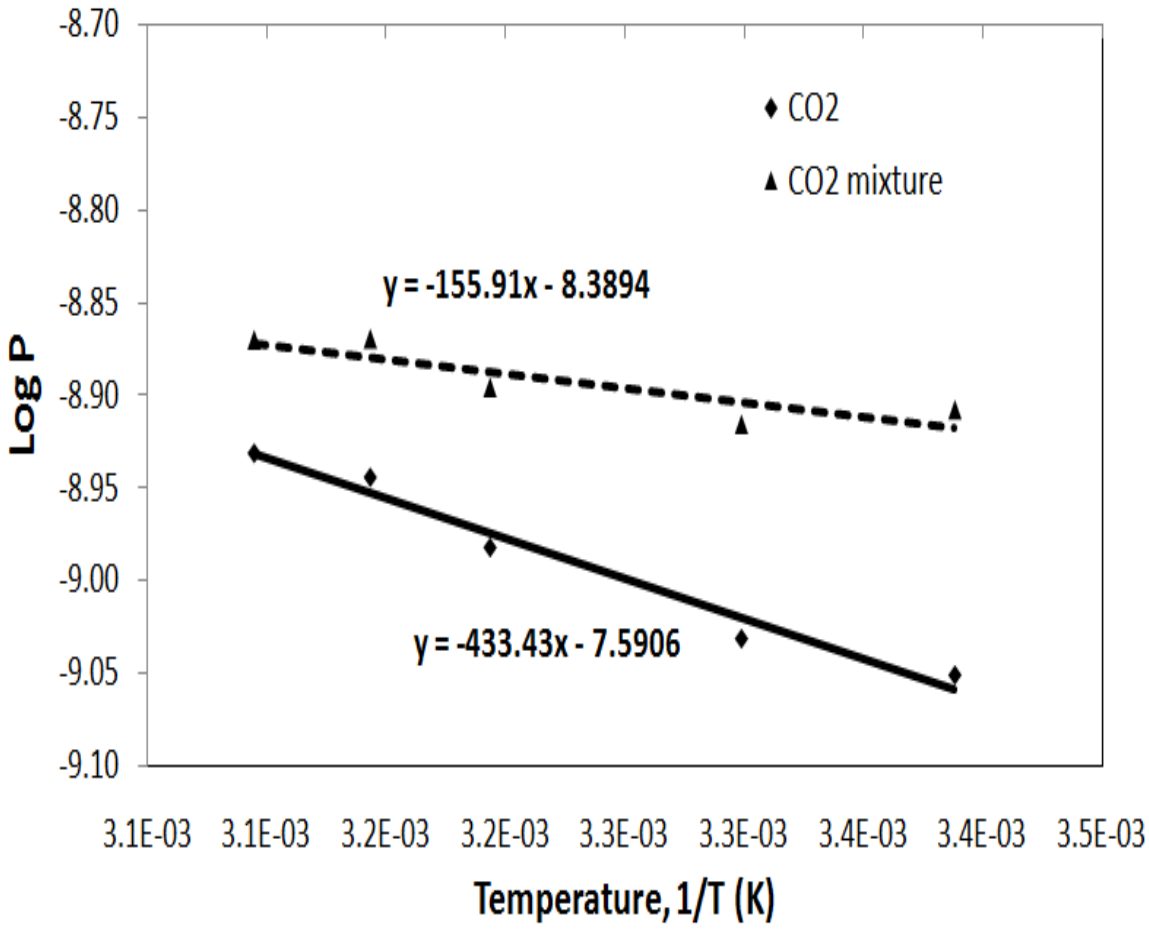

Figure 5.14: Arrhenius plot of CO_2 permeability coefficient through PTMSP and 1,6-divinylperfluorohexane

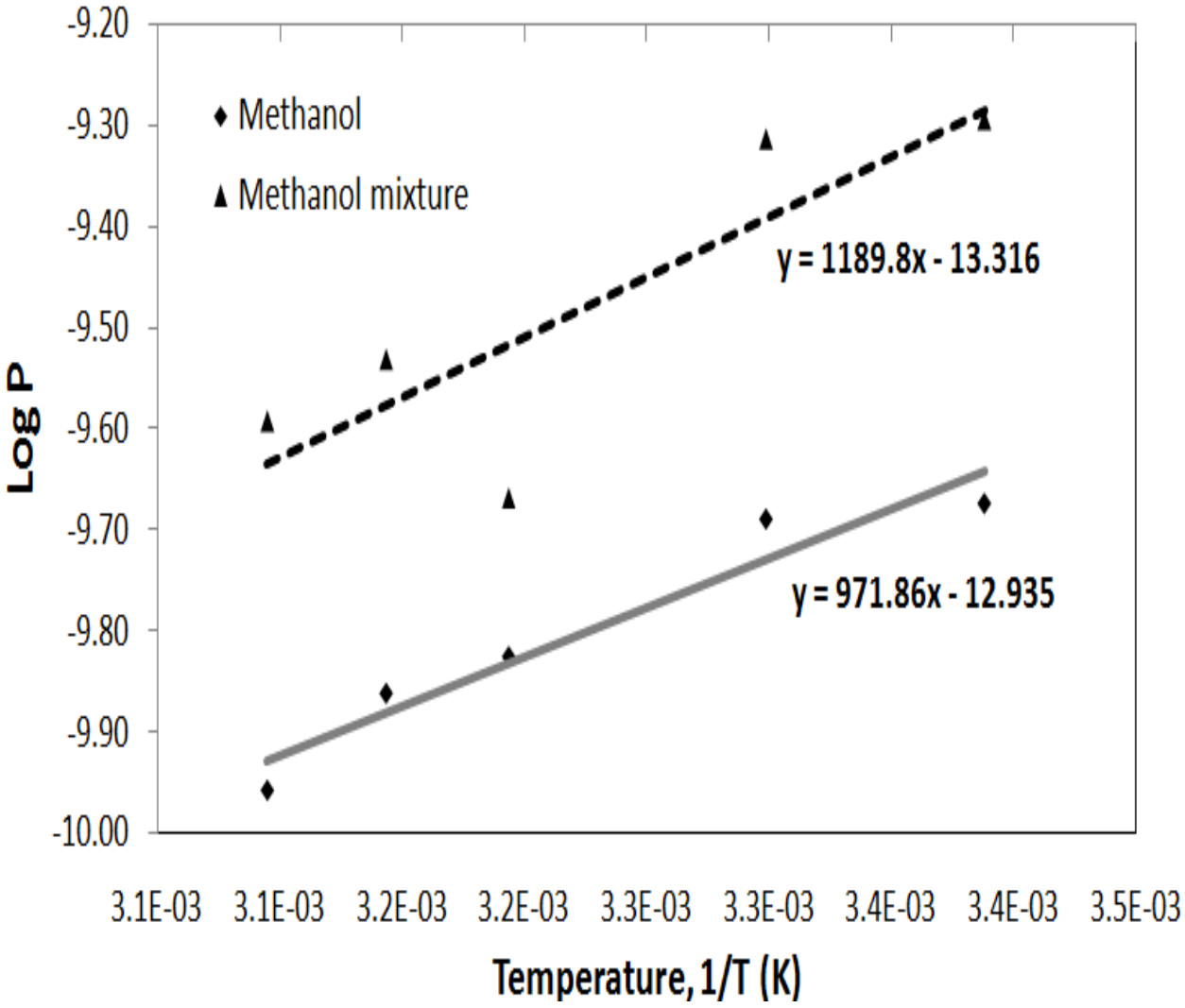

Figure 5.15: Arrhenius plot of methanol permeability coefficient through PTMSP and 1,6-divinylperfluorohexane

Figure 5.16 shows the theoretical and experimental efficiency of the CO_2 vent as a function of the operating current. At each operating current, the theoretical and experimental efficiencies were estimated from Eq.8 and 9 in conjunction with the

calculated and the measured fluxes. The permeability coefficients used for theoretical flux estimation are 7.56 x 10^{-9} and 2.16 x 10^{-9} mol-cm-cm^{-2}-day^{-1}-Pa^{-1}, for CO_2 and methanol, respectively. The steady state flux of CO_2 and methanol was measured using the response from the quadruple mass spectrometer at each operating current, which corresponded to a unique CO_2 flow rate. The theoretical and experimental efficiencies are very close to each other. The overall efficiency for a 10-to-1 PTMSP-to-1,6-divinylperfluorohexane membrane is approximately 80%.

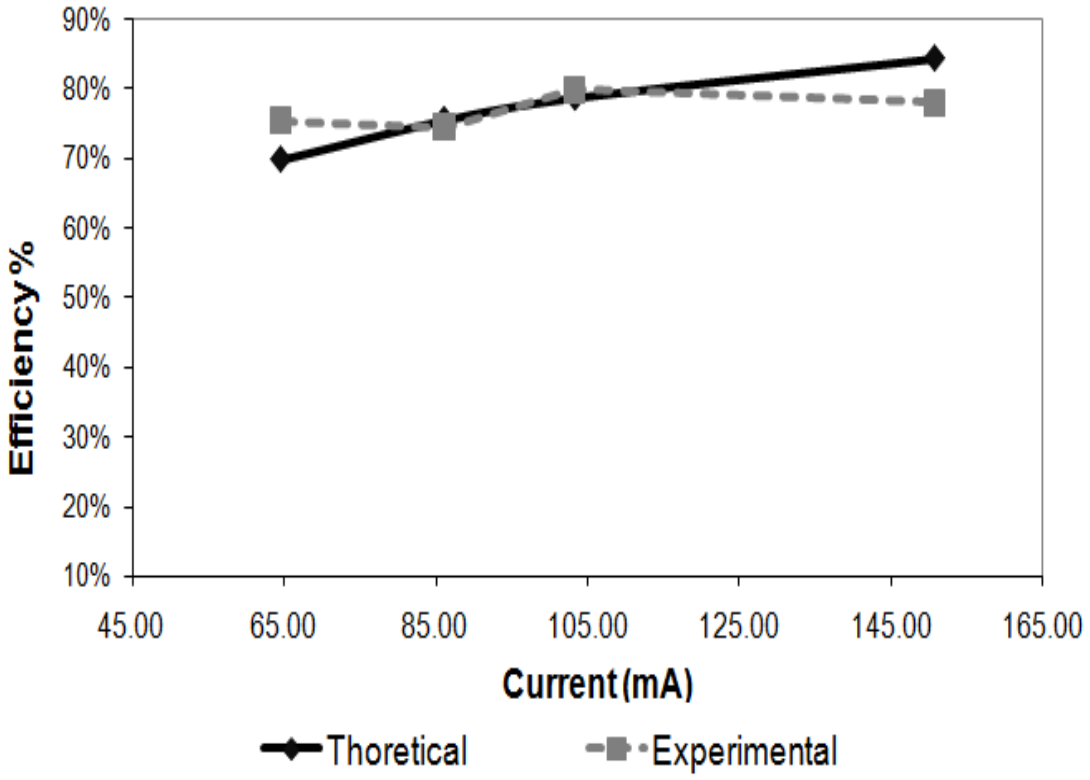

Figure 5.16: Theoretical and Experimental Efficiency of CO_2 vent membrane as a function of operating current

When a DMFC is operating in an upright condition, the CO_2 vent is in contact with methanol vapor and CO_2 gas. However, if the orientation is changed (or the tank is full), it is likely that the vent will be in direct contact with liquid methanol (wet condition). A permeation experiment, with the vent window below the liquid level, was designed to evaluate the performance of the CO_2 vent in contact with liquid methanol. The total driving force for liquid methanol transport is due to the saturated vapor pressure of methanol and the pressure due to the liquid column of methanol. The driving force for CO_2 transport in wet condition is a function of Henry's Law for CO_2 solubility in methanol and its partial pressure in gas phase. Table 1 shows the permeability coefficient of methanol and CO_2 under wet (liquid methanol) and dry (methanol vapor) conditions. The permeability coefficient of CO_2 under liquid methanol conditions is lower than that under methanol vapor conditions. The permeability coefficient of methanol in liquid and vapor conditions is approximately the same (1.9×10^{-9} vs. 2.1×10^{-9} mol cm $cm^{-1}day^{-1}Pa^{-1}$). As a result, the value of α is higher in vapor conditions than in liquid conditions.

Table 5.3: Permeability Coefficients of CO_2 and methanol (mol-cm-cm^2-day^{-1}-Pa) in wet and dry conditions.

	CO_2	**Methanol**	**α**
Dry Conditions	7.56×10^{-9}	2.1×10^{-9}	3.6
Wet Conditions	2.8×10^{-9}	1.9×10^{-9}	1.5

5.4 Discussion

The performance of PDMS and PTMSP polymer membranes as a selective CO_2 vent material has been demonstrated in this study. The permeability coefficients of CO_2 and methanol as pure species and as a non-ideal mixture through the polymer membranes were estimated. The results obtained from the permeability experiments of pristine PDMS and PTMSP membranes (Figs. 5.1, 5.2, 5.3 and 5.4) have been summarized in Table 5.2. It was observed that the overall permeability coefficient of CO_2 was higher than methanol for both the PDMS and the PTMSP membranes. The results shown in Table 5.2 shows that both membranes are hydrophobic in nature and allow the transport of CO_2 molecules with less hindrance than the polar, hydrophilic methanol molecules. It was also observed that the PTMSP membranes showed higher values for α in comparison to the PDMS membranes.

The higher value of α obtained for PTMSP membranes emphasizes the differences in the polymer structure of the PDMS and PTMSP membranes and their relative hydrophobicity. The higher permeability coefficients of CO_2 observed for the PTMSP membranes are because of the four methyl groups attached to each repeat unit in the PTMSP monomer in comparison to the two methyl groups in the PDMS monomer as shown earlier in Figure 5.2a and 5.2b. As a result, hydrophilic methanol molecules experience added hindrance in their transport through the PTMSP membranes than through the PDMS membranes thereby generating higher values for α.

The higher permeability coefficients obtained through PTMSP may also be due to its higher free volume. Unlike PDMS matrix, PTMSP has alternating double bonds and a tertiary silicon moiety that causes unsymmetrical monomer packing in the matrix.

Consequently, the PTMSP matrix has a lower polymer density (or high free volume density) than the PDMS matrix (0.75 g cm^{-3} vs.1.227 g cm^{-3}). Another feature that distinguishes the permeation properties and void density of the PTMSP membranes from the PDMS membranes is its glassy nature. PTMSP is considered as a glassy polymer because of its high glass transition temperature (> 200 °C).

Conventionally, the highly rigid structure associated with glassy polymers should restrict the transport of permeates through it. However, unlike traditional glassy polymers, PTMSP exhibits extremely large gas permeabilities that are in some cases several orders of magnitude higher than otherwise expected. This behavior can be explained on the basis of the dual mode sorption theory [63]. According to this theory, glassy polymers consist of mixed matrix structure where "dense" regions of intertwined, tangled polymer chains exist with micro-voids scattered amongst them. Because of the low enthalpy of sorption associated with PTMSP and weak sorption properties, it is believed that the density of micro-voids in the PTMSP is very high [30]. Unlike rubbery polymers, where the transport mechanism of permeate is mostly a result of the diffusion and sorption, glassy polymers act as sieving media and allow for a size-selective transport mechanism. In this mechanism the transport of a species through the membrane is strongly influenced by the size of the penetrants and the number of micro-voids available in the transport pathway. Since the transport mechanism is a size-related fundamental property, it is evident that the PTMSP backbone with a continuum of micro-voids will show a higher permeability coefficient for CO_2 than the PDMS membrane while their hydrophobic end groups will ensure low permeability coefficients for methanol.

In the independent permeation experiments, Figures 5.6a and 5.6b, the permeability coefficients of CO_2 increases while that of methanol decreases as a function of the 1, 6-divinylperfluorohexane content in the PDMS membrane. This is likely due to the fact that the PDMS polymer blends are more hydrophobic than the pristine PDMS due to the addition of 1,6-divinylperfluorohexane. As a result, higher permeability coefficients of CO_2 and lower permeability coefficients of methanol are expected.

Previous studies by Sohn et. al have shown that in a polymer matrix with relatively high cross linking density, permeability is dictated by the diffusion of species thorough the polymer [64]. Because of the "mutually alike" nature of fluorinated PDMS matrix and CO_2, its permeability coefficient increases. The polar methanol molecules (electron withdrawing/proton donating) have a tendency to form hydrogen bonds with their neighboring atoms. Thus, they aggregate together forming clusters of methanol. This observation has also been studied in the work done by Favre et al., who supported the cluster formation of methanol molecules and have suggested the non-random mixing between permeate-polymer or the degree of clustering depends on the solvent properties [63]. The authors have observed a high degree of clustering for methanol molecules, which explains their low diffusion coefficients and low solubility coefficients. Not only does the hydrophilic methanol suffer from the formation of large clusters, but it also suffers from a more tortuous path for transport through the hydrophobic fluorinated sites of the PDMS matrix. As a result, methanol molecules suffer from lower permeability coefficients through the fluorinated PDMS membranes.

However, unlike the individual permeability coefficients, the permeability coefficients of methanol and CO_2 in the mixture experiments increased at the same rate,

when both species were present in a mixture. The disparity observed in the trends of the methanol permeability coefficient between the individual and the binary system setups can be explained based on the interaction (attraction/repulsion) between the transporting moiety and the polymer matrix. It is likely that the swelling of the polymer membranes upon being exposed to methanol vapors provides an easier route for the transport of the bigger methanol clusters. In this case, one species with relatively similar properties as the polymer matrix could drag the other non-similar species with it, much like CO_2 dragging methanol clusters. Hence, a similar increase in the rates of mass transport for methanol and CO_2 were observed.

In the study of PTMSP blends with 1, 6-divinylperfluorohexane, the permeability coefficients of CO_2 increased as a function of the additive content in the blend and that for methanol decreased, as shown in figures 5.7a and 5.7b. The trends of the permeability coefficients of the two species remained the same in both individual and the binary experiment setups, thereby emphasizing on the accuracy of the membrane vent performance under fuel cell conditions. Interestingly, while the difference in the permeability coefficients of CO_2 between pure PTMSP membrane and PTMSP with 40% 1,6-divinylperfluorohexane membrane is about 4%, the difference between the methanol permeability coefficients for the two membranes is 75%. Thus, the rise in α that were observed in polymer blends of PTMSP with 1, 6-divinylperfluorohexane are affected more by the greater decline in the permeability coefficient of methanol than by the permeability coefficient of CO_2.

The lower permeability coefficient of methanol through all compositions of PTMSP and 1,6-divinylperfluorohexane is due to its polarity and the relatively larger size

of methanol molecule clusters in comparison to CO_2. The average void size in PTMSP matrix is 3.3 A°, as has been previously reported [30]. The average diameter of methanol molecule is 6.5 A^o, which is more than two times the size of the void present in PTMSP. Moreover, as has been discussed before, methanol molecules tend to form large clusters due to the intra-molecular hydrogen bonding and as a result the relative size of the molecules becomes larger. Since it is known that the diffusion coefficient is proportional to the square of the difference in the penetrants size and the gap size of the pore, it is apparent that because of its larger size in comparison to the pore size of PTMSP, methanol molecules have lower transport through the matrix [30]. As a result, methanol molecules have lower permeability coefficients than CO_2. Furthermore, upon addition of 1, 6-divinylperfluorohexane, the pore size not only becomes smaller, but it also creates more hydrophobic sites due to the presence of a large number of fluorine atoms. Consequently, the methanol permeability coefficient declines continuously as the weight percent of the additive increases. Therefore, due to the high CO_2 permeability and the continuously decreasing methanol permeability, the values of α is observed to increase with increasing amount of the additive in the polymer blend.

The similarity between the binary and the independent permeation experiments for PTMSP and 1, 6-divinylperfluorohexane polymer blends was not observed in the PDMS and 1, 6-divinylperfluorohexane blends. In the case of PTMSP and its composites, the transport mechanism was dictated predominantly by the free volume available in the matrix and the relative size of the permeating molecule. While in PDMS composite membranes, the methanol molecules could be more easily dragged through the matrix by CO_2 molecules. In the PTMSP composite membrane, the size of micro-voids restricts the

rate at which methanol gets transported through. Thus, the permeability coefficients remain unaltered in the binary system and the trend in both cases is the same for the PTMSP blends.

The performance of the second additive, 1, 9-decadiene, in PTMSP membranes is shown in Figures 5.8a and 5.8b. It was observed that the permeability coefficient trends for the mixture of CO_2 and methanol were different than their individual permeability coefficients. It is observed that for the mixed systems, as the amount of additive in the matrix is increased, the permeability coefficients of methanol increased along with CO_2. As a result the α value is muted, much unlike the independent experiment setup. It is likely that due to the presence of longer chains of 1, 9-decadiene, more flexibility was imparted to the PTMSP backbone. Therefore, the mechanism of methanol being dragged with CO_2 faced less hindrance, which reflected a more facile transport mechanism when both methanol and CO_2 were present together. As a result, the high values of α that were observed in the independent setup is not replicated in the binary setup, and the blend cannot be considered as an optimum choice for CO_2 vent material.

Figure 5.9 shows the theoretically modeled design conditions for a passive DMFC and predicts the vent aspect ratio at a desired efficiency and operating current. Again, each solid line in Figure 5.9 corresponds to the absolute pressure in the DMFC fuel tank. Using the line corresponding to a chosen pressure and a known value of the operating current, we can obtain the aspect ratio, selectivity and efficiency for the CO_2 vent. For example, if a direct methanol fuel cell operates at 500 μA output current, and the allowed pressure inside the tank equals 1.4 atm (1400 kPa)., the corresponding aspect ratio (λ) for the vent design will be 0.94 cm. The fuel efficiency of the CO_2 vent or γ in

this cell is 95%, meaning that only 5% of the consumed fuel is lost through the vent and a CO_2 selectivity of 19. Based on the value of γ of the vent, we can correctly size the fuel tank to provide for a specific mission life. For this particular example, a fuel tank with 2 cm^3 of 12 M methanol will allow the stand alone DMFC to operate at 500 μA for approximately a period of 1 year without refueling. Thus, the inclusion of a CO_2 vent in a stand alone DMFC helps to size the fuel reservoir.

Figure 5.10 shows the dependence of vent efficiency on operating current, as predicted by the theoretical model. The results show that even if the operating current of a passive DMFC decreased by 20%, the efficiency of the vent would exhibit a 1.4% decline. This implies that if a passive DMFC designed to operate at 500 μA experiences an abrupt change in current (e.g. 20% decline), the vent will release CO_2 with 93.6% efficiency and maintain the pressure inside the fuel tank at 1.32 atm. As such, the passive DMFC will not experience a burst in pressure that would have otherwise resulted in significant damages to the DMFC through increased methanol crossover, sealant ruptures and decreased its performance and lifetime.

The above results show that a CO_2 vent fabricated with polymer blends of PTMSP and PDMS membranes have high selectivity for CO_2 over methanol. The results generated from models for the CO_2 vent (Figure 5.9 and 5.10) show high-selectivity, controlled methanol loss, and negligible sensitivity to abrupt changes in operating current of the DMFC. The next section evaluates the performance of the CO_2 vent as a function of temperature and provides experimental validation for carbon dioxide and methanol mixtures.

Figure 5.10 shows the thermogravimetric analysis of PTMSP with 1, 6-divinylperfluorohexane (10:1 wt%) membrane. The negligible weight loss from 20°C to 90°C shows that the vent membrane is thermally stable at the normal DMFC operating temperatures. The onset of first weight loss at 90°C to100°C corresponds to the removal of 1, 6-divinylperfluorohexane, according to the manufacturer's data. The accumulated weight loss at 210°C corresponds to the volatilization of the 10% of 1, 6-divinylperfluorohexane contained in the mixture. The sharp decline observed at about 350°C corresponds to the weight loss due to the PTMSP backbone. The high decomposition temperature suggests that the polymer blend formed by the mixture of PTMSP and 1, 6- divinylperfluorohexane is glassy in nature, and exhibits behavior similar to that observed by Nakagawa et al. for pure PTMSP with a T_g above 300°C [32].

The temperature dependence of the CO_2 and methanol permeability coefficients (Fig. 5.12) shows that while the overall permeability coefficient of CO_2 through PTMSP and 1,6-divinylperflurohexane increased with temperature, the permeability of methanol decreased with temperature. At high temperature, CO_2 molecules acquire sufficient kinetic energy to increase their diffusivity and flux through the membrane. The flux of hydrophobic CO_2 molecules through the pores of the PTMSP matrix is governed by molecular and Knudsen diffusion. This observation is supported by Koros et al. who describe diffusion-dominated transport through the permeating polymer [30]. Furthermore, Wijmans et al. found that the large free volume available in a glassy matrix facilitates diffusion of non-condensable molecules and allows for a pore-flow mechanism [65]. Thus, at higher temperature, the diffusion of CO_2 molecules through the pores increases, leading to an increase in their permeability coefficient.

On the other hand, the transport of methanol through a hydrophobic polymer is a sorption-dominated process. The phenomenon is similar to the behavior observed by Morliere et al. where the decrease in permeability coefficient of the permeate vapors with temperature is due to the decrease in their sorption properties [66]. Chandak et al. have also shown a sorption-based transport mechanism for volatile organic compounds (VOC) [35]. The transport mechanism involves sorption of VOC at the membrane interface, followed by diffusion through the polymer bulk, and desorption at the downstream interface of the polymer membrane [35].

During pervaporation, the VOC molecules come in contact with the upstream interface of the glassy membrane and undergo a phase change resulting in condensation on the porous surface [67]. Barrer et al. have found that the presence of a fine-mesh supported micro-porous structure of PTMSP matrix facilitates the adsorption of condensed vapors [68]. As a result, the pores fill with VOC molecules producing capillary condensation, which blocks the open face of the pores and prevents further adsorption [68, 69]. Prabhakar et al. have also reported a similar observation where the entrapped methanol in the pores of the polymer create bottlenecks in the free volume network[70]. These bottlenecks restrict the flow of methanol through the bulk of the polymer matrix. As temperature increases, more energy is spent in overcoming the barriers to transport, compared to the actual transport mechanism. Consequently, the adsorption of methanol into the porous microstructure of PTMSP and 1,6-divinylperfluorohexane becomes a relatively slow process. Thus, as the temperature increases, sluggish transport of methanol is observed through the polymer matrix resulting in a decrease in the permeability coefficient.

Figure 5.12 also shows that the overall permeability coefficient of methanol is higher in the presence of CO_2 (mixture experiment) than in the individual-component experiment. In the absence of a second species (i.e. CO_2), the bottlenecks for transport formed within the free volume network of the polymer impedes the transport of methanol. However, in a binary system (i.e. combined carbon dioxide and methanol experiments), some of the trapped methanol within the polymer free volume network is flushed out with CO_2. As a result, the permeability coefficient of methanol is higher in the mixture experiment than in individual-component experiment. As a consequence, the figure of merit α, as shown in Figure 5.13, is higher for the individual-component experiment than for the mixture experiment. In both cases, the values of α increase with temperature, indicating a more favorable CO_2 transport mechanism through the polymer matrix.

The Arrhenius relationship, as shown in Equation 5.14, can be used to describe the transport pathway of a molecule through a polymer matrix and understand the transport mechanism. From Figure 5.14, the activation energy of permeation (E_P) of CO_2 was 3.6 and 1.3 kJ/mole for the individual-component experiment and mixture experiment experiment, respectively. A positive E_P value indicates a diffusion controlled mechanism for CO_2 transport. The lower E_P value for CO_2 in the mixture experiment indicates a lower barrier for CO_2 permeation through the polymer matrix in the presence of methanol vapor. The lower value of E_P, and thus better permeability for the mixture experiment is a consequence of the synergistic nature of the combined CO_2-methanol transport.

In a previous study, Merekel et al. reported that the CO_2 permeation activation energy through pure PTMSP is -6.8 kJ/moles [71]. The difference between this activation energy for pure PTMSP and the value here for the PTMSP and 1, 6-divinylperfluorohexane blend, can be attributed to the difference in the polymer properties. Since the polymer blend studied here is more hydrophobic than pure PTMSP [36], CO_2 experiences a smaller barrier to transport. As a result, the hydrophobic CO_2 can more easily diffuse through the polymer blend (lower magnitude of activation energy) in comparison to pure PTMSP.

The activation energy for permeation is a negative quantity (-9 and -8 kJ/mole) for methanol transport through the polymer blend, Figure 5.15. The negative value supports the sorption-dominated transport model for methanol and can be explained by the solution-diffusion theory, Equation 5.13 [32]. The activation energy of permeation is the sum of the activation energy of diffusion (E_D) and the change in enthalpy of sorption (ΔH_S). The enthalpy of sorption of methanol decreases as the methanol vapors condense (compared to methanol in the vapor phase) within the polymer matrix. Thus, ΔH_S for methanol in the polymer blend is a large negative value for vapor at elevated temperature. This causes the value of E_P for methanol to be dominated by the more negative ΔH_S at high temperature. It is not compensated by the small positive value of E_D. As a result, the activation energy for permeation for methanol through the PTMSP and 1, 6-divinylperflurohexane membrane is a negative value.

Figure 5.16 shows the theoretical and experimental efficiency of the CO_2 vent as a function of the operating current. At 10:1 ratio of PTMSP-to-1, 6-divinylperfluorohexane, the efficiency of the vent is approximately 80%, for both

theoretical and experimental cases regardless of the operating current. That is, if the DMFC where to operate with this vent, only 20% of the available fuel would be lost through the CO_2 vent. If a higher PTMSP-to-1, 6-divinylperfluorohexane ratio were used, the efficiency would be higher, reaching to 95% at 1:1 weight ratio of PTMSP-to-1, 6-divinylperflurohexane.

The comparison between the liquid and vapor permeation of methanol (Table 5.3) shows a slight decrease in the permeability coefficient for CO_2 when in the liquid condition, which is due to the low solubility of CO_2 in methanol (Henry's law constant of 0.489 MPa) at room temperature [72]. The permeability coefficient for liquid and vapor methanol are about the same. Methanol vapor forms a thin layer of condensed liquid when it comes in contact with the polymer surface. Thus, the permeability coefficient for methanol liquid and vapor are similar.

5.5 Summary

The permeation behavior of CO_2 and methanol through various compositions of PDMS and PTMSP with 1,6-divinylperfluorohexane and 1,9-decadiene membranes were studied. The results presented in this study indicate that both PDMS and PTMSP membranes were more selective towards CO_2 permeation than methanol. It was also observed that under the same experimental conditions, PTMSP membranes showed higher figure of merit (α) than the PDMS membranes. The better performance of the PTMSP membranes was mostly due to the presence of four hydrophobic methyl groups in each repeat unit that hindered the transport of hydrophilic methanol clusters. Furthermore, upon the addition of 1, 6-divinylperfluorohexane, both PDMS and PTMSP membranes exhibited higher selectivity towards the transport of CO_2 than methanol. The permeation trends of CO_2 and methanol through all compositions of PTMSP and 1, 6-divinylperfluorohexane remained unchanged when both moieties were present as a non-ideal mixture, much like a fuel cell operating condition.

The best performance was obtained with 50 wt% of 1,6-divinylperfluorohexane in PTMSP membrane, such that the permeability coefficient of CO_2 was 1.6×10^{-9} mole-cm-cm^{-2}-day^{-1}-Pa^{-1} and methanol was 1.8×10^{-10} mole-cm-cm^{-2}-day^{-1}-Pa^{-1}. The corresponding α was 9.2, which is approximately 5 times higher than pure PTMSP and 10 times higher than pure PDMS membranes. Based on these results a stand alone DMFC with CO_2 vent was designed. The dependence of the membrane aspect ratio (λ) on the fuel cell operating current has been demonstrated. It was observed that at a given aspect ratio, the efficiency of a CO_2 vent (γ) had limited sensitivity towards abrupt changes in current. As a result, the novel CO_2 vent can tolerate unforeseen bursts in pressure due to

changes in current without having a drastic impact on the fuel cell design and performance.

The selectivity of a 10 to 1, PTMSP to 1, 6-divinylperfluorohexane membrane as a function of temperature was studied. It was observed that the permeability coefficient of CO_2 increased with temperature while that for methanol decreased. The observed behavior was due to the difference in transport mechanism of CO_2 and methanol through the polymer blend. The transport process of small, hydrophobic CO_2 molecules through the hydrophobic membrane is diffusion controlled and the rate of transfer increased with temperature. On the contrary, since the transport of methanol is sorption controlled and requires condensation, the permeability coefficient of methanol decreased with increase in temperature. Furthermore, the solution-diffusion model in conjunction with the measured activation energies of permeation (E_P) also supported the transport process of CO_2 and methanol molecules. The positive E_P for CO_2 suggested high rates of diffusivity while the negative E_P for methanol vapors suggested that the value of E_P was strongly influenced by the large negative change in enthalpy of sorption (ΔH_S). It was also observed that the activation energy of permeation of CO_2 through this polymer blend was lower than the corresponding value through pure PTMSP.

The theoretical model for CO_2 vent was validated with experimental results. At 10:1 ratio of PTMSP-to-1, 6-divinylperfluorohexane, the efficiency of the vent was approximately 80%, regardless of the operating current. Based on the above results, at higher concentrations of 1, 6-divinylperfluorohexane in the polymer blend, higher efficiencies could be achieved. It was observed that on contact with liquid methanol, the vent membrane showed small decreases in CO_2 permeability due to low solubility of CO_2

in methanol. However, overall, the vent membrane was still more selective to CO_2 than methanol.

The above results show that the CO_2 vent is a feasible method of discharging CO_2 from the fuel tank of a DMFC. Its selectivity towards CO_2 over methanol remains unaltered at high temperatures and when in contact with liquid methanol. Moreover, the vent can be customized using theoretical model to achieve a desired efficiency and performance.

CHAPTER 6

LI-ION BATTERIES FOR LOW POWER, HYBRID POWER MODULES

6.1 Objective

Small, portable electronic devices need power supplies that have long life, high energy efficiency, high energy density, and can deliver short power bursts. Hybrid power sources that combine a high energy density fuel cell, or an energy scavenging device, with a high power secondary battery are of interest in sensors and wireless devices. However, fuel cells with low self-discharge have low power density and have a poor response to transient loads. A low capacity secondary lithium ion cell can provide short burst power needed in a hybrid fuel cell-battery power supply.

The objective of this chapter is to study the polarization, cycling, and self discharge of commercial lithium ion batteries as they would be used in the small, hybrid power source. The performance of 10 Li-ion variations, including organic electrolytes with $Li_xV_2O_5$ and $Li_xMn_2O_4$ cathodes and LiPON electrolyte with a $LiCoO_2$ cathode were evaluated. This chapter presents work that has been previous published in the Journal of Power Sources [2].

6.2 Result and Discussion

The capacity of the commercial Li-ion cells was tested in order to determine the portion of the rated capacity available between 2.5 and 4.2 V. The results for ML621, VL621 and NX0201 cells are shown in Figure 6.1. For the ML621, the available capacity is nearly a linear function of the charge voltage. This was repeated for 20 cycles for three different cells. This is somewhat different than results previously reported for laboratory prepared Li-ion cells with a $Li_xMn_2O_4$ cathode [73, 74]. However, this phenomenon has been observed previously in the literature with solid electrolytes [75] and carbon composite electrodes [76].

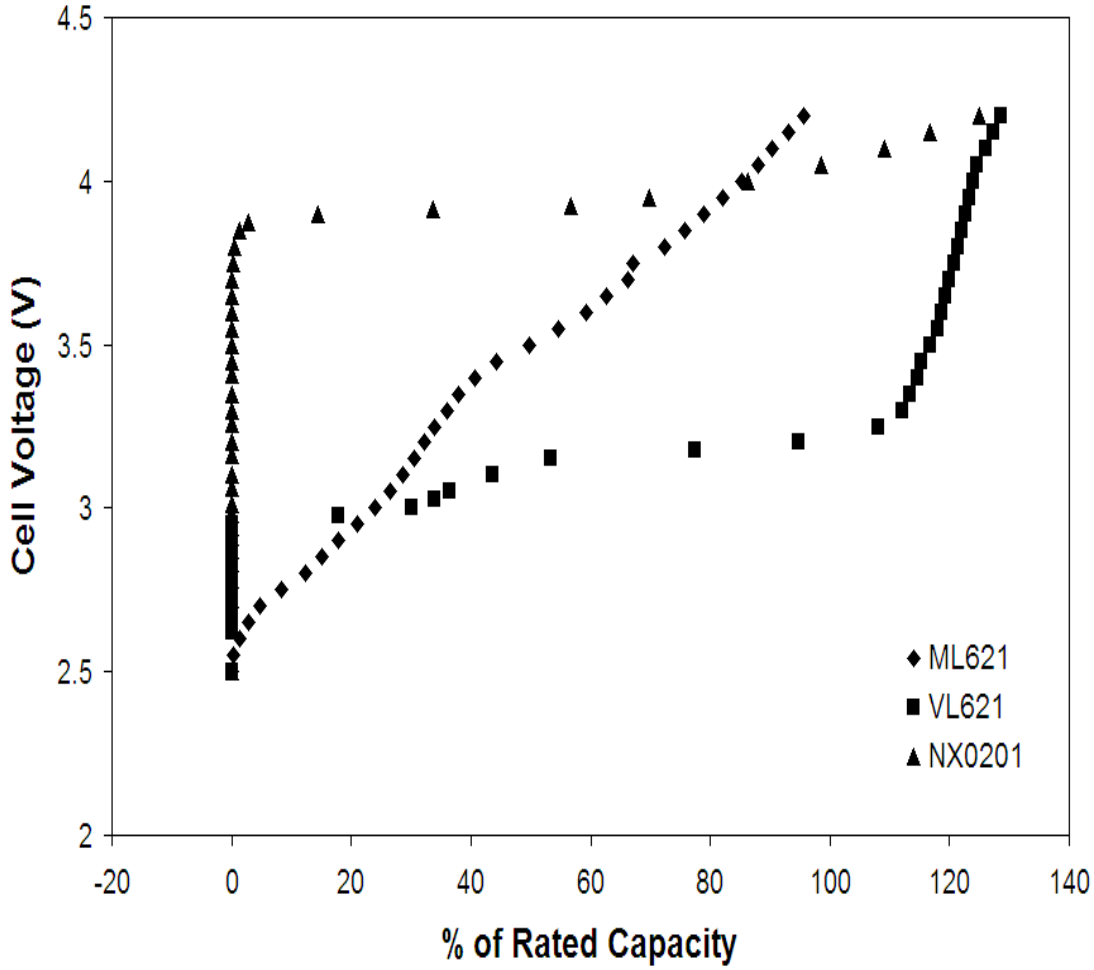

Figure 6.1: Cell voltage vs. rated capacity for ML621, VL621 and NX0201 cells

The vanadium oxide cell, VL621, showed two regions during cycling, which is consistent with reported behavior of polycrystalline V_2O_5 cathode Li-ion cells [77, 78]. Between 2.5 and 3 V, there is nearly zero stored charge. Between 3.0 and 3.2 V, 110 % of the rated capacity is available. This provides a stable and desirable performance range.

That is, one can use the full capacity of the battery at nearly constant voltage. Overcharging of the V_2O_5 cells resulted in a steep rise in the voltage with minimal gains in the stored charge. Finally, the NX0201 cell with the LiPON electrolyte and Li_xCoO_2 cathode showed minimal charge storage capability below 3.8 V. At voltages higher than 3.8 V, a steady, linear voltage increase was observed throughout the duration of the charge cycle.

Li-ion cells are operated at relatively high voltage corresponding to a high free energy change between the reactant and product states. There are several contributors to self discharge in electrochemical systems including faradaic processes due to decomposition of either the electrode or the electrolyte. A portion of the self discharge occurs during recharge, where the cell voltage is raised higher than the open circuit voltage.

Self discharge is especially important in hybrid, portable power sources because it compromises the energy density of the primary energy source, the fuel cell, by adding an additional load. In the hybrid sources considered here, the battery spends most of its time at open circuit or being recharged at a low C-rate. Typically, the self discharge rate is used to evaluate the shelf-life of an electrochemical cell and is measured by fully charging the cell, allowing it to sit at open circuit for a period of time and then discharging the cell at low current. The columbic difference between the charge and discharge steps is then divided by the open circuit time. The self discharge is given as the average current accounting for the lost charge. In the case of a hybrid power supply, open circuit shelf-life is not an issue. Rather, the charge lost during recharge at low C-

rate following a shallow discharge cycle more closely captures the operating mode of the hybrid power source.

In this work, the self-discharge was evaluated as function of cell potential for an operation mode which closely matches the performance of a battery in the hybrid power source. The batteries were charged to the operating voltage of interest: 3.5 V, 3.75 V, 4.0 V, and 4.2 V. The cells were then discharged at low current for 100 s corresponding to a very low depth-of-discharge, below 0.1%, which is typical of the discharge of the battery during operation in the hybrid power source. The cells were recharged at the same current to the original operating voltage. The recharge time was greater than 100 s in each case. The time in excess 100 s accounts for the excess charge which has be supplied due to self-discharge. The loss in charge is represented as a self-discharge current, i_{SD}, by averaging the charge over the time for the whole cycle, Equation 6.1.

$$i_{SD} = \frac{i_c(t_c - t_d)}{t_c + t_d} \tag{6.1}$$

Where i_c is the charging current, t_c is the recharge time, and t_d the discharge time, 100 s. The self-discharge were evaluated for all 10 Li-ion cells listed, shown earlier in Chapter 3, Table 3.1. A representative summary of those results, providing a full picture of the performance, is provided. At least three duplication cells were tested in each case. The data points shown are the result of the average of the final five cycles of each cell and the error in all measurements was taken as 3 times the standard deviation.

The self discharge for VL621 Lithium ion cells was measured at 4.2 V with charge/discharge currents of 10, 8, 6 and 2 µA and is shown in Figure 6.2. The loss due to self-discharge increased with the charge current. As expected, the self discharge increased with charging current when the electrode overpotentials were the highest.

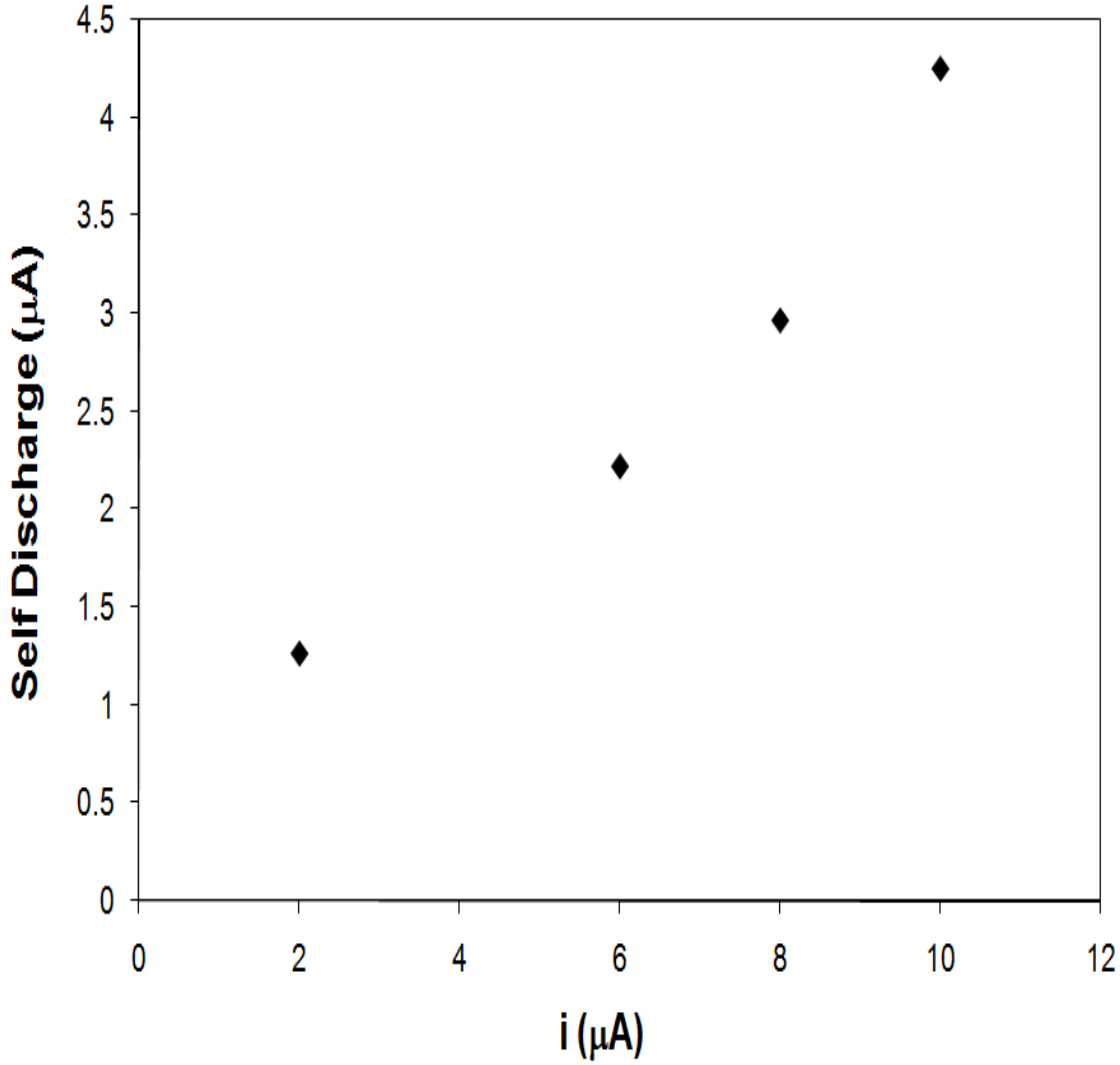

Figure 6.2: Self Discharge current vs. charge/discharge current for VL621 Li-ion cells charged to 4.2V

Identical experiments were performed with the NX0201 cells at 4.2 V with charge/discharge currents of 1.0, 0.8, 0.6 and 0.2 µA, as shown in Figure 6.3. The magnitude of the self discharge was less than the VL621. The self-discharge current for

the NX0201 was much less than with self discharge for the vanadium oxide cell, even though its electrochemically active area is significantly larger. This is consistent with literature reports that LiPON electrolyte cells show significantly lower self-discharge than their counterparts with organic electrolytes [75, 79-81].

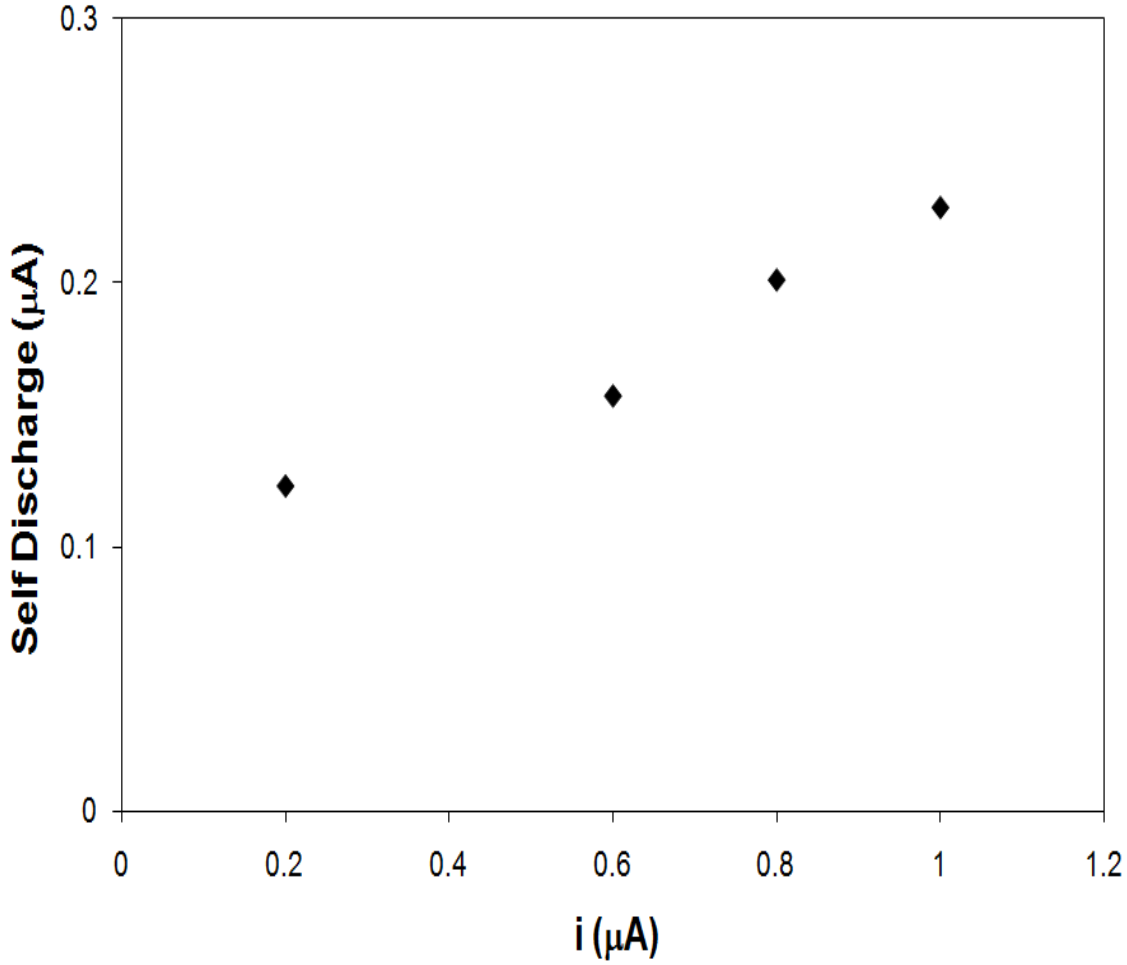

Figure 6.3: Self-discharge current vs. charge/discharge current for FrontEdge NX0201 thin film Li-ion cells charged to 4.2V

The self discharge for all cells was also investigated as a function of the operating voltage. The self-discharge of VL1220 and ML414 cells as a function of voltage are shown in Figure 6.4 and Figure 6.5, respectively.

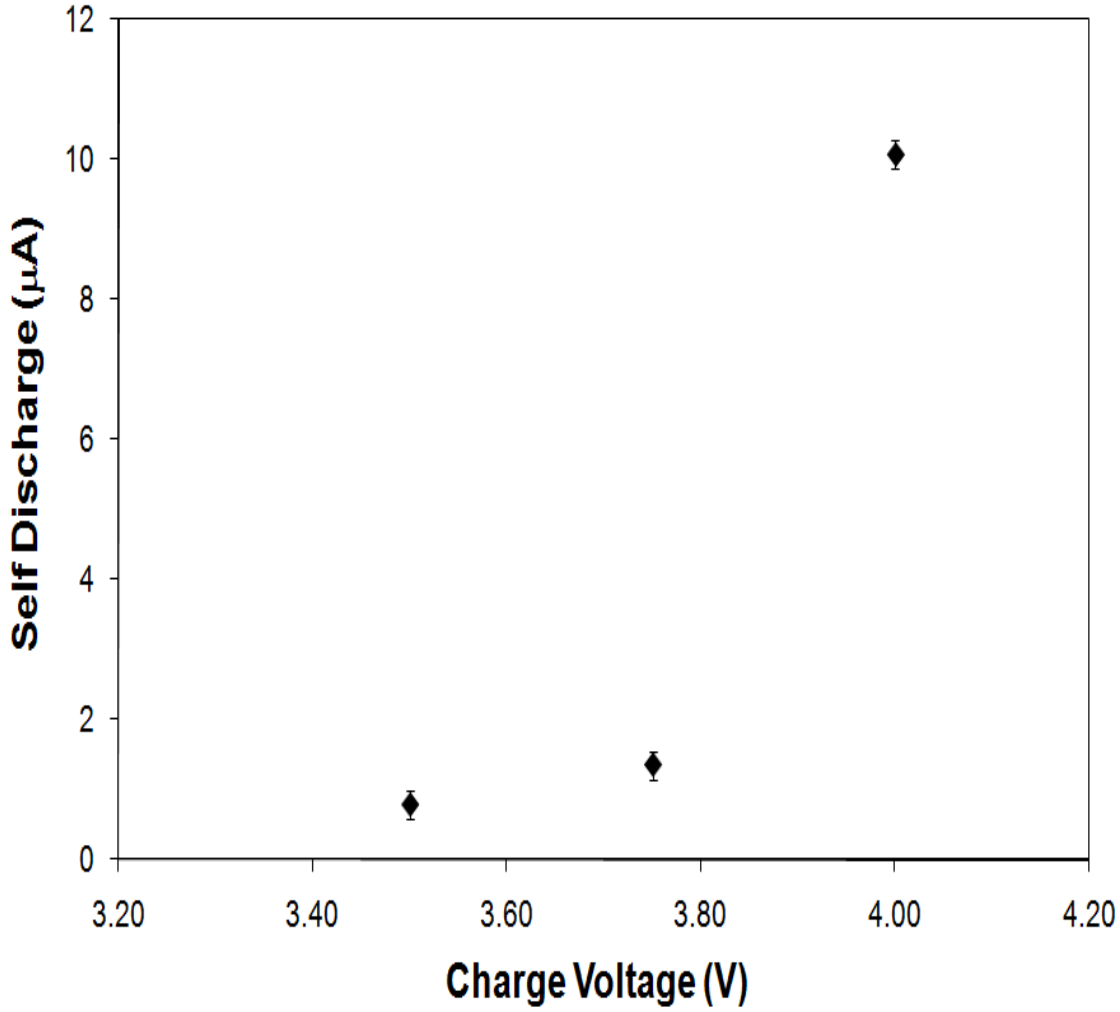

Figure 6.4: Self discharge current vs. charge voltage for VL1220 cells.

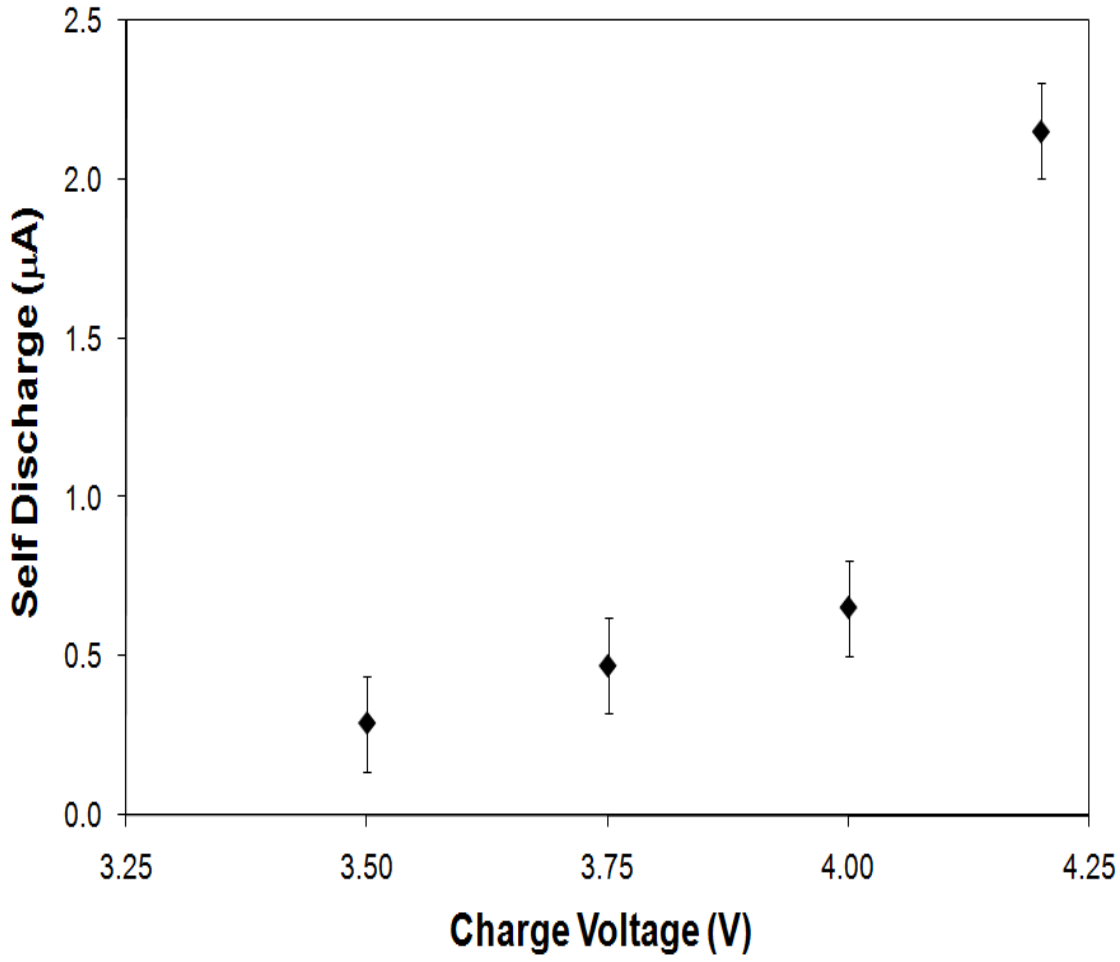

Figure 6.5: Self discharge current vs. charge voltage for ML414 cells

Overall, the self-discharge of the Lithium ion cells increased with cell voltage due to the higher overpotentials at the electrode surfaces during recharge. This was also the case for the LiPON electrolyte thin film cell. V. The self-discharge is function of the state-of-charge for the vanadium oxide cells and rapidly increases at higher a higher state-of-charge (higher voltage). For example, the self-discharge increases more than 10

times when the voltage increased from 3.5 to 4.0 V. For the manganese cells, the effect is less pronounced, showing only a 2.5 fold increase over the same voltage range. This may be due to similar states of charge for the manganese cells at 3.5 and 4.0 V, shown in the Figure 6.1. The geometric area of the cells was measured by disassembling three of each type of battery and measuring the area of the cathode pellet. This was done for the vanadium oxide and manganese oxide cathode cells. The self-discharge density (self-discharge per unit area) can be determined for the ML and VL series cells, as shown in Figures 6.6 and 6.7, respectively, at 3.75 V. The self-discharge for the VL series and ML series cells compares favorably with previously reported $LiCoO_2$ cathode cells measured at open circuit at similar voltages, 11 μA cm^{-2-} [52]. Improvements in the Li-ion cathode have led to a reduction in the self discharge. Also, the results for the self-discharge of VL2320 and VL2330 cells shown in Figure 6.6 verify that the self discharge is a function of the electrode surface area exposed to the electrolyte and not the cell capacity.

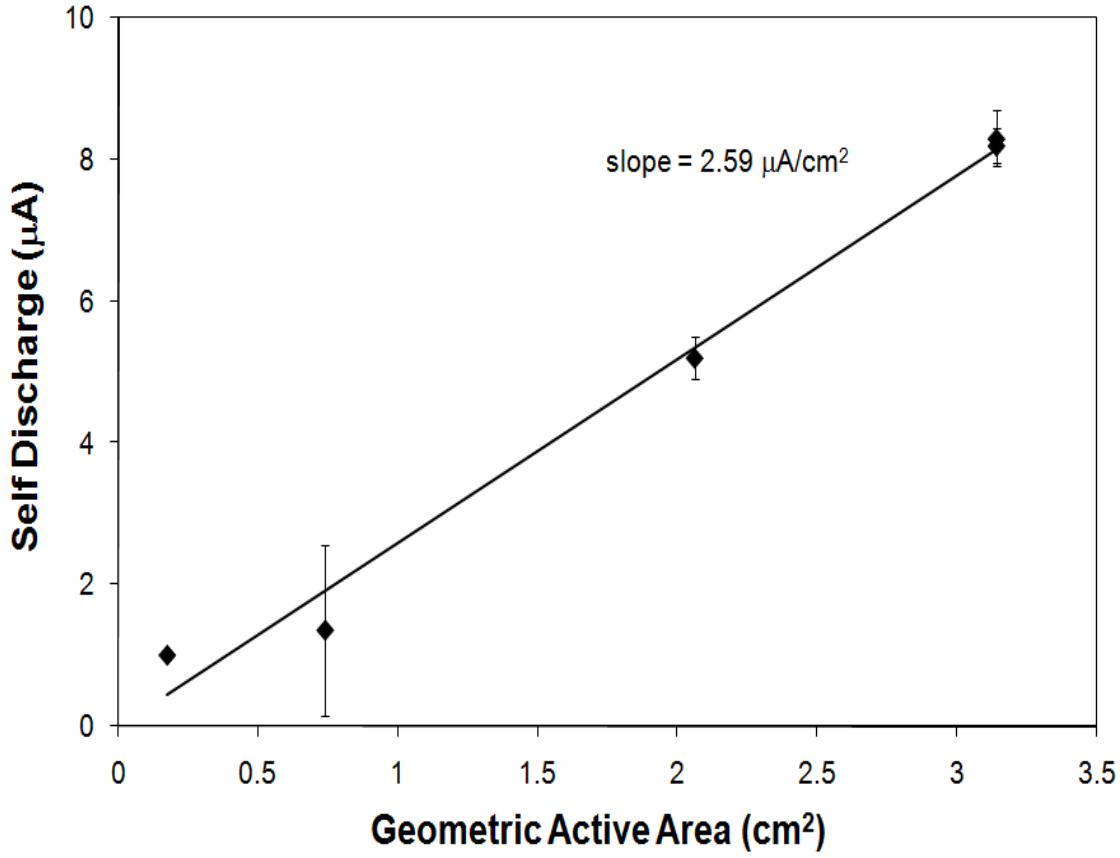

Figure 6.6: Self discharge of VL series lithium ion button cells at 3.75V.

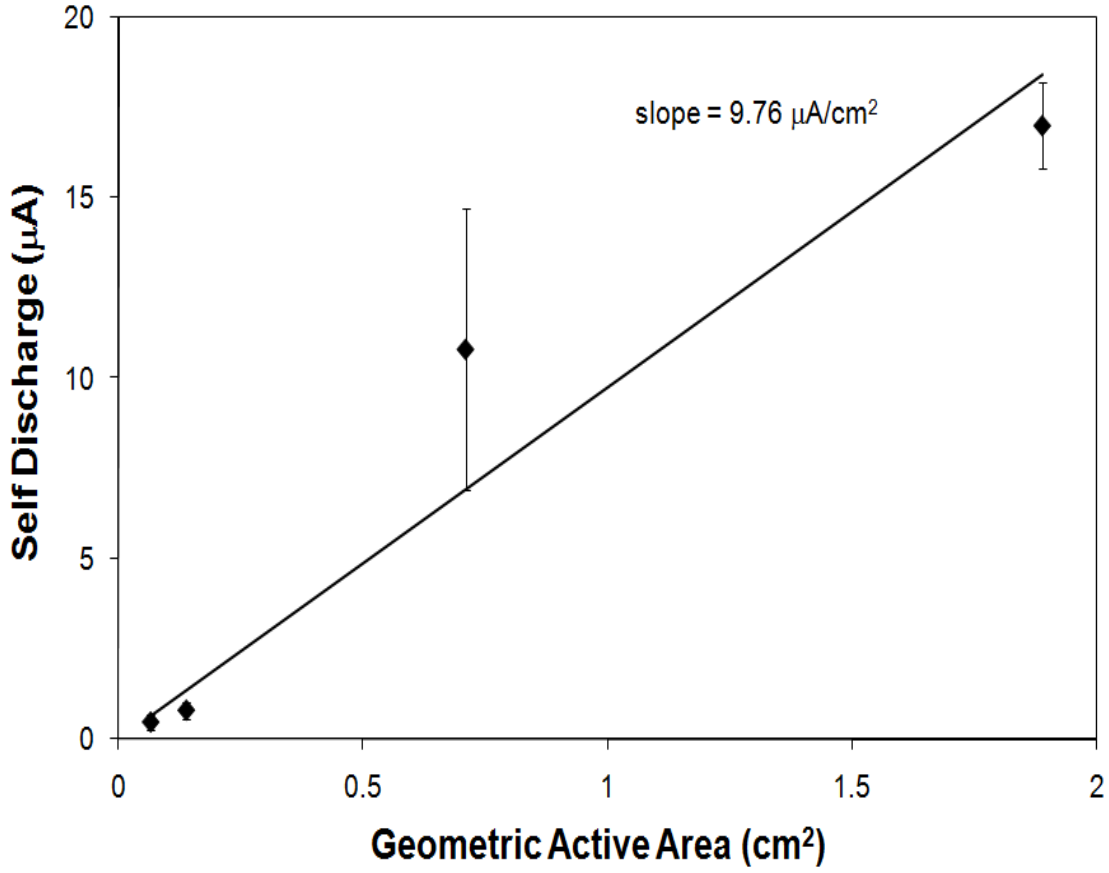

Figure 6.7: Self discharge of ML series lithium ion button cells at 3.75V.

The vanadium cells generally have lower self-discharge than their manganese counterparts, even though the cells were constantly operated in the overcharge region. The overcharge caused the self-discharge of the VL cells to significantly increase at high voltage where it surpassed that of the ML cells above 4.0 V. Both the ML and VL series cells have inferior performance to the NX0201 thin film LiPON cell.

Although the self-discharge can play an important role in energy efficiency, the self-discharge rates were generally acceptable for hybrid power supplies. The main energy loss encountered in the hybrid power supply is the energy loss due to electrode polarization. When a cell is discharged, the potential difference between the two electrodes is less than during charging due to electrode polarization. At zero current, the cell remains at open circuit voltage. As the cell is discharged, the cell voltage drops, due to activation and concentration overpotential. The potential difference between charging and discharging increases with current density and thus lowers the energy efficiency. The discharge efficiency, ε, can be defined as the discharge voltage, V_d, divided by charging voltage, V_c, as shown in Equation 6.2.

$$\varepsilon = \frac{V_d}{V_c} \tag{6.2}$$

The discharge efficiency is not a significant concern when plug-power is used to recharge the lithium ion cell because of the virtually unlimited supply of current. In the case of a fuel cell powered hybrid, the energy loss due to discharge efficiency can be a significant energy drain.

Cell polarization measurements were performed on all cells at 2C, 1C, 1/2C, 1/5C, and 1/10C rates. The results for the ML414 cells is presented in Table 6.1. The cells show two clear trends. First, the discharge efficiency improves as the C-rate is decreased. This was true for all the cells tested at 4.2, 4.0, 3.75 and 3.5 V. Second, the peak efficiency at all rates was observed at 4.0 V. This is likely a balance of two effects. First, the activation overpotential increases as the discharge rate increases. Second, as the discharge rate is increased, the number of lithium ions available for deintercalation at the Li-ion anode is reduced, leading to a depletion overpotential at the electrode surface due

to mass transport. Thus, the higher state of charge and lower discharge C-rate favor improved energy efficiency.

Table 6.1: Discharge efficiency as a function of discharge rate and charge potential for ML414 cells.

	Discharge Rate				
Voltage	2C	1C	1/2 C	1/5C	1/10C
4.20	0.26	0.59	0.77	0.91	0.94
4.00	0.60	0.78	0.88	0.96	0.97
3.75	0.45	0.68	0.82	0.93	0.95
3.50	0.43	0.67	0.81	0.93	0.95

Table 6.2: Discharge efficiency as a function of discharge rate and charge potential for VL1220 cells.

	Discharge Rate				
Voltage	2C	1C	1/2 C	1/5C	1/10C
4.20	0.69	0.79	0.86	0.92	0.94
4.00	0.75	0.85	0.91	0.97	0.98
3.75	0.76	0.85	0.91	0.97	0.98
3.50	0.78	0.86	0.92	0.97	0.98

Identical experiments were conducted with VL1220 cells and are given as Table 6.2. As in the previous case, the cell polarization decreases at lower C-rate. However, for the vanadium oxide cells, the highest efficiencies were observed at the lowest tested cell voltage, 3.5 V, at all rates, although there was only a modest increase over the performance at 4.0 V. In the most extreme case, 4.2 V operating voltage and 2C discharge, the efficiency for the VL series cell is 165 % greater than the ML series. At modest conditions, 3.5 V and C/10, only a 3 % improvement was realized.

Polarization experiments were also performed with the NX0201 thin film LiPON cell, which are summarized in Table 6.3. As with other cells, the discharge efficiency increased with decreasing C-rate. However, in this case the efficiency steadily improved from 3.5 to 4.2 V. This is clearly due to the LiPON operating window and higher state-of-charge at high voltage, as shown in Fig. 6.1. The LiPON cell had nearly zero stored charge below 3.8 V.

Table 6.3: Discharge efficiency as a function of discharge rate and charge potential for NX0201 cells.

	Discharge Rate				
Voltage	2C	1C	1/2 C	1/5C	1/10C
4.20	0.982	0.991	0.995	0.998	0.999
4.00	0.981	0.991	0.995	0.998	0.999
3.75	0.843	0.922	0.963	0.989	0.995
3.50	0.737	0.864	0.922	-	0.981

The cell polarization experiments are useful in determining the performance of the cells during operation, however, other factors contribute to the battery's performance during the hybrid cell's lifetime. First, capacity-fade of Li-ion cells during cycling has been documented and is accompanied by increased self discharge and increased cell polarization during operation. However, in this investigation, the depth-of-discharge for each cycle is low, which reduces these effects. Second, a 2C discharge rate for the NX0201 cell corresponds to less than C/10 for the ML621 and 0.5C for the VL 621, both of which have a much higher capacity at the same cell volume and lower surface area.

In order to compare the performance of the thin-film LiPON cell with the higher capacity VL cell of comparable volume, the discharge experiments were performed at 1 and 3 mA with NX0201 and VL621 cells charged to 3.5 V. Figure 6.8 shows the cell voltage during discharge for the NX0201 (at 1 and 3 mA) and the VL621 cell (at 1 mA) as a function of cycle number. All three cells show stable performance with cycle number during these shallow discharge experiments. However, the discharge voltage at 1 mA was significantly higher than for the VL 621 cell than the NX0201. The volume of the two cells were approximately the same, however the capacity of the VL 621 was higher than the NX0201. A 1 mA discharge represents only a 0.67C discharge for the VL621, whereas the same current is a 2.5C discharge for the NX0201. However, the NX0201 has a larger electrode area than the VL621 and the NX0201 has limited capacity at low discharge voltages, whereas the VL series cell is almost fully charged (Fig. 6.1).

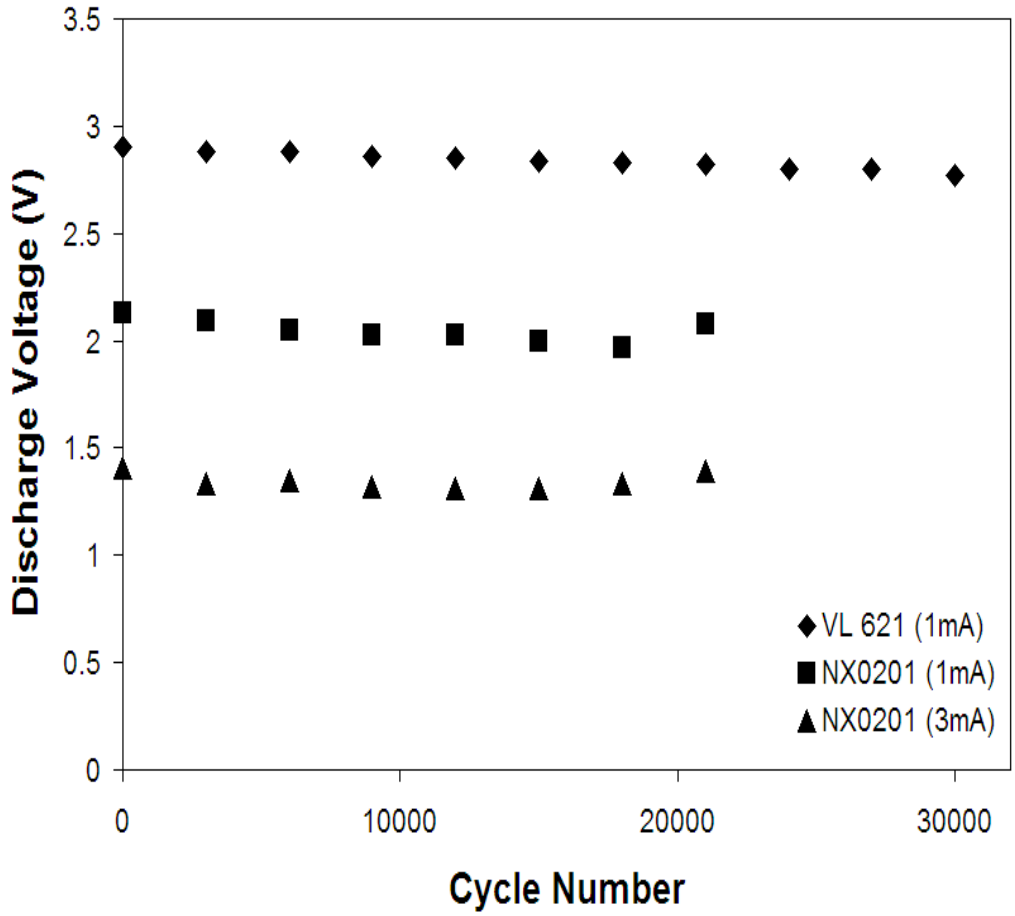

Figure 6.8: Discharge Voltage as a function of cycle number for shallow discharge experiments with vanadium oxide cathode VL621 and LiPON electrolyte NX0201 cells.

The voltage efficiency of all cells decreased slowly with cycling. The VL621 cells showed a 4.5% decrease in the discharge voltage after 30,000 cycles. On the other hand, the LiPON cells showed a decrease of 7.5% and 5.7% for the 1 and 3 mA experiments, respectively. The NX0201 cell performance became erratic at 21,000 cycles, sometimes showing negative discharge potentials or an inability to reach the desired discharge rate and the experiments were terminated. The high discharge rate for

the NX0201 (3 mA corresponds to 7.5C) is likely a contributing factor in overstressing the cell.

Figure 6.9 shows the low depth-of-discharge cycling performance for the VL621 cell with a 3 mA discharge pulse. The cell shows a rapid decrease in performance with cycle number and no useful work is obtained after 250 cycles. Therefore, for the vanadium oxide cells to be competitive, one needs to oversize the cell such that the discharge is no greater than 1 C, while the thin film LiPON cells are clearly superior at high C rates, although efficiency is sacrificed.

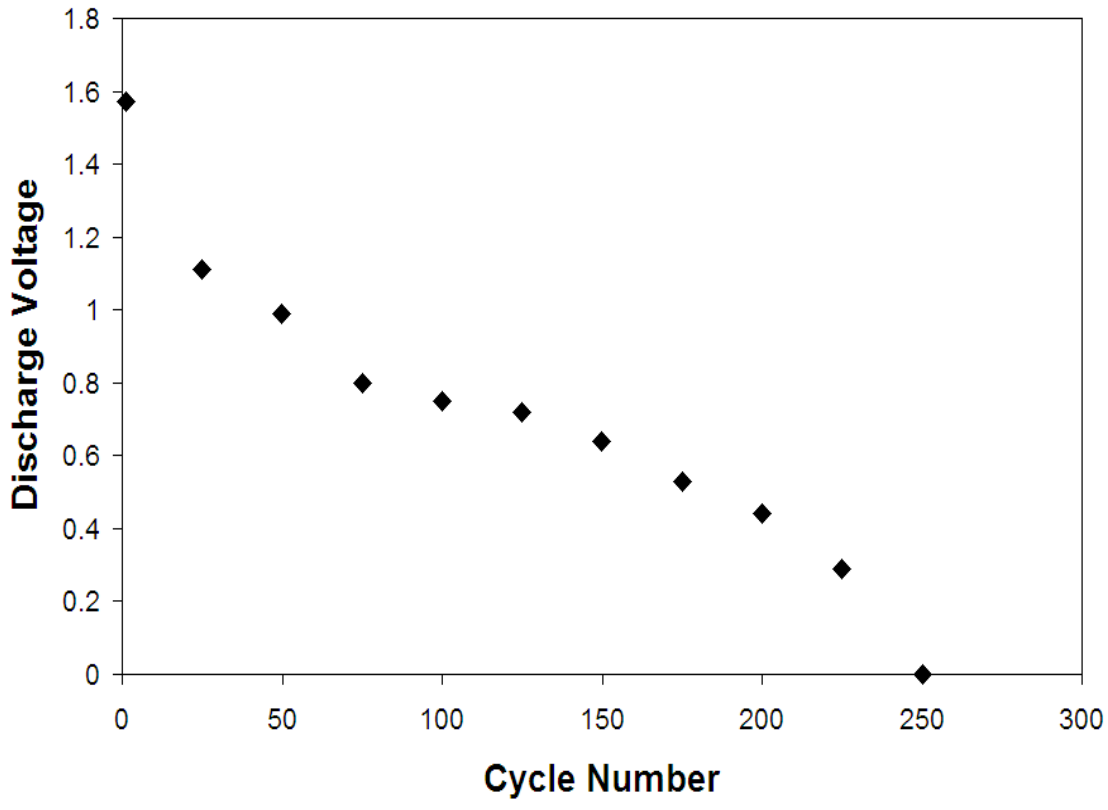

Figure 6.9: Discharge Voltage as a function of cycle number for VL621 cells discharged at 3 mA.

6.3 Summary

Several commercial secondary Li-ion cells have been investigated for use in low power hybrid power supplies. The self discharge of the LiPON electrolyte cells was found to be more than an order of magnitude superior to the manganese and vanadium oxide cathode cells with organic electrolytes despite their larger electrode area. However, the manganese oxide and vanadium oxide cell showed a superior self discharge behavior to previously reported commercial cells with a $LiCoO_2$ cathode and similar electrolyte. Their self discharge values were 9.76 and 2.59 $\mu A\ cm^{-2}$.

The cells were also tested for their polarization performance and lifetime stability with low depth of discharge pulses. The LiPON NX0201 cell showed the best polarization performance to any other cell, though it should be noted that the vanadium oxide cells showed a much higher efficiency, as high as 165%, than manganese oxide cells under identical operating conditions. Finally, both the vanadium oxide cathode and LiPON electrolyte cells showed excellent cycling performance at low depth of discharge, < 0.01 % depth of discharge. The performance of the LiPON cells was stable for 21,000 cycles at 7.5 C, while the vanadium oxide cells were stable at 2/3 C for over 30,000 cycles. However, at 2 C the cycling performance of the vanadium oxide cells was poor, yielding usable power for only 250 cycles with efficiencies always less than 45 %.

CHAPTER 7

CONCLUSIONS

The objective of this dissertation was to explore the issues in designing a hybrid power module for low power electronics. This work advances the DMFC performance for systems where space and volume are a premium. The performance of phospho-silicate glass (PSG) membrane as a barrier to methanol transport has been investigated and the optimum fabrication condition has been demonstrated. New polymer blends have been synthesized and investigated for fabricating CO_2 vent in a DMFC. This technique provides a low cost and simple solution to the CO_2 accumulation problem inside the fuel tank of a DMFC. Finally, low loss commercial Li-ion batteries were identified and their performance as a function of self-discharge and voltage efficiency were studied.

Silicate glasses deposited by plasma enhanced chemical vapor deposition (PECVD) have traditionally been used as low-loss electrical insulators in microelectronic devices. Incomplete oxidation of silane and phosphine in the plasma chamber introduced defect sites (-OH) groups in the otherwise dense tetrahedral structure. Careful and systematic variation of deposition condition increased the percentage of phosphorus and –OH groups in the glass structure. A peak conductivity of 2.52×10^{-4} S/cm was achieved for PSG deposited at 400 W RF Power, 400 mTorr chamber pressure, 100 °C substrate temperature and a nitrous oxide flow rate of 80 sccm. This value is 2.5 times greater than the target conductivity value of 1×10^{-4} S/cm and 250 times greater than the ionic conductivity of pure silicon dioxide films. DMFC performance with Nafion-PSG hybrid PEM showed lower methanol permeability and improved current density compared to pure Nafion PEM.

The process of CO_2 discharge from the anode chamber without significant loss of methanol raises a key challenge in fuel cells designed with minimal volume and passive components. The performance of two polymer membranes, poly (dimethyl siloxane) (PDMS) and poly (1-trimethyl silyl propyne) (PTMSP), for use as a CO_2 vent has been presented. In both cases, the membrane was more selective to CO_2 than methanol. The addition of hydrophobic additives like 1, 6-divinylperfluorohexane and 1,9-decadiene to PDMS and PTMSP membranes enhanced the selectivity resulting in values of α as high as 9.2. It was also observed that the performance of the vent improved with increase in temperature. Furthermore, an experimentally validated model was developed to predict the efficiency of CO_2 vent. At α of 9.2, the vent was 95% efficient.

The study of Li-ion batteries evaluated the trade-offs between battery type, state of charge, and battery capacity to find the most energy efficient operating condition. The LiPON NX0201 cell showed better polarization performance than the two Panasonic coin cells (manganese oxide cells and vanadium oxide cells). The vanadium oxide cells showed a much higher efficiency, as high as 165%, than manganese oxide cells under identical operating conditions. Finally, both the vanadium oxide cells and LiPON electrolyte cells showed excellent cycling performance at low depth of discharge, i.e., less than 0.01 % depth of discharge. The performance of the LiPON cells was stable for 21,000 cycles at 7.5 C, while the vanadium oxide cells were stable at 2/3 C for over 30,000 cycles. However, at 2 C the cycling performance of the vanadium oxide cells was poor, yielding usable power for only 250 cycles with efficiencies always less than 45 %.

REFERENCES

[1] Rincón-Mora, G. A. In *Energy Harvesting Technologies*, **2009**, pp. 287-321.

[2] Prakash, S.; Mustain, W. E.; Kohl, P. A. *Journal of Power Sources, In Press, Accepted Manuscript*.

[3] EG&G Services. Parsons, I. *Fuel Cell Handbook*, Office of Fossil Energy. U.S. Departement of Energy: Morgantown,WV **2000**.

[4] Heinzel, A.; Hebling, C.; Muller, M.; Zedda, M.; Muller, C. *Journal of Power Sources*, **2002**, *105*, 250-255.

[5] Cooper, H. W. *Chemical Engineering Progress*, **2007**, *103*, 34-43.

[6] Moore, C. W., **2005**, pp. 210 pp.

[7] Lamy, C.; Leger, J.-M.; Srinivasan, S. *Modern Aspects of Electrochemistry*, **2001**, *34*, 53-118.

[8] Li, X. *Principles of Fuel Cells* **2006**.

[9] Chu, D. R.; Jiang, R. Z. *Electrochimica Acta*, **2006**, *51*, 5829-5835.

[10] Liu, F. Q.; Lu, G. Q.; Wang, C. Y. *Journal of the Electrochemical Society*, **2006**, *153*, A543-A553.

[11] Rajesh, B.; Thampi, K. R.; Scibioh, A.; Viswanathan, B.; Kaneco, S.; Ohta, K. *Photo/Electrochemistry & Photobiology in the Environment, Energy and Fuel*, **2004**, 91-137.

[12] Narayanan, S. R.; Valdez, T. I.; Kindler, A.; Witham, C.; Surampudi, S.; Frank, H. *Annual Battery Conference on Applications and Advances, 15th, Long Beach, Calif., Jan. 11-14, 2000*, **2000**, 33-36.

[13] Nogami, M.; Usui, Y.; Kasuga, T. *Fuel Cells*, **2001**, *1*, 181-185.

[14] Chapple-Sokol, J. D.; Pliskin, W. A.; Conti, R. A. *Jounal of Electrochemical Society*, **1991**, *138*, 3723-3726.

[15] Abe, Y.; Hosono, H.; Ohta, Y.; Hench, L. L. *Physical Review B*, **1988**, *38*, 10166-10169.

[16] Abe, Y.; Shimakawa, H.; Hench, L. L. *Journal of Non-Crystalline Solids*, **1982**, *51*, 357-365.

[17] Uma, T. N. *Journal of Non-Crystalline Solids*, **2005**, *351*, 3325.

[18] Uma, T.; Nogami, M. *Journal of Membrane Science*, **2006**, *280*, 744-751.

[19] Nogami , M.; Nagao, R.; Wong, C.; Kasuga, T.; Hayakawa, T. *Journal of Physical Chemistry B*, **1999**, *103*, 9468-9472.

[20] Hiroki Itoh, y. O., Masaharu Horiguchi. *Journal of Non-Crystalline Solids*, **1986**, *88*, 83-93.

[21] Abe, Y.; Li, G. M.; Nogami, M.; Kasuga, T.; Hench, L. L. *Journal of the Electrochemical Society*, **1996**, *143*, 144-147.

[22] Park, Y. I.; Kim, J. D.; Nagai, M. *Journal of Materials Science Letters*, **2000**, *19*, 2251-2253.

[23] Fernandez-Lorenzo, C.; Esquivias, L.; Barboux, P.; Maquet, J.; Taulelle, F. *Journal of Non-Crystalline Solids*, **1994**, *176*, 189-99.

[24] Matsuda, A.; Kanzaki, T.; Kotani, Y.; Tatsumisago, M.; Minami, T. *Solid State Ionics*, **2001**, *139*, 113-119.

[25] Ceiler, M. F.; Kohl, P. A.; Bidstrup, S. A. *Journal of the Electrochemical Society*, **1995**, *142*, 2067-2071.

[26] Yang, H.; Zhao, T. S.; Ye, Q. *Journal of Power Sources*, **2005**, *139*, 79-90.

[27] Lu, G. Q.; Wang, C. Y.; Yen, T. J.; Zhang, X. *Electrochimica Acta*, **2004**, *49*, 821-828.

[28] Kelley, S. C.; Deluga, G. A.; Smyrl, W. H. *Aiche Journal*, **2002**, *48*, 1071-1082.

[29] Blum, A.; Duvdevani, T.; Philosoph, M.; Rudoy, N.; Peled, E. *Journal of Power Sources*, **2003**, *117*, 22-25.

[30] Koros, W. J.; Fleming, G. K. *Journal of Membrane Science*, **1993**, *83*, 1-80.

[31] Rogers, C. E. ed. *Permeation of gases and vapors in polymers.*, Elsevier Applied Science Publishers LTD: Essex, England\ **1985**.

[32] Nakagawa, T.; Saito, T.; Asakawa, S.; Saito, Y. *Gas Separation & Purification*, **1988**, *2*, 3-8.

[33] Jordan, S. M.; Koros, W. J. *Journal of Polymer Science Part B-Polymer Physics*, **1990**, *28*, 795-809.

[34] Zimmerman, C. M.; Singh, A.; Koros, W. J. *Abstracts of Papers of the American Chemical Society*, **1998**, *215*, U326-U326.

[35] Chandak, M. V.; Lin, Y. S.; Ji, W.; Higgins, R. J. *Journal of Applied Polymer Science*, **1998**, *67*, 165-175.

[36] Prakash, S.; Mustain, W.; Kohl, P. A. *Journal of Power Sources*, **2008**, *185*, 392-400.

[37] Blomgren, G. E. *Journal of Power Sources*, **1999**, *82*, 112-118.

[38] Kim, H.; Choi, J.; Sohn, H. J.; Kang, T. *Journal of The Electrochemical Society*, **1999**, *146*, 4401-4405.

[39] Kazunori, O.; Yokokawa, M. In *10th. International Seminar of Primary and Secondary Battery Technology Applications*; Florida Educational Seminars: Deerfield Beach, FL, **1993**.

[40] Mizushima, K.; Jones, P. C.; Wiseman, P. J.; Goodenough, J. B. *Materials Research Bulletin*, **1980**, *15*, 783-789.

[41] Bates, J. B.; Dudney, N. J.; Lubben, D. C.; Gruzalski, G. R.; Kwak, B. S.; Yu, X. H.; Zuhr, R. A. *Journal of Power Sources*, **1995**, *54*, 58-62.

[42] Zhang, J. G.; McGraw, J. M.; Turner, J.; Ginley, D. *Journal of The Electrochemical Society*, **1997**, *144*, 1630-1634.

[43] Park, N. G.; Ryu, K. S.; Park, Y. J.; Kang, M. G.; Kim, D. K.; Kang, S. G.; Kim, K. M.; Chang, S. H. *Journal of Power Sources*, **2002**, *103*, 273-279.

[44] Shokoohi, F. K.; Tarascon, J. M.; Wilkens, B. J. *Applied Physics Letters*, **1991**, *59*, 1260-1262.

[45] Shokoohi, F. K.; Tarascon, J. M.; Wilkens, B. J.; Guyomard, D.; Chang, C. C. *Journal of The Electrochemical Society*, **1992**, *139*, 1845-1849.

[46] Kumagai, N.; Kitamoto, H.; Baba, M.; Durand-Vidal, S.; Devilliers, D.; Groult, H. *Journal of Applied Electrochemistry*, **1997**, *28*, 41-48.

[47] Dahn, J. R.; Sacken, U. v.; Juzkow, M. W.; Al-Janaby, H. *Journal of The Electrochemical Society*, **1991**, *138*, 2207-2211.

[48] Hirano, A.; Kanno, R.; Kawamoto, Y.; Takeda, Y.; Yamaura, K.; Takano, M.; Ohyama, K.; Ohashi, M.; Yamaguchi, Y. *Solid State Ionics*, **1995**, *78*, 123-131.

[49] Delmas, C.; Brethes, S.; Menetrier, M. *Journal of Power Sources*, **1991**, *34*, 113-118.

[50] Bates, J. B.; Dudney, N. J.; Neudecker, B.; Ueda, A.; Evans, C. D. *Solid State Ionics*, **2000**, *135*, 33-45.

[51] Yu, X. H.; Bates, J. B.; Jellison, G. E.; Hart, F. X. *Journal of The Electrochemical Society*, **1997**, *144*, 524-532.

[52] Johnson, B. A.; White, R. E. *Journal of Power Sources*, **1998**, *70*, 48-54.

[53] Prakash, S.; Mustain, W. E.; Park, S.; Kohl, P. A. *Journal of Power Sources*, **2008**, *175*, 91-97.

[54] Tung, S.-P.; Hwang, B.-J. *Journal of Membrane Science*, **2004**, *241*, 315-323.

[55] Digiovanni, D. J.; Morse, T. F. *Journal of American Ceramic Society*, **1988**, *71*, 914-23.

[56] Nogami, M.; Matsushita, H.; Goto, Y.; Kasuga, T. *Advanced Materials (Weinheim, Germany)*, **2000**, *12*, 1370-1372.

[57] Dobkin, D. M. *Journal of electrochemical Society*, **1992**, *139*, 2573-2579.

[58] Hey, H. P. W.; Sluijk, B. G.; Hemmes, D. G. *Solid State Technology*, **1990**, *33*, 139-44.

[59] Hines, A. L.; Maddox, R. N. *Mass Transfer: Fundamentals and Applications* **1985**.

[60] Comyn, J.; Editor. *Polymer Permeability* **1985**.

[61] Crank, J. *The Mathematics of Diffusion. 2d Ed* **1975**.

[62] Molyneux, P. *Journal of Applied Polymer Science*, **2001**, *79*, 981-1024.

[63] Favre, E.; Schaetzel, P.; Nguygen, Q. T.; Clement, R.; Neel, J. *Journal of Membrane Science*, **1994**, *92*, 169-184.

[64] Sohn, W. I.; Ryu, D. H.; Oh, S. J.; Koo, J. K. *Journal of Membrane Science*, **2000**, *175*, 163-170.

[65] Wijmans, J. G.; Baker, R. W. *Journal of Membrane Science*, **1995**, *107*, 1-21.

[66] Morlière, N.; Vallières, C.; Perrin, L.; Roizard, D. *Journal of Membrane Science*, **2006**, *270*, 123-131.

[67] Jia, J.; Baker, G. L. *Journal of Polymer Science, Part B: Polymer Physics*, **1998**, *36*, 959-968.

[68] Barrer, R. M. *Journal of Membrane Science*, **1984**, *18*, 25-35.

[69] Barrer, R. M. *Annales de l'Institut Technique du Batiment et des Travaux Publics*, **1974**, 113-124.

[70] Prabhakar, R. S.; Merkel, T. C.; Freeman, B. D.; Imizu, T.; Higuchi, A. *Macromolecules*, **2005**, *38*, 1899-1910.

[71] Merkel, T. C.; Gupta, R. P.; Turk, B. S.; Freeman, B. D. *Journal of Membrane Science*, **2001**, *191*, 85-94.

[72] Xia, J. Z.; Jodecke, M.; Kamps, A. P. S.; Maurer, G. *Journal of Chemical and Engineering Data*, **2004**, *49*, 1756-1759.

[73] Blyr, A.; Sigala, C.; Amatucci, G.; Guyomard, D.; Chabre, Y.; Tarascon, J. M. *Journal of The Electrochemical Society*, **1998**, *145*, 194-209.

[74] Amatucci, G. G.; Blyr, A.; Sigala, C.; Alfonse, P.; Tarascon, J. M. *Solid State Ionics*, **1997**, *104*, 13-25.

[75] Dudney, N. J. *Journal of Power Sources*, **2000**, *89*, 176-179.

[76] Lee, J.; Lee, J. M.; Yoon, S.; Kim, S. O.; Sohn, J. S.; Rhee, K. I.; Sohn, H. J. *Journal of Power Sources*, **2008**, *183*, 325-329.

[77] West, K.; Zachauchristiansen, B.; Jacobsen, T.; Skaarup, S. *Journal of Power Sources*, **1993**, *43*, 127-134.

[78] Jeon, E. J.; Shin, Y. W.; Nam, S. C.; Cho, W. I.; Yoon, Y. S. *Journal of The Electrochemical Society*, **2001**, *148*, A318-A322.

[79] Tarascon, J. M.; Schmutz, C. N.; Gozdz, A. S.; Warren, P. C.; Shokoohi, F. K. In *MRS Symposium Proceeding*, **1994**; Vol. *369*, pp. 595.

[80] Tarascon, J. M.; Gozdz, A. S.; Schmutz, C.; Shokoohi, F.; Warren, P. C. *Solid State Ionics*, **1996**, *86-88*, 49-54.

[81] Gozdz, A. S.; Schmutz, C. N.; Tarascon, J. M.; Bell Communications Research, Inc: USA, **1994**; Vol. *US Patent 5296318*.